

**Physics-Based Machine Learning Approach for Modeling
the Temperature-Dependent Yield Strength of Superalloys**

B. Steingrímsson ^{*1,2}, X. Fan³, B. Adam⁴, and P. K. Liaw ⁵

1. Imagars LLC, 2062 Thorncroft Drive Suite 1214, Hillsboro, OR 97124, USA. Email: baldur@imagars.com
2. Department of Materials Science and Engineering, The University of Tennessee, Knoxville, TN, 37996, USA. Email: bsteingr@vols.utk.edu
3. Department of Materials Science and Engineering, The University of Tennessee, Knoxville, TN, 37996, USA.
4. School of Mechanical, Industrial and Manufacturing Engineering, Oregon State University, Corvallis, OR 97331, USA.
5. Department of Materials Science and Engineering, The University of Tennessee, Knoxville, TN, 37996, USA.

* Corresponding authors: baldur@imagars.com, bsteingr@vols.utk.edu.

Abstract

In the pursuit of developing high-temperature alloys with improved properties for meeting the performance requirements of next-generation energy and aerospace demands, integrated computational materials engineering (ICME) has played a crucial role. In this paper a machine learning (ML) approach is presented, capable of predicting the temperature-dependent yield strengths of superalloys, utilizing a bilinear log model. Importantly, the model introduces the parameter break temperature, T_{break} , which serves as an upper boundary for operating conditions, ensuring acceptable mechanical performance. In contrast to conventional black-box approaches, our model is based on the underlying fundamental physics, directly built into the model. We present a technique of global optimization, one allowing the concurrent optimization of model parameters over the low-temperature and high-temperature regimes. The results presented extend previous work on high-entropy alloys (HEAs) and offer further support for the bilinear log model and its applicability for modeling the temperature-dependent strength behavior of superalloys as well as HEAs.

Introduction

The conventional approach to alloy design assumes selecting a main component, based on the primary property needed in the alloy, with one or more additions to provide secondary properties. For over six decades, superalloys have provided reliable and cost-effective means for achieving high operating temperatures and stress conditions, first in aircraft and later in industrial gas turbines [1]. The zenith of superalloy development was in the 1960s, as columnar grain alloys and single crystals were then made feasible, and many polycrystalline alloys matured to commercial reality [1]. Since then, advances in the powder metallurgy (P/M) processing and oxide dispersion strengthening have ensued, along with advances in additive manufacturing (AM) and integrated computational materials engineering (ICME).

In the case of Nickel-based superalloys, Nickel is selected for the main component, because of its high melting point. Nevertheless, chromium is added to prevent corrosion, and titanium and aluminum are included to increase strength. The Ni-based superalloys can accommodate γ , γ' , γ'' , η , carbide, or topologically-closed-packaged (TCP) phases, as explained in the Supplementary Manuscript. Co-based superalloys can similarly contain γ , γ' , carbide, or TCP phases. The Co-based superalloys are usually strengthened by a combination of carbides and solid-solution hardeners [1]. The use of steels for applications necessitating superalloys may also be of interest, as further explained in the Supplementary Manuscript, because certain steels have exhibited creep and oxidation resistance analogous to that of the Ni-based superalloys, while being much less expensive to manufacture. Similar to the Ni- and Co-based superalloys, the Fe-based superalloys can accommodate a γ matrix phase along with a γ' phase. The γ' phase is introduced in the form of precipitates to strengthen the Fe-based superalloys.

Machine learning (ML) and data analytics, coupled with physics-based modeling, can assist with the effective search of the compositional space of superalloys and with the optimization of thermomechanical post-processes. Figure 1 outlines the multiple sources that affect the mechanical properties of superalloys. As opposed to specifically applying ML, narrowly-defined in terms of multi-variate regression, single-layer or multi-layer neural networks, Bayesian graphical models, support vector machines, or decision trees, to the identification of superalloy compositions of interest, we reformulate the task in the broader context of engineering optimization [2], [3], [4]. We recommend selecting an optimization technique suitable for the application at hand and the data available, but we certainly include ML in the consideration. Our rationale is based in part on observations from Agrawal et al. [5]. According to Table 2 and Figure 5 of [5], there is at most a difference of a few percentages between the techniques applied to model the fatigue strengths of stainless steels. For further background information on the application of ML to modeling of mechanical properties of alloys, and the motivation for coupling with physics-based modeling approaches, refer to [2], [3], [4].

This paper introduces a bilinear log model for predicting the yield strength of superalloys across temperatures. It consists of separate exponentials, for a low-temperature and a high-temperature regime, with a break temperature, T_{break} , in between. The underlying physics are accounted for, e.g., through diffusion processes required to initiate phase transformations in the high-temperature regime [6]. Moreover, we show in [3] how piecewise linear regression can be employed to extend the model beyond two exponentials and yield accurate fit, in case of a non-convex objective function caused by hump(s) in the data. Previous models for the temperature dependence of yield strengths (YS) only accounted for a single exponential [7], [8]. There was, therefore, no break temperature, T_{break} . We regard the break temperature very important for the optimization of the

high-temperature properties of alloys. For the reliable operation, the temperature of turbine blades or disks (rotors) made from refractory superalloys may need to stay below T_{break} . Once the temperature increases beyond T_{break} , the superalloys can lose strengths rapidly due to rapid diffusion, leading to the easy dislocation motion and dissolution of strengthening phases [6]. We consider T_{break} a very important parameter for the design of superalloys with attractive high-temperature properties, one warranting the inclusion in the superalloy specifications. Hence, it is of paramount importance to be able to accurately estimate T_{break} , e.g., using the global-optimization approach presented in [3].

In terms of impacts, this paper addresses a physics-based, i.e., not a black box, approach to ML and data analytics. Preference to such approaches, especially for applications involving materials science, may primarily stem from the fact that they involve fewer parameters than the black-box models, and hence require less input data. With experiments often being time consuming and expensive, in the case of such applications, high-quality input data tends to be a scarce resource. Moreover, the physics-based modeling approaches help establish causal links between output observations and the behavior of the underlying material system.

Results

Figure 1 summarizes the multiple sources that impact the mechanical properties of superalloys. It bears noting that improvements in the yield strength may come at the expense of other properties. Hence, we have suggested a framework for *joint optimization* [2], [3], [4]. For instance, there typically is a trade-off between the ductility and the strength of the superalloys. Figure 1 resembles an inverse design process, where components of the design are explicitly calculated from the target performance metrics provided.

For forty superalloy compositions, Table 1 compares the performance of the bilinear log model to

that of a model based on a single exponential. When averaged over these forty compositions, the bilinear log model results in a mean squared error (MSE) of 0.00175 in the logarithmic domain, compared to the MSE of 0.0525 for the model based on a single exponential. This difference is much exacerbated in the linear domain, where the bilinear log model yields the MSE of only 4,151 MPa², compared to the MSE of 25,836 MPa² for the model based on a single exponential. Analogous to Wu et al. [7], we employ a model with a single exponential for the overall YS, $\sigma_y(T)$, of the form

$$\sigma_y(T) = \sigma_a \exp\left(\frac{-T}{C}\right) + \sigma_b, \quad (1)$$

where σ_a , C , and σ_b represent fitting coefficients.

In an effort to identify superalloy compositions exhibiting the ability to retain strengths at high temperatures, we present Figure 2 - Figure 3. The strengths of most metals tend to decrease, as the temperature is increased, since as the temperature is increased, it becomes easier for dislocations to surmount obstacles, through the support from thermal activation [9]. In the case of high-temperature applications, one may look to derive a model of the form

$$\text{YS} = h(\text{composition}, T) \quad (2)$$

for the prediction of the YS of the superalloys across temperature.

Looking at Figure 2 - Figure 4, one first observes that the strength vs. temperature data definitely does not look linear. Therefore, a multi-variate linear regression may not constitute a preferred approach. Second, the dependence of the strength on temperature does come across as approximately exponential, but not exactly. Figure 2 -Figure 4 seem to feature a high-temperature and a low-temperature regime. Third, one may refrain from employing an automated ML suite, such as the Tree-Based Pipeline Optimization Tool (T-POT) [10], because of the limited ability of such black-box models to provide much needed insights into the underlying physics. Instead, one

is motivated to make the most of the limited data available, by incorporating important a priori information about the underlying physics into the model structure, for the purpose of deriving such insights. For specifics on the algorithmic aspects of the incorporation of a priori information into the bilinear log model, refer to the Method section. The results in Figure 2 - Figure 4 were derived, using the global-optimization approach, applied separately to individual alloys, for the purpose of obtaining a tighter fit and more accurate estimation of T_{break} , than for separate optimization over the low and high temperature regimes.

In regards to the underlying physics, Ni-based superalloys containing γ' phases, tend to be particularly resistant to temperature with reference to their in-service mechanical properties [9]. Strengthening generally occurs through both alloying elements acting as solutes in the face-centered-cubic (FCC) austenitic matrix phase, and through the solute precipitation strengthening, such as the γ' phase. This phase is responsible for the yield strength of many nickel-based superalloys being relatively insensitive to temperature. The effect arises from dislocation locking on secondary $\{100\}$ slip planes caused by cross-slipping of primary dislocations on $\{111\}$ slip planes in the γ' phases during plastic deformation. Ordinary dislocation slip occurs on the $\{111\}\langle 110\rangle$ plane, both for the γ and the γ' phases. There is, however, a tendency for dislocations in the γ' phase to cross-slip on to secondary $\{100\}$ planes, where they can have a lower anti-phase domain boundary energy (APB). The activation of these secondary slip planes is thermally activated as is the APB, crucial for maximizing the γ' strength, where both decrease with an increase in temperature. This trend explains then the signature peak in the flow stress, seen for γ' -strengthened superalloys [11], [12].

When great strength is required at lower temperatures, e.g., for turbine discs, precipitation strengthening in Ni-based superalloys can be still be utilized, either by employing other phases,

such as the γ'' -phase in Nb-bearing alloys or multimodal size distribution of the γ' -phase. The γ'' phase occurs in Ni-based superalloys, such as Inconel 718, which have significant addition of Niobium or Vanadium. The composition of the γ'' phase is Ni_3Nb or Ni_3V . The γ'' phase consists of a body-centered-tetragonal lattice with an ordered arrangement of Nickel and Niobium atoms. Strengthening occurs primarily through coherency-hardening and order-hardening mechanisms [9]. Further, in regards to dislocation dynamics and diffusion mechanisms, ordinary slips occur on the $\{111\}\langle 110\rangle$ plane, both for the γ and the γ' phases. There is, however, a tendency for dislocations in the γ' phase to cross-slip on to $\{100\}$ planes, where they can have a lower anti-phase domain boundary energy. Situations can arise where an extended dislocation is partly on a close-packed plane and partly on a cube plane. Such a dislocation can become locked and result in an increase in strength (can help retain strength in the low-temperature regime). In the elevated-temperature regime, thermal activations tend to be sufficiently violent to allow dislocations to overcome obstacles [9].

Figure 5 offers a comparison of temperature-dependent yield strengths across superalloy compositions. Similar to [1], we consider the three primary categories of superalloys: (1) Fe-Ni-, (2) Ni-, and (3) Co-based superalloys. Fe-Ni-based superalloys, such as the popular Inconel 718, came into existence as an extension of the stainless-steel technology and are generally heat treated (wrought). Co- and Ni-based superalloys may be heat treated or not (wrought or cast), depending on the application and composition involved. Figure 5 illustrates the following:

1. The precipitation-strengthened superalloys seem to result in higher YS than the solid-solution-strengthened ones, in case of both the Ni-based and the Fe-Ni-based superalloys.
2. The Ni-based superalloys tend to produce higher YS than the Fe-Ni-based superalloys, in case of both precipitation and solid-solution strengthening.

As far as the superior YS of the precipitation-strengthened superalloys is concerned, Figure 5 exhibits resemblance and consistency with Figure 1.1 of [1]. Superalloys can be strengthened through solid-solution strengthening (and its chemistry), but also through the presence of strengthening phases (usually precipitates) [1]. Co-based superalloys can exhibit a tendency towards the transformation of the FCC matrix phase to stable lower-temperature phases. In the case of Ni-based and Fe-Ni-based superalloys, the FCC matrices can exhibit favorable characteristics for precipitation of uniquely effective strengthening phases [1].

Discussion and Conclusions

When looking at the superalloy compositions from the Supplementary Manuscript, the following observations stand out:

1. Many of the superalloy specimens, such as Astroloy, Hastelloy S, Hastelloy X, Waspaloy, Nimonic PE16, Rene 41, Nimonic 80a, Nimonic 90, Rene 95, Nickel 200, Nimonic 263, Udimet 520, Udimet 500, Haynes 556, Inconel 600, Inconel 601, Incoloy 825 and Inconel 807, present fairly straight forward cases, where the bilinear log model offers much better performance than the model based on a single exponent.
2. For some of the superalloy specimen, such as Nimonic PE 13, Nickel 201, Udimet 720, Inconel 801, Inconel X750, and Hastelloy C22, accurate modeling seems to be precluded by a lack of data points in the high-temperature regime.
3. Some of the superalloy specimen, such as Udimet D979, Inconel 802, Inconel 800, Inconel 625, Inconel 617 (sheet), Haynes 188 and Nimonic 75, seem to exhibit behavior featuring a flat intermediate regime.
4. At least one of the superalloy specimens (Inconel 718) may exhibit a trilinear log behavior.

5. Both configurations of the Haynes 230 superalloys, as well as the L 605 superalloy, seem to exhibit an anomalous yield-strength phenomenon (a hump between the low-temperature and high-temperature regimes) [3].

The good match of the bilinear log model with the temperature-dependent strength data for Astroloy, Hastelloy S, Hastelloy X, Waspaloy, Nimonic PE16, Rene 41, Nimonic 80a, Nimonic 90, Rene 95, Nickel 200, Nimonic 263, Udimet 520, Udimet 500, Haynes 556, Inconel 600, Inconel 601, Incoloy 825, and Inconel 807 is consistent with the observations from Figure 2 - Figure 3,

from [3] and from [13]. The models utilized here are presented in the Method section.

The experimental data for the superalloy specimens of Nimonic PE 13, Nickel 201, Udimet 720, Inconel 801, Inconel X750, and Hastelloy C22 did not allow for the estimation of an exponent for the high-temperature regime. In order to estimate the high-temperature exponent, one needs at least two data points above T_{break} .

A flat intermediate regime, such as observed for Udimet D979, Inconel 802, Inconel 800, Inconel 625, Inconel 617 (sheet), Haynes 188, and Nimonic 75, has also been reported for medium- and high-entropy alloys (MEAs and HEAs) [13]. These cases may necessitate the application of the tri-linear log model from Eqs. (13) – (16). Reference [14] offers an explanation for a tri-linear behavior for intrinsic temperature-dependent yield strengths in BCC metals and substitutional solid solutions:

1. Plastic deformation of the BCC metals and alloys is believed to be mediated by the thermally-activated formation and movement of kink pairs, at low temperatures [14].
2. Above a certain “critical temperature,” a flat strength plateau is achieved, where the strength becomes virtually temperature or strain-rate independent [14].

3. When the test temperature exceeds approx. 40% of the melting temperature, diffusional processes can lead to a rapid decrease of yield stress, and the YS becomes strain-rate dependent again [14].

We are looking at two break temperatures, T_{break1} and T_{break2} , in the case of the tri-linear log model [3]. But Ref. [14] only references one such temperature, and refers to it as the “critical temperature” or “knee temperature”, which apparently corresponds to T_{break1} in our model.

The flat intermediate plateau seems less prevalent in alloys with FCC crystal structures. The FCC-crystal structure possesses 12 slip planes with 4 closest packed planes of $\{111\}$ and 3 closest packed directions per plane of $\langle 110 \rangle$. The HCP crystal structure, on the other hand, only has 3 slip systems. The BCC crystal structure does not have truly closest packed planes, so the slips must be thermally activated in the BCC metals. For the further analysis of slip systems, Peierls barriers, dislocation mechanisms, flow stress, and temperature-dependent stress behavior, in BCC vs. FCC metals, refer to the work of Seeger [15], [16]. In the specific case of Inconel 718, the need for a tri-linear log model may be hard to ascertain, due to the possible uncertainty in the experimentally measured data points.

The hump between the low-temperature and the high-temperature regimes (the anomalous yield-strength phenomenon) is characteristic for the γ' - or γ'' -strengthened superalloys [3], [12]. The phenomenon manifests itself as a positive temperature dependence of the total yield strength, and is found in superalloys strengthened by $L1_2$ ordered intermetallics [17]. The increased strength of the γ' phase with temperature is explained by a thermally-activated cross slip of dislocations from $\{111\}$ planes to $\{100\}$ planes, where the partial dislocation locking occurs [18], [19]. The influence of the γ' strengthening increases with increasing the γ' volume fraction and increasing temperature below the peak yield strength, as seen in Figure S5 [11], [20]. Additional factors involve the γ' size, γ' solute content, γ - γ' mismatch, and both the stacking fault energy (SF) as well as the

anti-phase boundary (APB) energy. The latter two factors are the major contributions to hardening for both the matrix phase as well as the precipitate phase, and are both strongly affected by alloying additions [21].

Supplementary datasets for the above-mentioned factors were collected for all alloys, seen in Table S1, where possible, for the solution-annealed and peak-aged condition, maximizing the precipitation-strengthening effect. In reviewing the data on (if present) the strengthening-precipitate type, volume fraction, and average size as well as the lattice misfit for all alloys, the significant scatter becomes apparent, resulting from the lack of data, lack in consistency in the methodology and processing. While this feature provides challenges to data extraction and comparability, it also shows the complex precipitation and growth as function of prior processing and heat treatment, as well as the need for incorporating physics-based prediction models that can account for multimodal-precipitate distributions [22], [23].

For example, this trend is illustrated by the alloy CMSX-4, a γ' -strengthened, single-crystal, Nickel-based superalloy, where three exponentials are needed for accurate modeling in case of Heat Treatment A, but four exponentials in case of Heat Treatment B, according to the Supplementary Figure 4 [3], [17].

In conclusion, we proposed a bilinear log model for predicting the YS of superalloys across temperatures and studied its effectiveness for 38 distinct compositions (40 configurations). We considered the break temperature, T_{break} , an important parameter for the design of superalloys materials with favorable elevated-temperature properties, one warranting the inclusion in the superalloy alloy specifications. For reliable operations, and not accounting for coatings, the operating temperatures for the corresponding superalloys may need to stay below T_{break} . Earlier models for the temperature dependence of the yield strength only accounted for a single

exponential, and thus did not feature a break temperature. Across these 40 configurations, we demonstrated much superior performance of the bilinear log model, compared to the one comprising a single exponential. In the logarithmic domain, the bilinear log model resulted in MSE of 0.00175, compared to the MSE of 0.0525 for the single-exponent model. But in the linear domain, the bilinear log model produced MSE of 4,151 MPa², averaged across these 40 configurations, compared to the MSE of 25,836 MPa² for the single-exponent model. Our observations regarding the superior YS behavior of precipitation-strengthened superalloys, compared to solid-solution strengthened superalloys, for both the Ni-based and Fe-Ni-based superalloys, were consistent with those of Donachie et al. [1]. Similarly, our observations concerning superior YS properties of Ni-based superalloys, compared to Fe-Ni-based superalloys, in the case of both precipitation and solid-solution hardening, were also consistent with those of Donachie et al. [1].

Methods

Although the primary emphasis here is on the yield strength, the optimization of the mechanical properties is assumed to take place within a framework for joint optimization [3], [13].

Methodology for Maximization of the YS

Our approach accurately captures the input sources that contribute to variations in the YS observed, relative to variations in the output. The input parameters for the model used in the present work are [3]:

$$\text{Input} = (\text{composition}, T, \text{process}, \text{defects}, \text{grain size}, \text{microstructure}). \quad (3)$$

In this context, “defects” are defined broadly, such as to include inhomogeneities, impurities, dislocations, or further undesirable features, while “ T ” represents temperature. Analogously, the term “microstructure” broadly represents microstructures here, at the nano or micro scale, and

phase properties, and the term “process” broadly refers to manufacturing processes and post-processing. Similarly, the term “grain size” generally refers to the distribution of grain sizes. Section 4.4 of [4] accounts for the dependence between input sources, and Section 4.5 of [4] addresses the expected dependence of the US on the individual input sources listed. The prediction model can be summarized as [3], [13]

$$US = h[\text{composition}, T, \text{process}, \text{defects}(\text{process}, T), \text{grains}(\text{process}, T), \text{microstructure}(\text{process}, T)]. \quad (4)$$

If the YS corresponding to a certain input combination is known, one can simply look up the known value. However, if the YS corresponding to a given input combination is not known, then a prediction step can be applied (e.g., interpolation or extrapolation) [13].

Methodology for Modeling YS at Elevated Temperature

Motivated by Figures 3(c) and (d) of [3], along with physics-based insights from [6], we model the temperature dependence of the $YS(T)$, in terms of a bilinear log model, parametrized by the melting temperature, T_m , as follows [13]:

$$YS(T) = \min(\log(YS_1(T)), \log(YS_2(T))), \quad (5)$$

$$YS_1(T) = \exp(- C_1 * T / T_m + C_2), \quad 0 < T < T_{\text{break}}, \quad (6)$$

$$YS_2(T) = \exp(- C_3 * T / T_m + C_4), \quad T_{\text{break}} < T < T_m. \quad (7)$$

T_{break} is subjected to a separate physics (diffusion)-induced constraint [6]:

$$0.35 \lesssim T_{\text{break}} / T_m \lesssim 0.55, \quad (8)$$

as well as a continuity constraint between the low-temperature and high-temperature regimes:

$$YS_1(T_{\text{break}}) = YS_2(T_{\text{break}}); \quad (9)$$

$$T_{\text{break}} = \frac{(C_4 - C_2)}{(C_3 - C_1)} T_m. \quad (10)$$

As elucidated in [3], [13], a conceptually simple approach for fitting the model in Eqs. (5) – (10) to the YS data available consists of first deriving the constant coefficients, C_1 and C_2 , by applying

linear regression to the data points available to the lowest temperature region ($0 < T < 0.35 T_m$) as well as to the intermediate region ($0.35 T_m \leq T \leq 0.55 T_m$). One can then obtain the constants, C_3 and C_4 , by applying linear regression to the data points available to the intermediate ($0.35 T_m \leq T \leq 0.55 T_m$) and high-temperature ($T > 0.55 T_m$) regions. Note that T_{break} does not have to be known in advance. As supported by Eq. (10), T_{break} is an inherent property of a given alloy that emerges from the model as the break point between the two linear regions. The model in Eqs. (5) – (7) comprises of only four (4) independent parameters, C_1 , C_2 , C_3 , and C_4 , which simply can be estimated by applying linear regression separately to low-temperature and high-temperature regimes, even to a fairly small data set. Note, furthermore, that for a new alloy system, T_m , does not have to be known experimentally in advance either; a rough estimate for T_m may be obtained, by using “the rule of mixing” and a more refined estimate obtained, by employing the Calculation of Phase Diagram (CALPHAD) simulations [4].

A superior method for deriving the coefficients, C_1 , C_2 , C_3 , and C_4 , entails the concurrent optimization over the low-temperature and high-temperature regimes, using the global optimization. Here, one looks to minimize [13]

$$\min_{C_1, C_2, C_3, C_4} \text{norm}_2 \left((YS(T_i) - y_i)^2 \right), \quad (11)$$

where y_i represents the YS values measured,

$$YS(T_i) = \min(\log(YS_1(T_i)), \log(YS_2(T_i))), \quad (12)$$

and $YS_1(T_i)$ and $YS_2(T_i)$ are modeled, employing Eqs. (6) and (7), respectively. Matlab provides a function, `fminunc()`, for solving this sort of unconstrained minimization over a generic function.

Depending on the grain sizes and the compositions comprising the alloys, a tri-linear log model may offer a better fit for specific alloys [3], [13], [24]:

$$YS(T) = \min(YS_1(T), YS_2(T), YS_3(T)), \quad (13)$$

$$YS_1(T) = \exp(-C_1 * T / T_m + C_2), \quad 0 < T < T_{\text{break1}}, \quad (14)$$

$$YS_2(T) = \exp(-C_3 * T / T_m + C_4), \quad T_{\text{break1}} < T < T_{\text{break2}}, \quad (15)$$

$$YS_3(T) = \exp(-C_5 * T / T_m + C_6), \quad T_{\text{break2}} < T < T_m. \quad (16)$$

Data Availability

The data in this paper, including those in the Supplementary Figures, can be requested by contacting the corresponding author (baldur@imagars.com, bsteingr@vols.utk.edu).

Code Availability

Matlab comprises the software package primarily used for this study. The Supplementary Figures 7 and 8 of [3] contain an Matlab source code for the objective functions optimized in case of the bilinear or trilinear log model, respectively.

Acknowledgements

XF and PKL very much appreciate the support of the U.S. Army Research Office Project (W911NF-13-1-0438 and W911NF-19-2-0049) with the program managers, Drs. M. P. Bakas, S. N. Mathaudhu, and D. M. Stepp. PKL thanks the support from the National Science Foundation (DMR-1611180, 1809640, and 2226508) with the program directors, Drs. J. Madison, J. Yang, G. Shiflet, and D. Farkas. XF and PKL also appreciate the support from the Bunch Fellowship. XF and PKL would like to acknowledge funding from the State of Tennessee and Tennessee Higher Education Commission (THEC) through their support of the Center for Materials Processing (CMP). BS very much appreciates the support from the National Science Foundation (IIP-1447395 and IIP-1632408), with the program directors, Drs. G. Larsen and R. Mehta, from the U.S. Air Force (FA864921P0754), with J. Evans as the program manager, and from the U.S. Navy (N6833521C0420), with Drs. D. Shifler and J. Wolk as the program managers.

The authors also want to thank Dr. Graham Tewksbury for offering insightful comments on strengthening mechanisms in superalloys during an October 21, 2021, material science graduate seminar presentation, conducted by BS at Oregon State University. The authors similarly want to thank Dr. Chanhoo Lee for bringing precursors to Supplementary Figures S1 – S3 to their attention.

Author Contributions

B.S. and P.K.L conceived the project. B.S. performed the modeling of the temperature-dependent yield strength and put together the Supplementary Manuscript. X.F. helped prepare the database. R.F. contributed towards analytical modeling. All authors edited and proofread the final manuscript and participated in discussions.

Competing Interests

The authors declare no competing interests (financial or non-financial).

References

1. M.J. Donachie and S.J. Donachie, *Superalloys, a Technical Guide*. 2002, Second Edition: ASM International.
2. B. Steingrímsson, X. Fan, A. Kulkarni, D. Kim and P.K. Liaw, *Machine Learning to Accelerate Alloy Design*. US Patent Application 16/782,829, filed on February 5, 2020.
3. B. Steingrímsson, X. Fan, X. Yang, M.C. Gao, Y. Zhang and P.K. Liaw, *Predicting Temperature-Dependent Ultimate Strengths of Body-Centered Cubic (BCC) High-Entropy Alloys*. NPJ Computational Materials, September 24, 2021. **7**(152).
4. B. Steingrímsson, X. Fan, A. Kulkarni, M.C. Gao, and P.K. Liaw, *Machine Learning and Data Analytics for Design and Manufacturing of High-Entropy Materials Exhibiting Mechanical or Fatigue Properties of Interest*, in *High-Entropy Materials: Theory, Experiments, and Applications*. 2021, Springer Nature Switzerland AG: Editors: James Brechtel and Peter K. Liaw. pp. 115-238.
5. A. Agrawal, P.D. Deshpande, A. Cecen and G.P. Basavarsu, *Exploration of data science techniques to predict fatigue strength of steel from composition and processing parameters*. Integrating Materials and Manufacturing Innovation, 2014. **3**(1): pp. 1–19.
6. O.N. Senkov, S. Gorsse, and D.B. Miracle, *High Temperature Strength of Refractory Complex Concentrated Alloys*. Acta Materialia, 2019. **175**: pp. 394 - 405.
7. Z. Wu, H.B., G.M. Pharr and E.P. George, *Temperature dependence of the mechanical properties of equiatomic solid solution alloys with face-centered cubic crystal structures*. Acta Materialia, 2014. **81**: pp. 428-441.
8. F. Maresca and W.A. Curtin, *Mechanistic origin of high strength in refractory BCC high entropy alloys up to 1900K*. Acta Materialia, 2020. **182**: pp. 235-249.
9. Bhadeshia, H.K.D.H., *Nickel Based Superalloys*. 2019, University of Cambridge.
10. T.T. Le, W. Fu and J.H. Moore, *Scaling tree-based automated machine learning to biomedical big data with a feature set selector*. Bioinformatics, 2020. **36**(1): pp. 250-256.
11. Reed, R.C., *The superalloys: fundamentals and applications*. 2008: Cambridge University Press.
12. C.T. Sims, N.S. Stoloff, and W.C. Hagel, *Superalloys II*. Vol. 8. 1987: Wiley New York.
13. B. Steingrímsson, X. Fan, R. Feng and P.K. Liaw, *Physics-Based Machine-Learning Approach for Modeling the Temperature-Dependent Yield Strengths of Medium- or High-Entropy Alloys*". Applied Materials Today, submitted on Aug. 4, 2022.
14. H. Chen, A. Kauffmann, S. Laube, I.C. Choi, R. Schwaiger, Y. Huang, K. Lichtenberg, F. Muller, B. Gorr, H.J. Christ and M. Heilmaier, *Contribution of Lattice Distortion to Solid Solution Strengthening in a Series of Refractory High Entropy Alloys*. Metallurgical and Materials Transactions A, 2018. **49**: pp. 772-781.
15. Seeger, A., *Why anomalous slip in body-centred cubic metals?* Materials Science and Engineering: A, 2001. **319-321**: pp. 254-260.
16. Seeger, A., *Peierls barriers, kinks, and flow stress: Recent progress*. 2002. **93**(8): p. 760-777.
17. A. Sengupta, S.K. Putatunda, L. Bartosiewicz et al., *Tensile Behavior of a New Single-Crystal Nickel-Based Superalloy (CMSX-4) at Room and Elevated Temperatures*. Journal of Materials Eng. and Performance, 1994. **3**: pp. 73 – 81.
18. Kear, B., *Role of 2-Dislocation Boundaries in Plastic Deformation of FCC Crystals*. Transactions of the Metallurgical Society of AIME, 1962. **224**(4): p. 674.
19. Kear, B., *Clustering of Slip Bands in Cu₃Au Crystals*. Transactions of the Metallurgical Society of AIME, 1962. **224**(4): pp. 669-673.
20. Kruml, T., et al., *From dislocation cores to strength and work-hardening: a study of binary Ni₃Al*. Acta Materialia, 2002. **50**(20): pp. 5091-5101.
21. Chen, Z., et al., *Improving the intermediate- and high-temperature strength of L1₂-Co₃(Al,W) by Ni and Ta additions*. Acta Materialia, 2022. **238**: p. 118224.
22. E.I. Galindo-Nava and C.M.F. Rae, *Microstructure evolution during dynamic recrystallisation in polycrystalline nickel superalloys*. Materials Science and Engineering: A, 2015. **636**: pp. 434-445.

23. E.I. Galindo-Nava, L.D. Connor, and C.M.F. Rae, *On the prediction of the yield stress of unimodal and multimodal γ' Nickel-base superalloys*. Acta Materialia, 2015. **98**: pp. 377-390.
24. F. Otto, A. Diouhý, C. Somsen, H. Bei, G. Eggeler and E.P. George, *The influence of temperature and microstructure on the tensile properties of a CoCrFeNiMn high-entropy alloy*. Acta Mater., 2013. **61**: pp. 5743–5755.

Table 1: Quantification of ability of superalloy compositions to retain yield strengths at high temperatures. T_{break} refers to the breaking point between bilinear log models, defined in Eq. (10).

No.	Alloy	Category	Solvus Temperature [°C]	T_{break} [°C]	MSE: Two exponentials		MSE: Single exponential	
					Log	Linear	Log	Linear
1	Waspaloy	Ni-base (precipit. hard.)	1,330	755.2	6.367e-04	5,118	0.0070	44,260
2	Udimet D979	Fe-Ni-base (precipit. hard.)	1,390	717.7	0.005391	7,678	0.0138	36,204
3	Udimet 720	Ni-base (precipit. hard.)	1,371	Not enough high-temp data pts.		0.00056	243,720	
4	Udimet 520	Ni-base (precipit. hard.)	1,371	728.6	5.663e-05	2,221	0.0162	50,701
5	Udimet 500	Ni-base (precipit. hard.)	1,360	748.9	7.901e-05	1,331	0.0181	48,108
6	Astroloy	Ni-base (precipit. hard.)	1,399	760.6	5.759e-04	6,643	0.0091	80,097
7	Incoloy 825	Fe-Ni-base (solid sol.)	1,370	727.6	3.196e-07	14	0.0367	2,198
8	Inconel 807	Fe-Ni-base (solid sol.)	1,275	774.1	1.069e-04	1,358	0.00136	3,442
9	Inconel 802	Fe-Ni-base (solid sol.)	1,372	760.0	0.00252	1,049	0.00495	2,248
10	Inconel 801	Fe-Ni-base (solid sol.)	1,372	Not enough high-temp data pts.		0.00009	10,504	
11	Inconel 800	Fe-Ni-base (solid sol.)	1,357	675.8	4.131e-04	637	0.00163	2,364
12	Incoloy 800	Fe-Ni-base (solid sol.)	1,350	Not enough high-temp data pts.		0.00623	699.8	
13	Inconel X750	Ni-base (precipit. hard.)	1,393	Not enough high-temp data pts.		0.00000	90,438	
14	Inconel 718	Ni-base (precipit. hard.)	1,260	717.3	0.01707	7,622	0.00819	58,230
15	Inconel 625	Ni-base (solid sol.)	1,290	766.8	2.911e-04	598	0.01615	14,501
16	Inconel 617 (sheet)	Ni-base (solid sol.)	1,332	893.4	0.00201	2,790	0.00235	4,010
17	Inconel 601	Ni-base (solid sol.)	1,360	735.0	7.862e-04	99	0.18572	7,360
18	Inconel 600	Ni-base (solid sol.)	1,354	760.1	1.639e-04	10	0.22850	4,314
19	Ti ₆ Al ₄ V	α and β phases	1,604	501.6	1.793e-04	134	0.01299	12,367
20	Haynes 556	Fe-Ni-base (solid sol.)	1,371	775.6	1.039e-04	1,390	0.00107	3,771
21	Haynes 230 (a)	Ni-base (solid sol.)	1,288	798.4	0.002124	1,591	0.00376	6,176
22	Haynes 230 (b)	Ni-base (solid sol.)	1,288	829.3	0.002035	260	0.12314	7,681
23	Haynes 188	Co-base (solid sol.)	1,315	932.8	0.001307	4,807	0.00138	6,002
24	Hastelloy C22	Ni-base (solid sol.)	1,357	Not enough high-temp data pts.		0.00020	4,647	
25	Hastelloy S	Ni-base (solid sol.)	1,335	765.2	8.509e-05	454	0.00859	6,211
26	Hastelloy X	Ni-base (solid sol.)	1,260	837.6	0.002745	212	0.13881	5,298
27	Hastelloy X (10 μ m)	Ni-base (solid sol.)	1,260	744.4	0.003165	137	0.24225	11,620
28	Rene 95	Ni-base (precipit. hard.)	1,343	627.6	0.000001	80,757	0.00135	217,771
29	Rene 41	Ni-base (precipit. hard.)	1,316	748.1	0.000009	663	0.03624	79,716
30	Pure Nickel	Ni-base	1,455	Not enough high-temp data pts.		0.00892	64	
31	Nickel 201	Ni-base (solid sol.)	1,435	Not enough high-temp data pts.		0.00246	132	
32	Nickel 200	Ni-base (solid sol.)	1,435	349.4	0.001337	22	0.01677	258
33	Nimonic 263	Ni-base (precipit. hard.)	1,300	758.8	0.000262	82	0.08506	15,601
34	Nimonic 90	Ni-base (precipit. hard.)	1,310	724.8	7.875e-05	74	0.08111	29,514
35	Nimonic 80a	Ni-base (precipit. hard.)	1,320	754.3	0.000351	156	0.05091	19,933
36	Nimonic 75	Fe-Ni-base (solid sol.)	1,340	731.2	0.001561	92	0.06840	1,391
37	Nimonic PE16	Fe-Ni-base (precipit. hard.)	1,310	731.6	2.512e-05	7	0.1399	16,557
38	Nimonic PE13	Fe-Ni-base (solid sol.)	1,310	Not enough high-temp data pts.		0.00131	6,424	
39	N155	Fe-Ni-base (solid sol.)	1,288	847.5	0.008876	687	0.0670	2,998
40	L605	Co-base (solid sol.)	1,330	Not enough high-temp data pts.		0.00782	3,666	
Average (No. 1-2, 4-9, 11, 14-23, 25-30, 32-37 and 39):					0.00175	4,151	0.0525	25,836

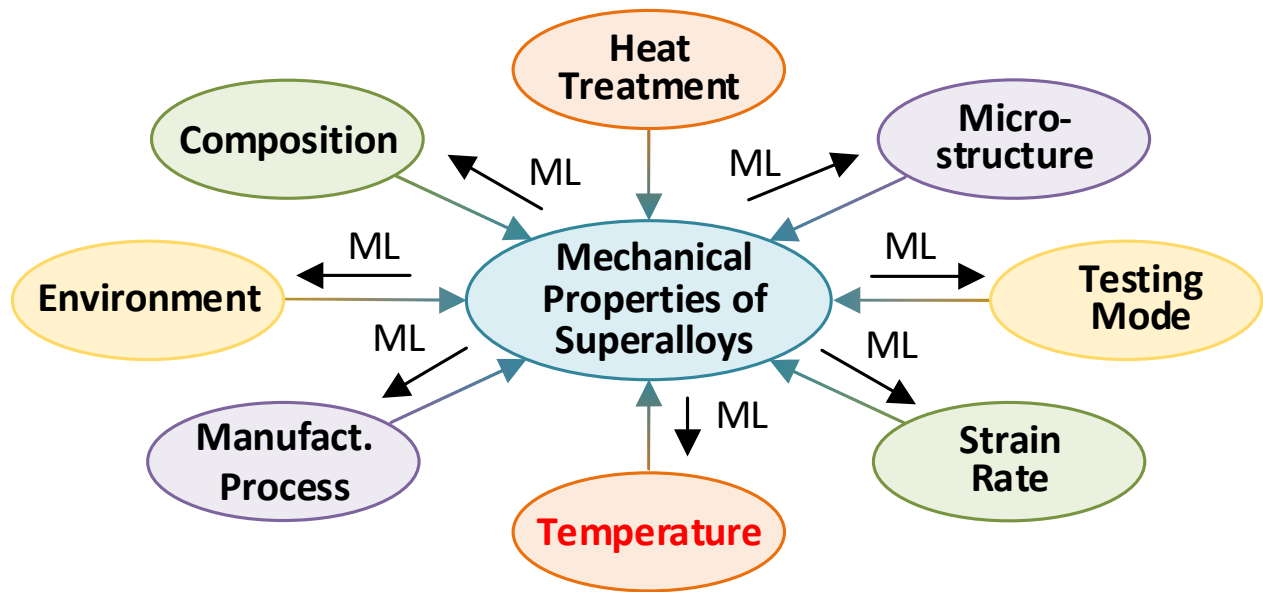
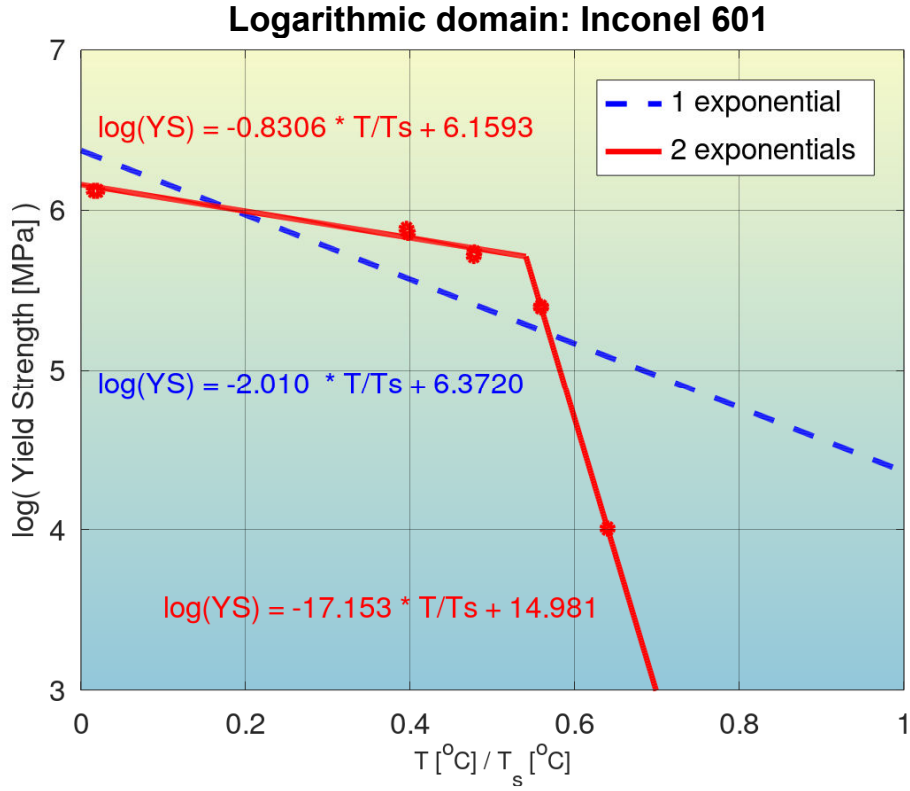


Figure 1: High-level depiction of the role of ML and optimization inferring the features giving rise to the superalloy properties observed, including the yield strength [2], [4].

(a)



(b)

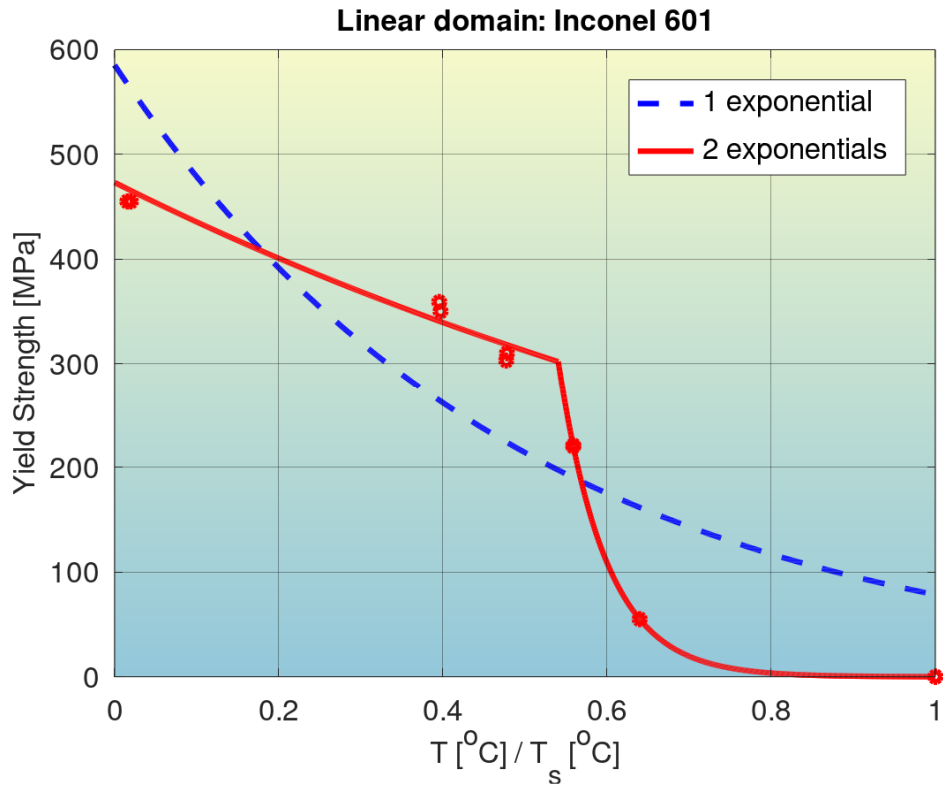
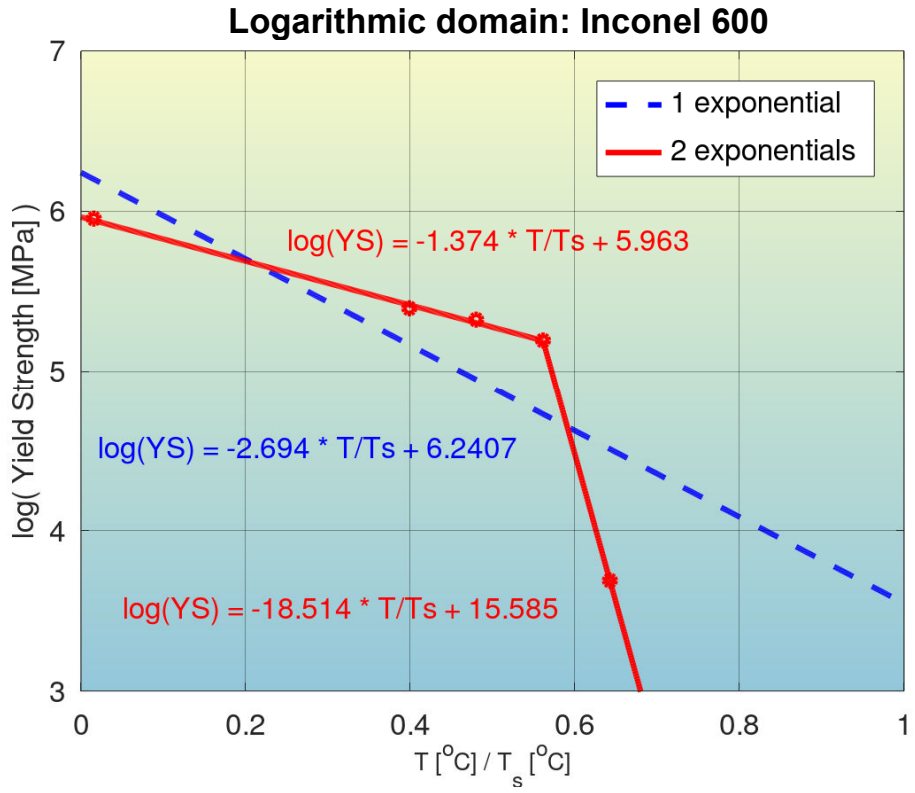


Figure 2: Quantification of modeling accuracy of the bilinear log model, for the composition No. 17 from Table 1 (Inconel 601), and comparison to that of a model with a single exponential. One outlier has been excluded from the modeling.

(a)



(b)

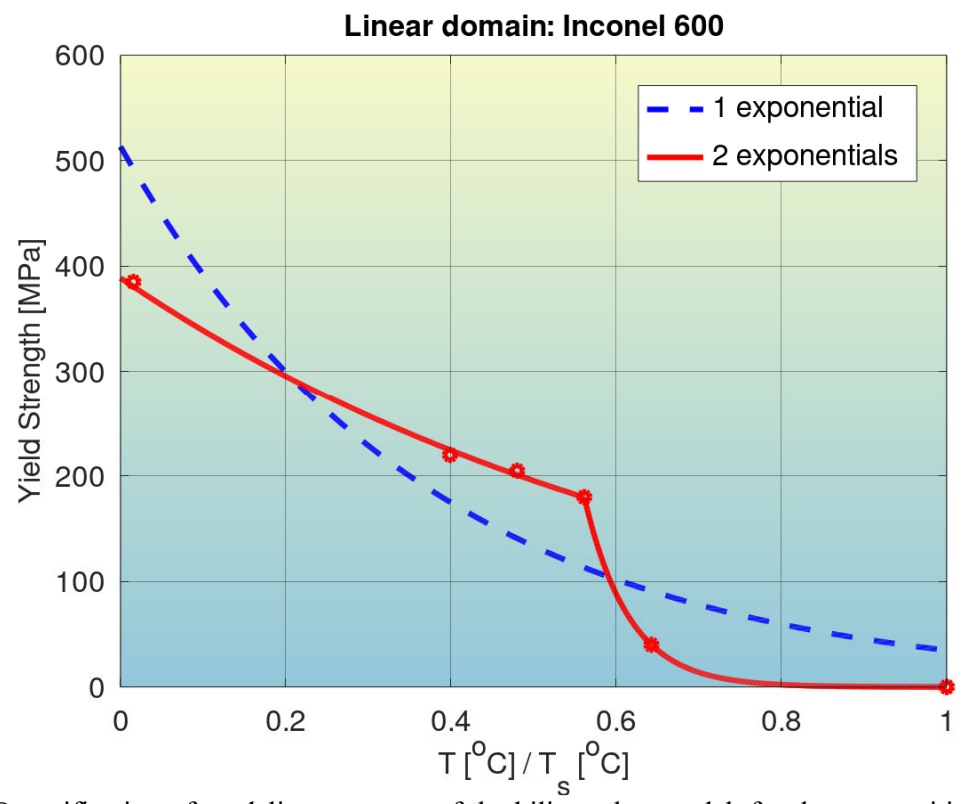
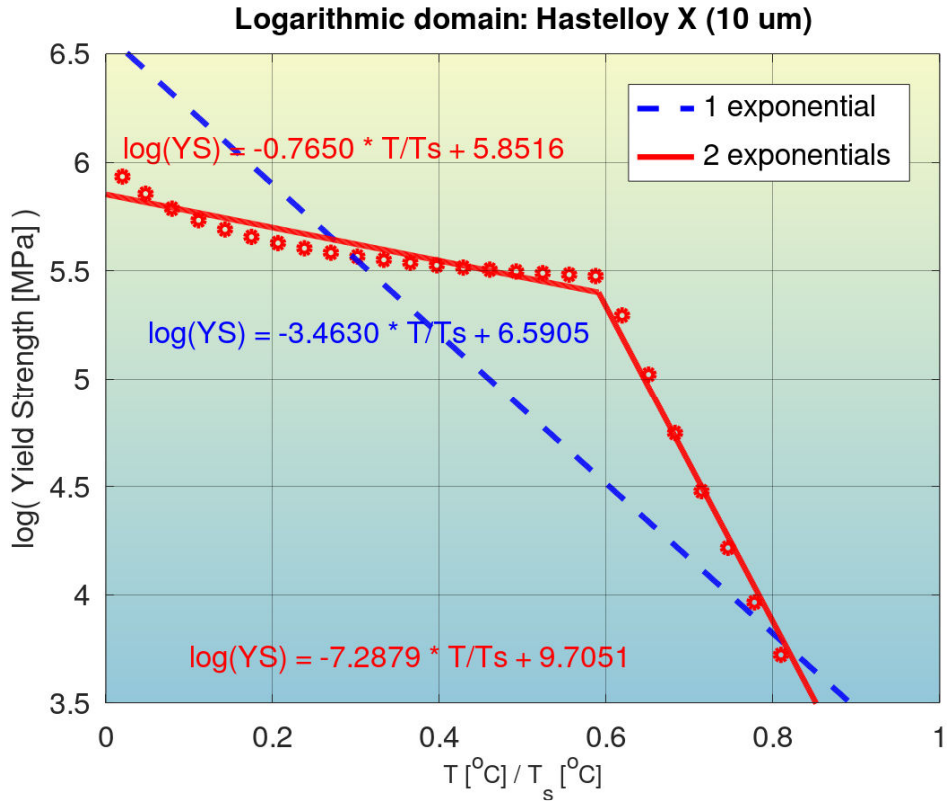


Figure 3: Quantification of modeling accuracy of the bilinear log model, for the composition No. 18 from Table 1 (Inconel 600), and comparison to that of a model with a single exponential. One outlier has been excluded from the modeling.

(a)



(b)

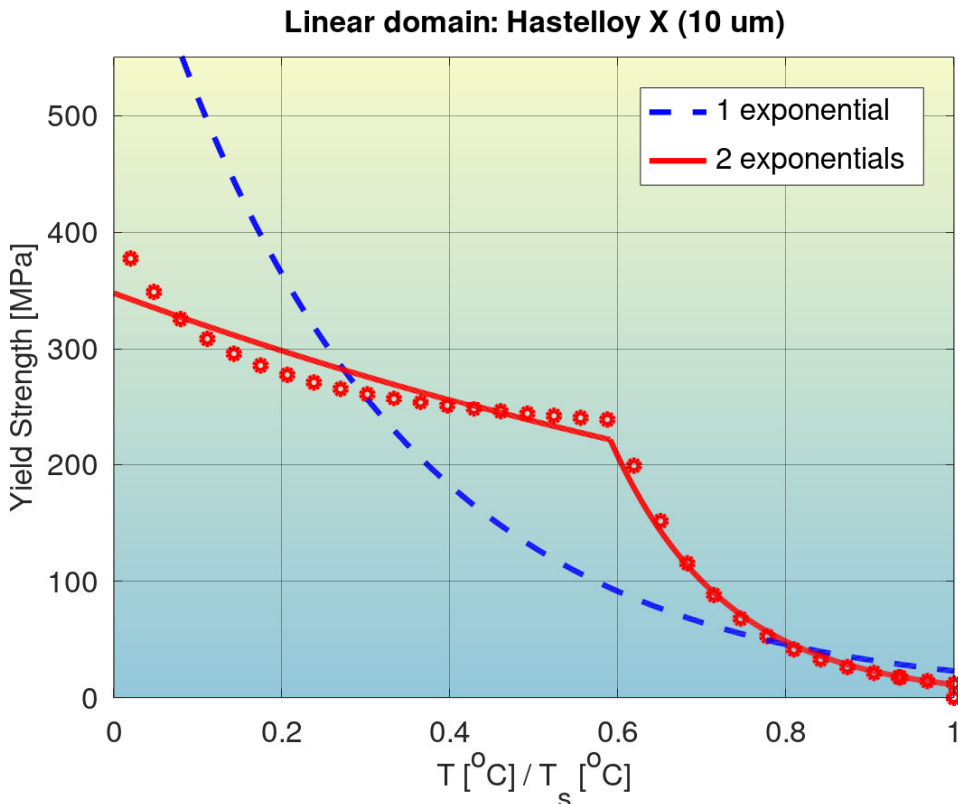
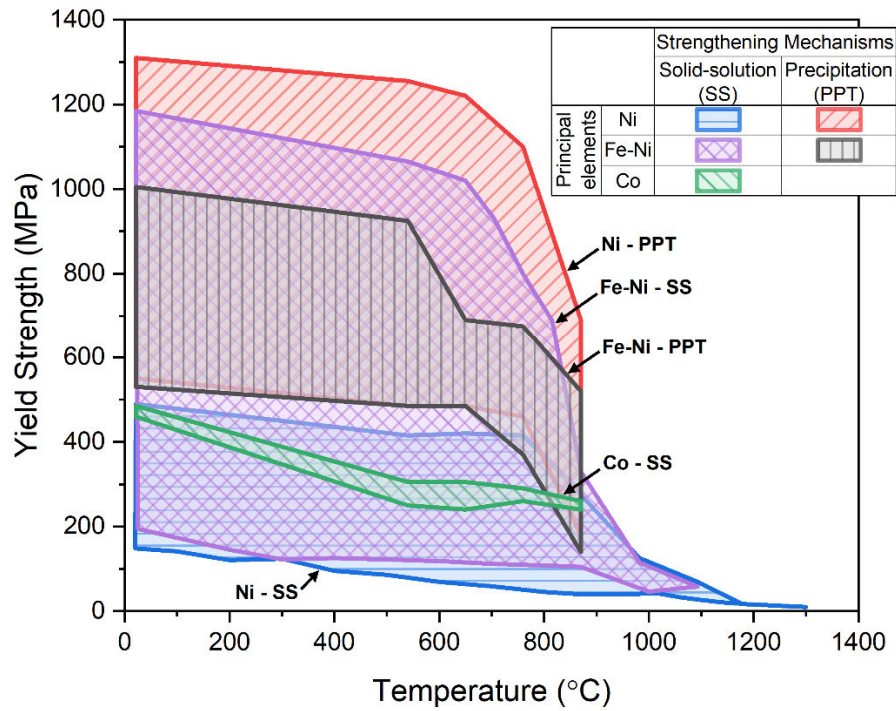


Figure 4: Quantification of modeling accuracy of the bilinear log model, for the composition No. 27 from Table 1 (Hastelloy X 10 μm), and comparison to that of a model with a single exponential. One outlier has been excluded from the modeling.

(a)



(b)

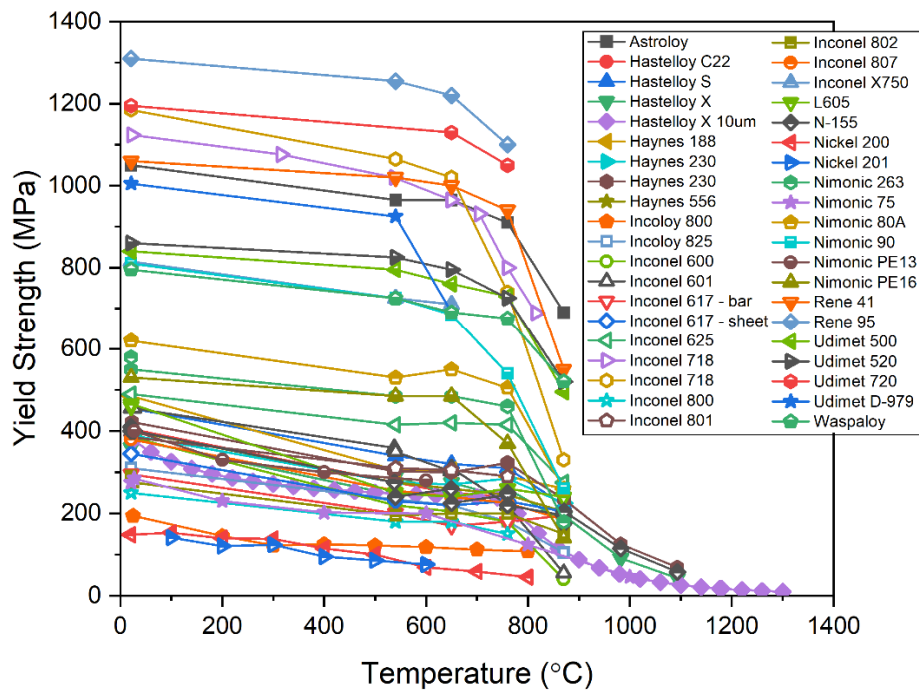


Figure 5: Comparison of temperature-dependent yield-strength properties of Fe-Ni-based, Ni-based, and Co-based superalloys.

Supplementary Manuscript

Table S1: Key properties impacting high-temperature strengths for the superalloys under study. ¹ Unless otherwise noted, all values are for a wrought, standard annealed and aged state, where applicable. ² Equivalent Circle Diameter (ECD). ³ Total volume fraction in case of a multimodal distribution. ⁴ Primary precipitate ⁵ Secondary/aged precipitate form; ⁶ Lattice-mismatch austenite matrix and precipitate phase at a constant temperature.

No.	Alloy	Category	Precipitate / dispersoid ¹					Matrix grain size [μm] ^{1,2}	Ref.
			Type	Volume Fraction ³	Avg. size [μm] ⁴	Avg. size [μm] ⁵	Lattice mismatch [%] ⁶		
1	Waspaloy	Ni-base (precipit. hard.)	γ'	0.2 - 0.5; 0.3-0.4	0.025	-	0.5	25-35	[1], [2]
2	Udimet D979	Fe-Ni-base (precipit. hard.)	γ'	-	0.02-0.04	-	-	20-30	[3], [4]
3	Udimet 720	Ni-base (precipit. hard.)	γ'	0.3 - 0.4	0.05-0.1	1	0.02	325 – 350	[5], [6], [7]
4	Udimet 520	Ni-base (precipit. hard.)	γ'	0.3	0.02-0.05	-	-	60	[8]
5	Udimet 500	Ni-base (precipit. hard.)	γ'	0.25	0.08-0.1	-	0.3	60-90	[2], [9], [10]
6	Astroloy	Ni-base (precipit. hard.)	γ'	-	-	-	-	-	-
7	Incoloy 825	Fe-Ni-base (solid sol.)	MC	0.002	0.04	-	-	122	[11]
8	Inconel 807	Fe-Ni-base (solid sol.)	-	-	-	-	-	-	-
9	Inconel 802	Fe-Ni-base (solid sol.)	-	-	-	-	-	-	-
10	Inconel 801	Fe-Ni-base (solid sol.)	-	-	-	-	-	-	-
11	Inconel 800	Fe-Ni-base (solid sol.)	MC	0.002-0.003	0.1	-	-	120	[12]
12	Incoloy 800			-	-	-	-	-	-
13	Inconel X750	Ni-base (precipit. hard.)	γ'	0.25	0.02-0.03	-	0.8-1.0	170	[13]
14	Inconel 718	Ni-base (precipit. hard.)	γ', γ''	0.15-0.2	0.01-0.03	0.02	-	300	[14], [15]
15	Inconel 625	Ni-base (solid sol.)	M(C,N), M23C6	-	-	-	-	70-90	[16], [17]
16	Inconel 617	Ni-base (solid sol.)	M(C,N), M23C6 M6C	-	-	-	-	45-100	[18], [19]
17	Inconel 601	Ni-base (solid sol.)	M(C,N)	-	-	-	-	70-90	Special Metals Infosheet
18	Inconel 600	Ni-base (solid sol.)	M(C,N)	-	-	-	-	30-40	[20]
19	Ti ₆ Al ₄ V	α and β phases	-	-	-	-	-	-	-

Table S1 (continued): Key properties impacting high-temperature strengths for the superalloys under the study. ¹ Unless otherwise noted, all values are for a wrought, standard annealed and aged state, where applicable. ² Equivalent Circle Diameter (ECD). ³ Total volume fraction in case of multimodal distribution. ⁴ Primary precipitate ⁵ Secondary/aged precipitate form; ⁶ Lattice mismatch of the austenite matrix and precipitate phase at a constant temperature.

No.	Alloy	Category	Precipitate / dispersoid ¹					Matrix grain size [μm] ^{1,2}	Ref.
			Type	Volume Fraction ³	Avg. size [μm] ⁴	Avg. size [μm] ⁵	Lattice mismatch [%] ⁶		
20	Haynes 556	Fe-Ni-base (solid sol.)	-	-	-	-	-	45	[21]
21	Haynes 230 (a)	Ni-base (solid sol.)	-	-	-	-	-	70-90	[18], [22]
22	Haynes 230 (b)		-	-	-	-	-	-	-
23	Haynes 188	Co-base (solid sol.)	-	-	-	-	-	40-50	[23], [24]
24	Hastelloy C22	Ni-base (solid sol.)	Ni2Cr, M6C, M23C6	-	-	-	-	50-100	[25], Haynes Data Sheet
25	Hastelloy S	Ni-base (solid sol.)	-	-	-	-	-	-	-
26	Hastelloy X	Ni-base (solid sol.)	-	-	-	-	-	50	[26]
27	Hastelloy X (10 μm)		-	-	-	-	-	-	-
28	Rene 95	Ni-base (precipit. hard.)	γ', MC	0.4-0.5	0.2	-	-	10-20	[27], [28]
29	Rene 41	Ni-base (precipit. hard.)	γ'	0.3-0.4	0.1	-	-	40-60	[29], [30]
30	Pure Nickel	Ni-base	-	-	-	-	-	-	-
31	Nickel 201	Ni-base (solid sol.)	-	-	-	-	-	-	-
32	Nickel 200	Ni-base (solid sol.)	-	-	-	-	-	-	-
33	Nimonic 263	Ni-base (precipit. hard.)	γ', η	0.1-0.15	0.01-0.03	0.02-0.1	-	100-200	[31], [32], [33]
34	Nimonic 90	Ni-base (precipit. hard.)	γ'	-	-	-	0.34	-	[7], [34], [35]
35	Nimonic 80a	Ni-base (precipit. hard.)	γ'	-	0.02-0.05	-	0.32	90	[7], [34], [35]
36	Nimonic 75	Fe-Ni-base (solid sol.)	M23C6	0.7-1.2	-	-	-	10-20	[34], [35], [36]
37	Nimonic PE16	Fe-Ni-base (precipit. hard.)	γ'	0.08-0.12	0.01-0.05	-	0.03	15-20	[37], Special Metals Datasheet
38	Nimonic PE13	Fe-Ni-base (solid sol.)	-	-	-	-	-	-	-
39	N155	Fe-Ni-base (solid sol.)	-	-	-	-	-	20-30	[38]
40	L605	Co-base (solid sol.)	-	-	-	-	-	60-90	[39]

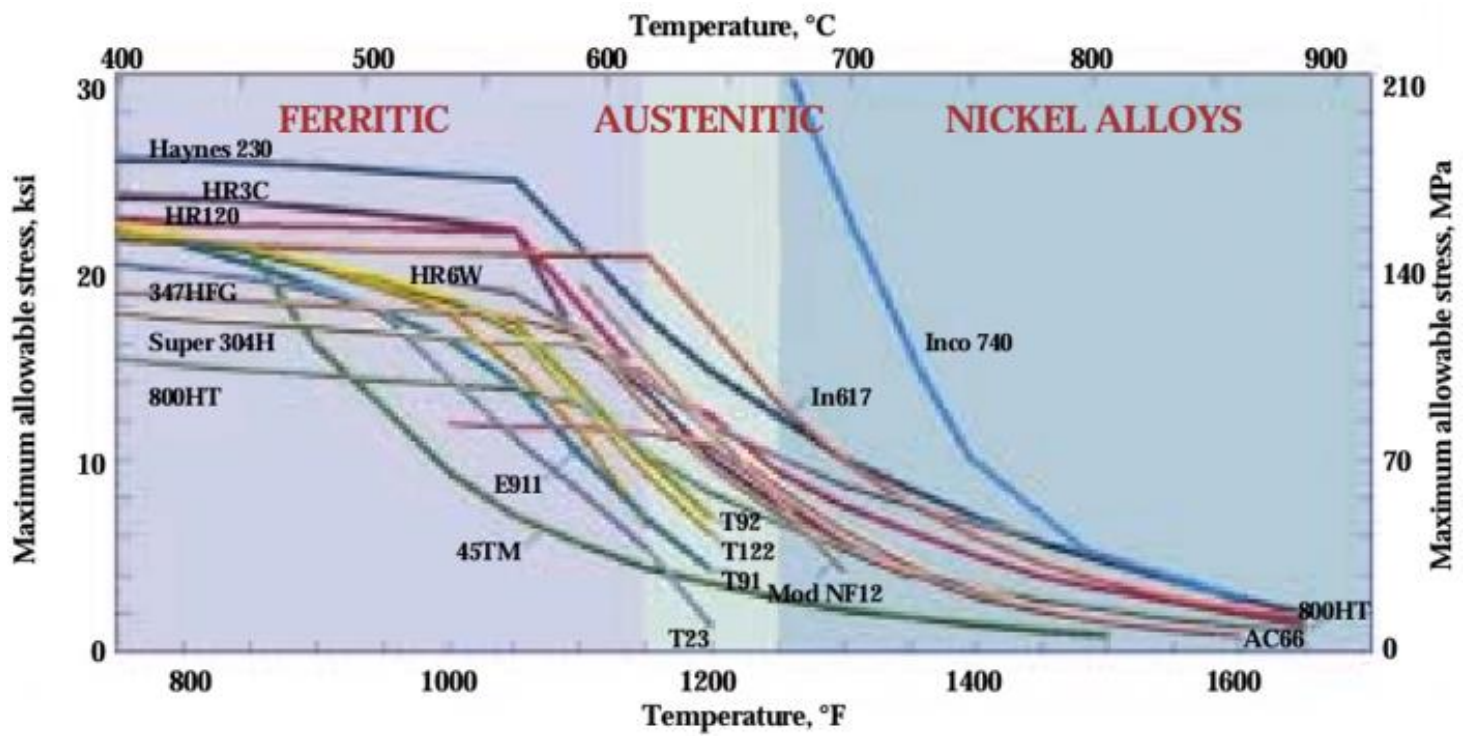


Figure S1: Allowable stress for various classes of alloys (adapted from [40]).

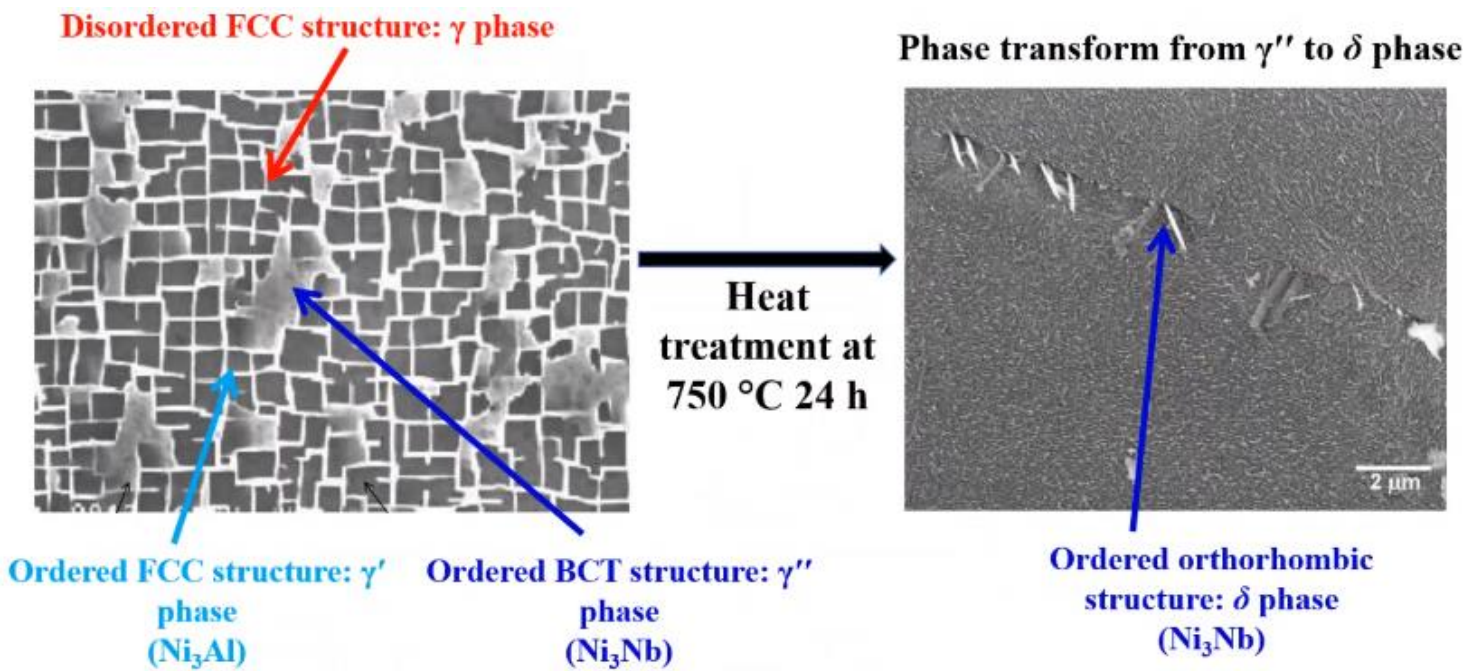
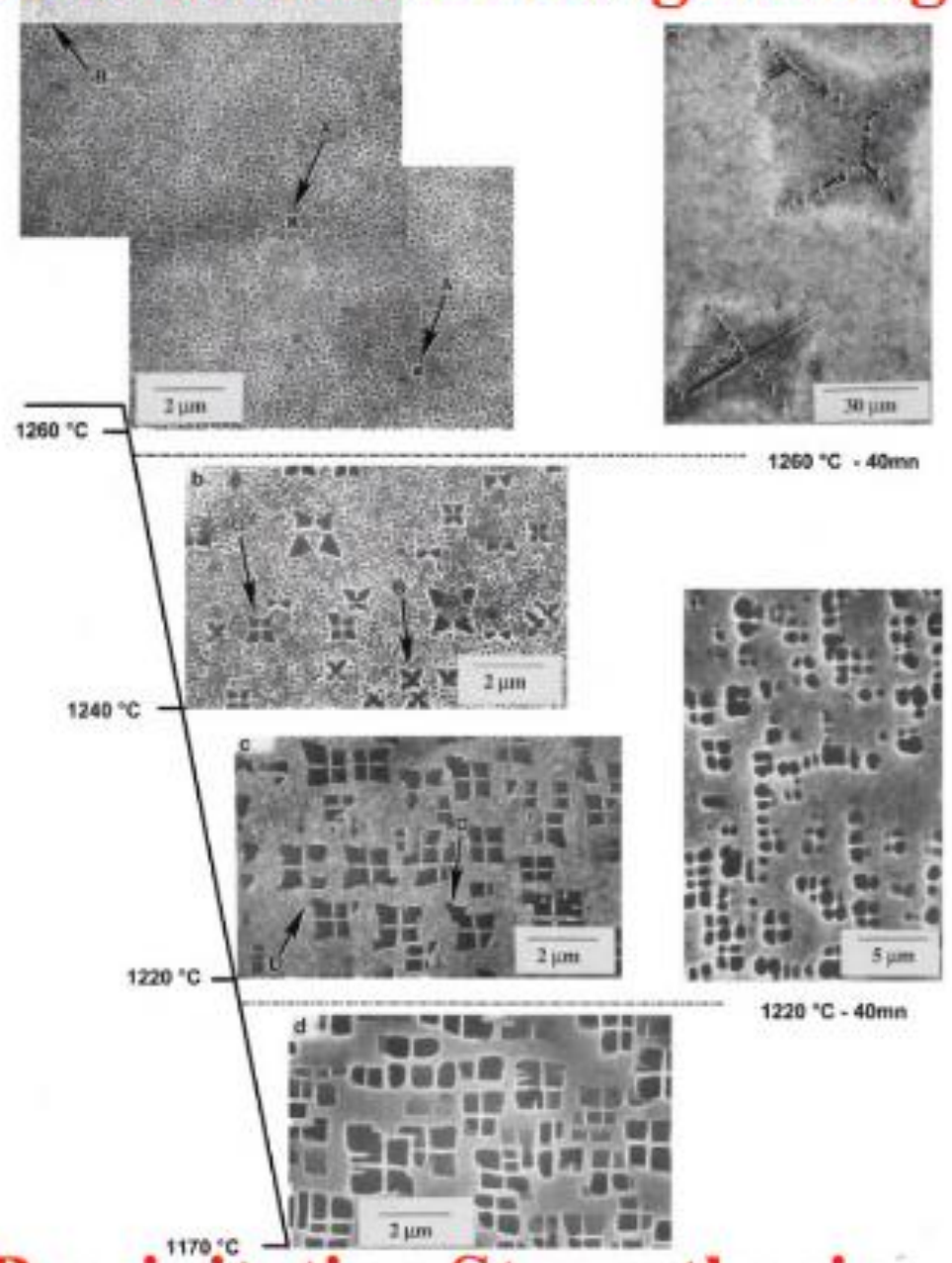


Figure S2: Phase transformations in Ni-based superalloys, caused by dissolution of γ'' phase, at the elevated temperature of 750 °C (adapted from [41]).

High temperature

Moderate temperature

Solid-solution Strengthening



Precipitation Strengthening

Figure S3: For Ni-based superalloys, precipitation strengthening tends to be the main strengthening mechanism at low-to-medium temperatures, but solid-solution strengthening at high temperatures, i.e., at temperatures above 1,260 °C (adapted from [42]).

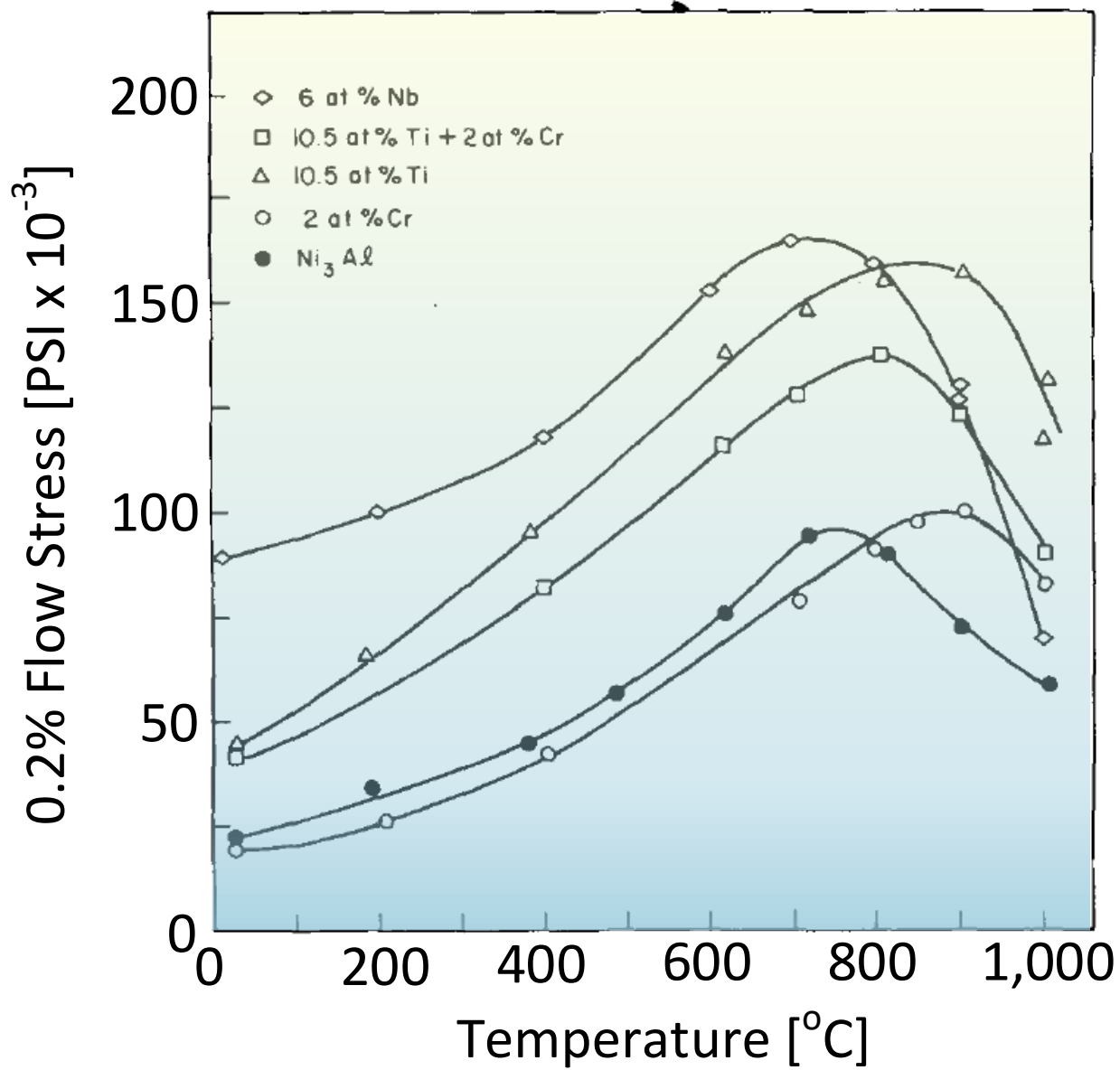


Figure S4: Yield stress vs. temperature for γ' showing the yield stress peak and the influence of solutes on Ni₃Al (adapted from [43]).

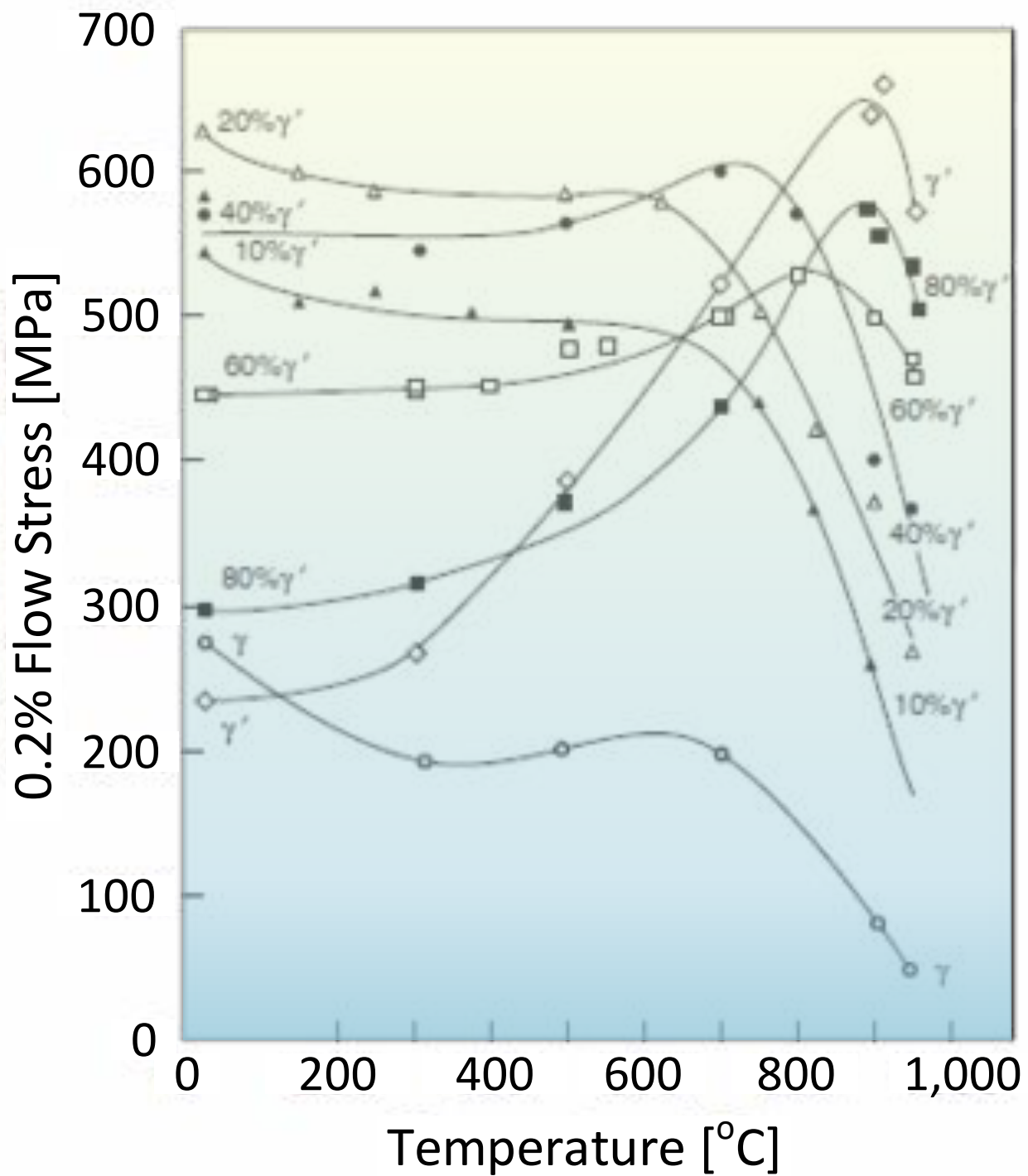


Figure S5: Effects of γ' volume fraction and temperature on yield strength (adapted from [44]).

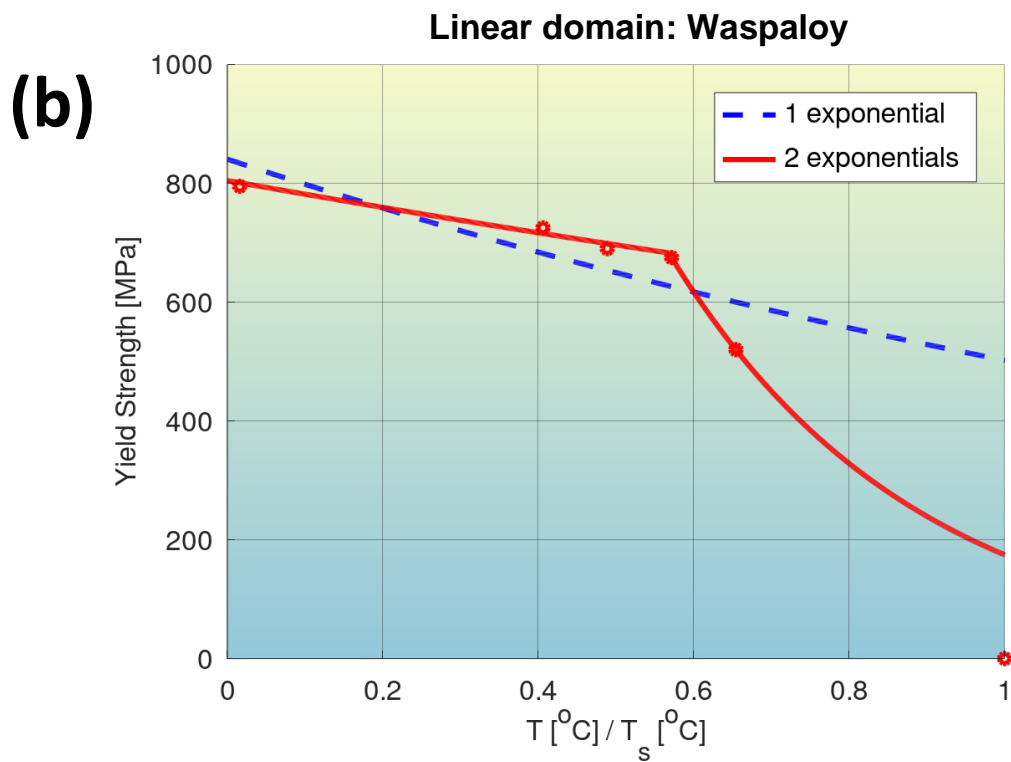
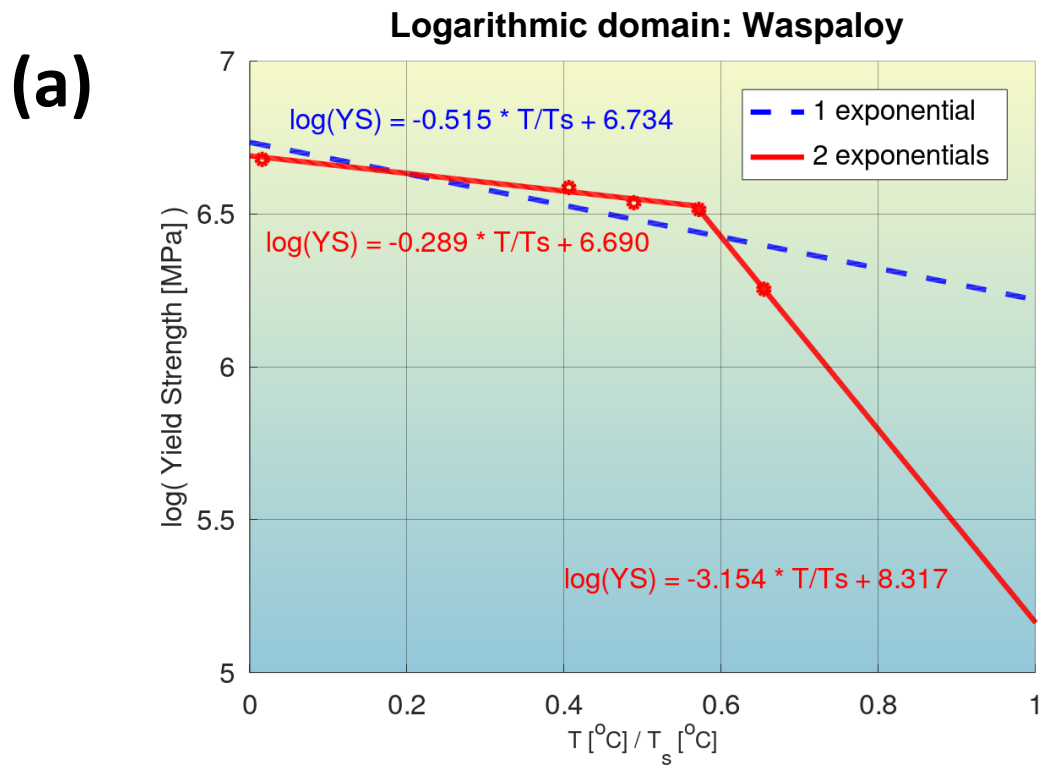


Figure S6: Quantification of modeling accuracy of the bilinear log model, for the composition No. 1 from Table S1 (Waspaloy), and comparison to that of a model with a single exponential.

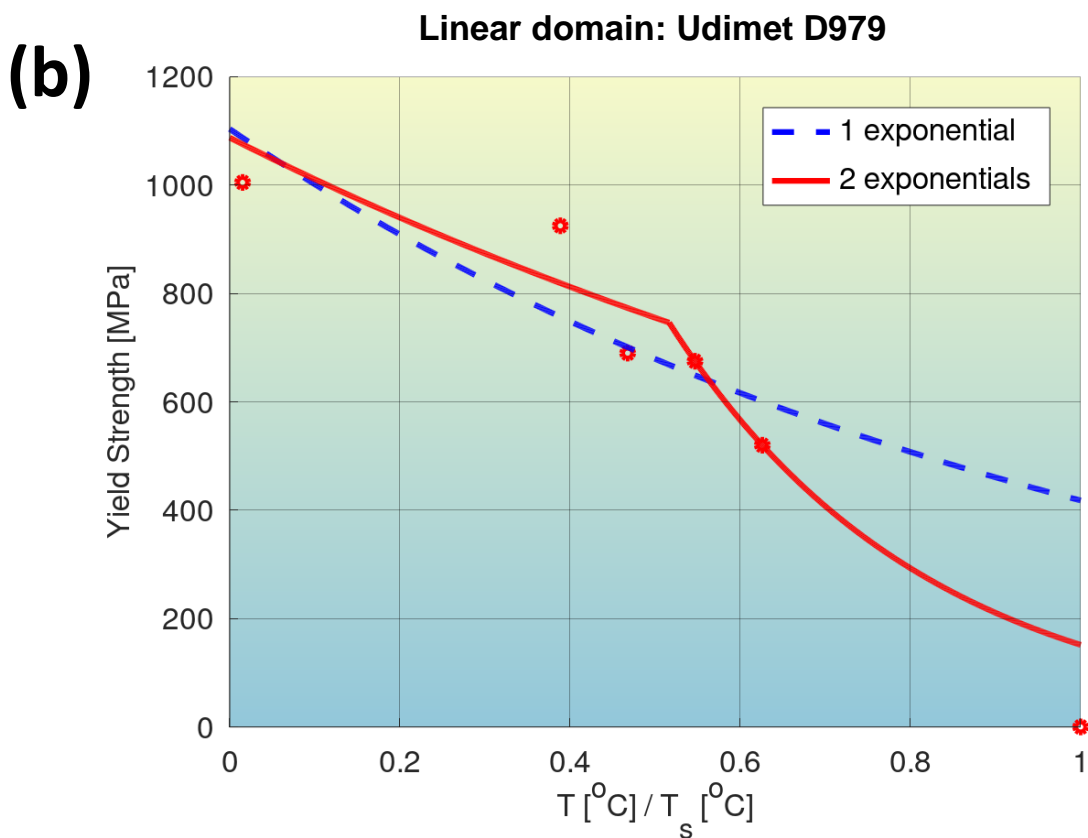
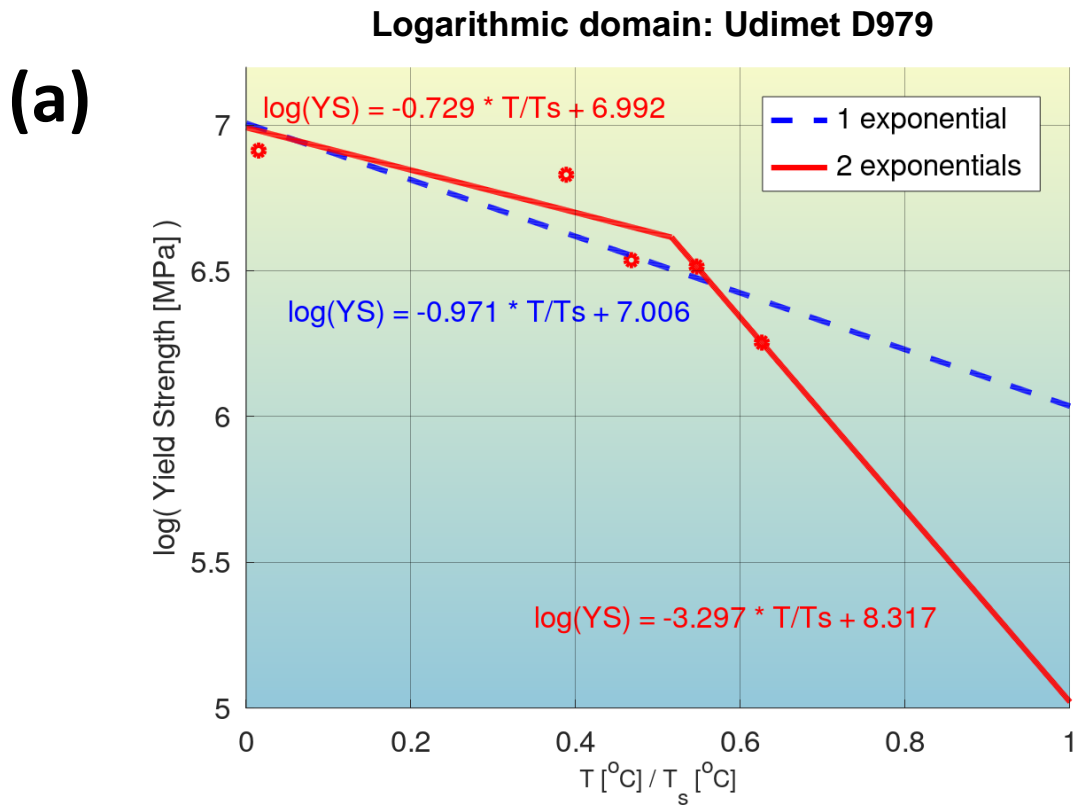


Figure S7: Quantification of modeling accuracy of the bilinear log model, for the composition No. 2 from Table S1 (Udimet D979), and comparison to that of a model with a single exponential.

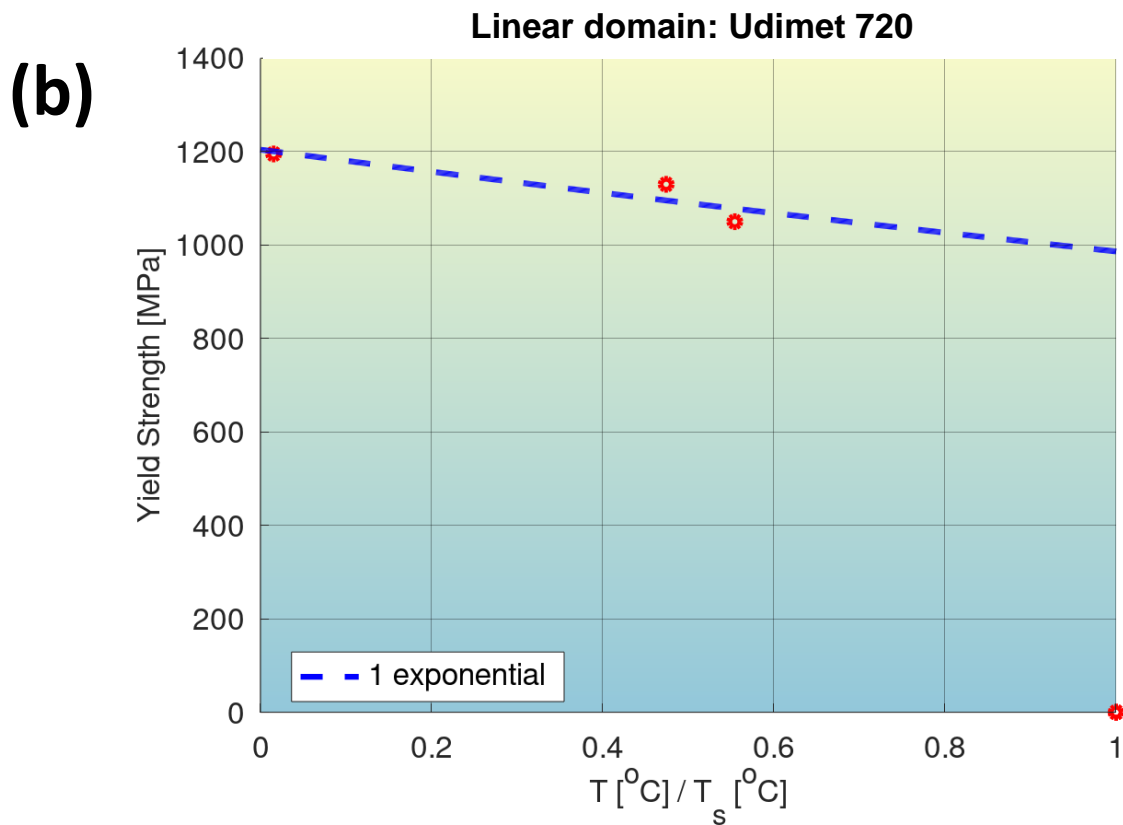
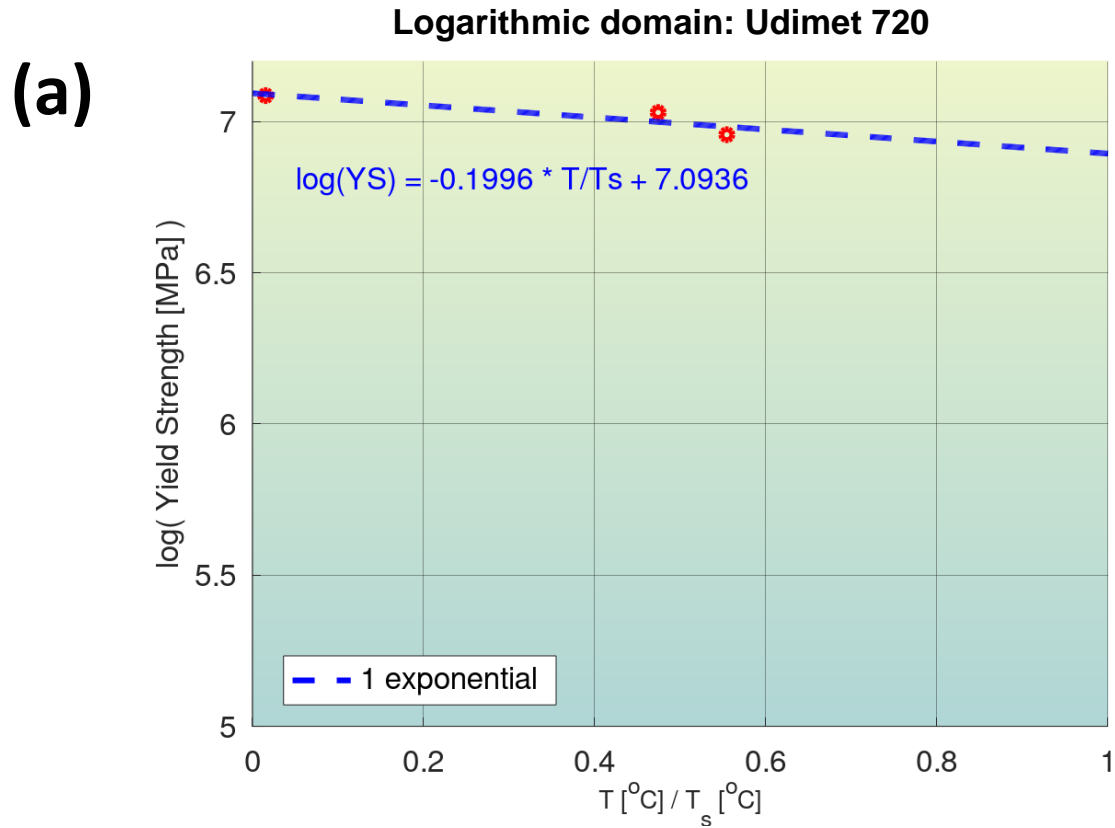


Figure S8: Quantification of modeling accuracy of the bilinear log model, for the composition No. 3 from Table S1 (Udimet 720), and comparison to that of a model with a single exponential.

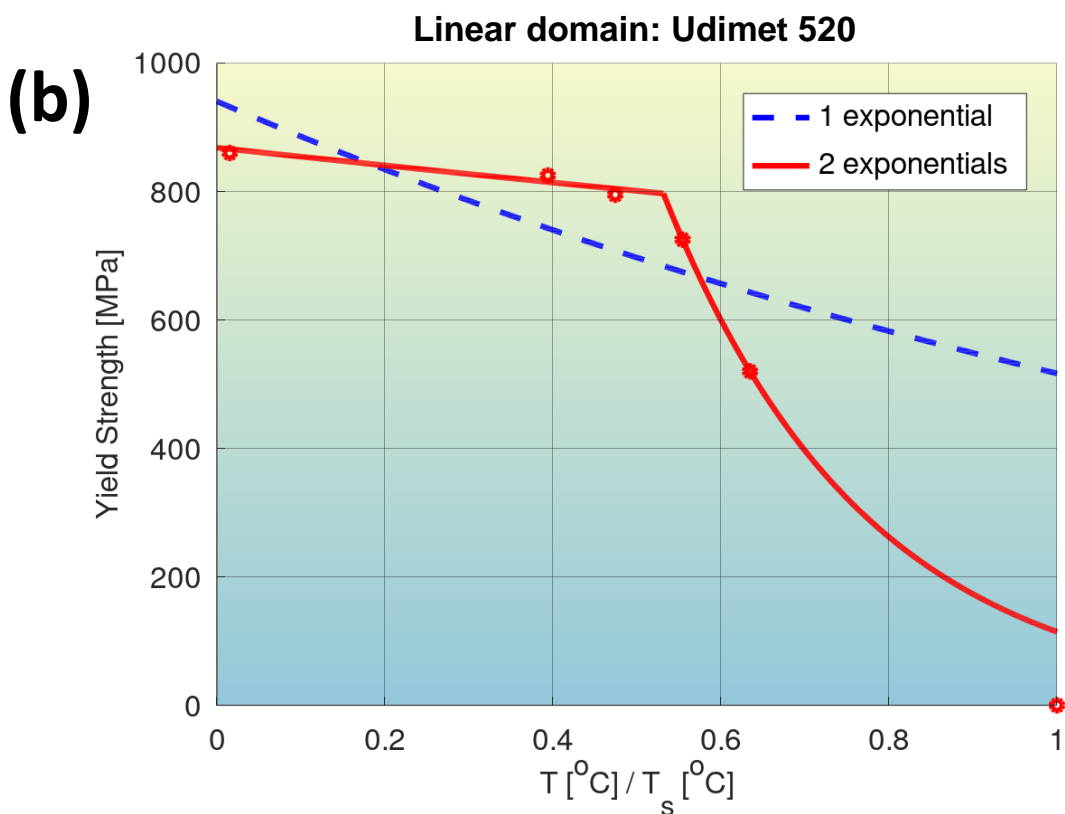
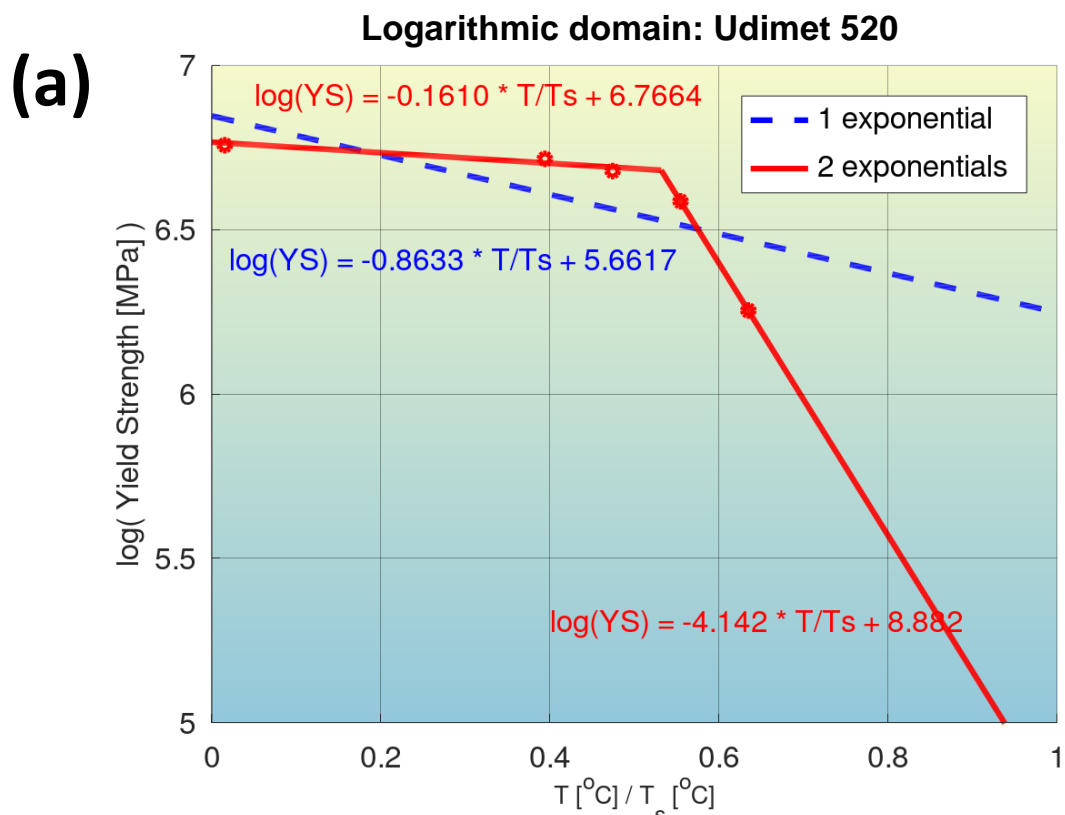


Figure S9: Quantification of modeling accuracy of the bilinear log model, for the composition No. 4 from Table S1 (Udimet 520), and comparison to that of a model with a single exponential.

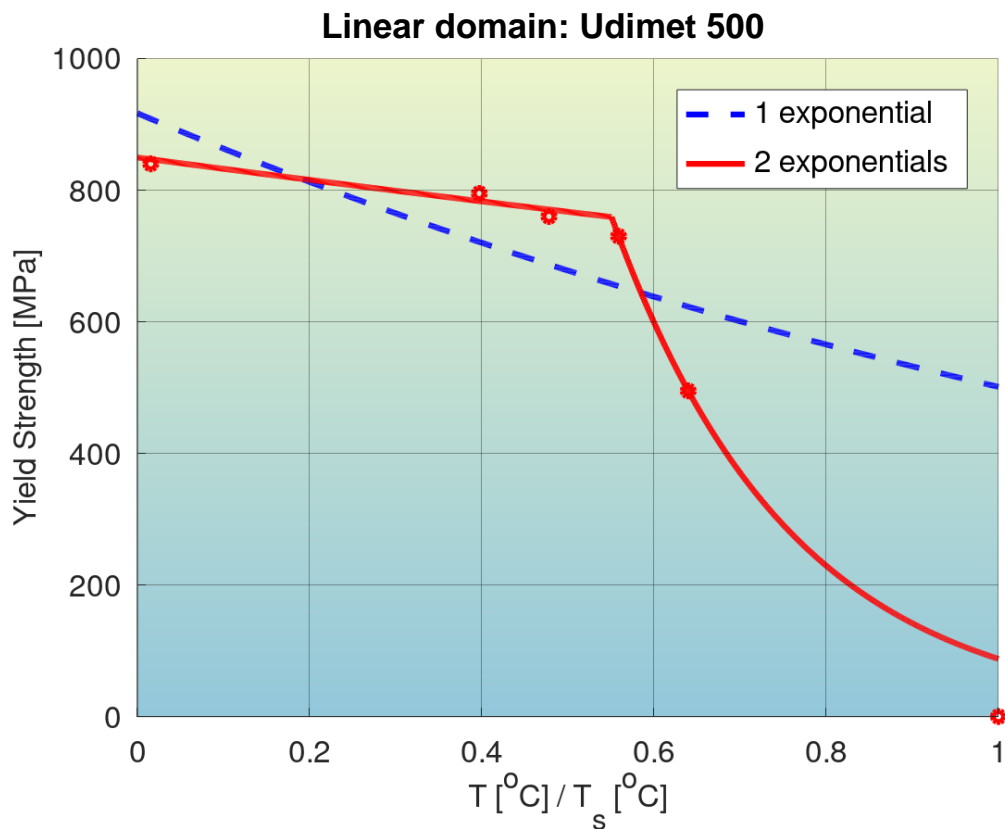
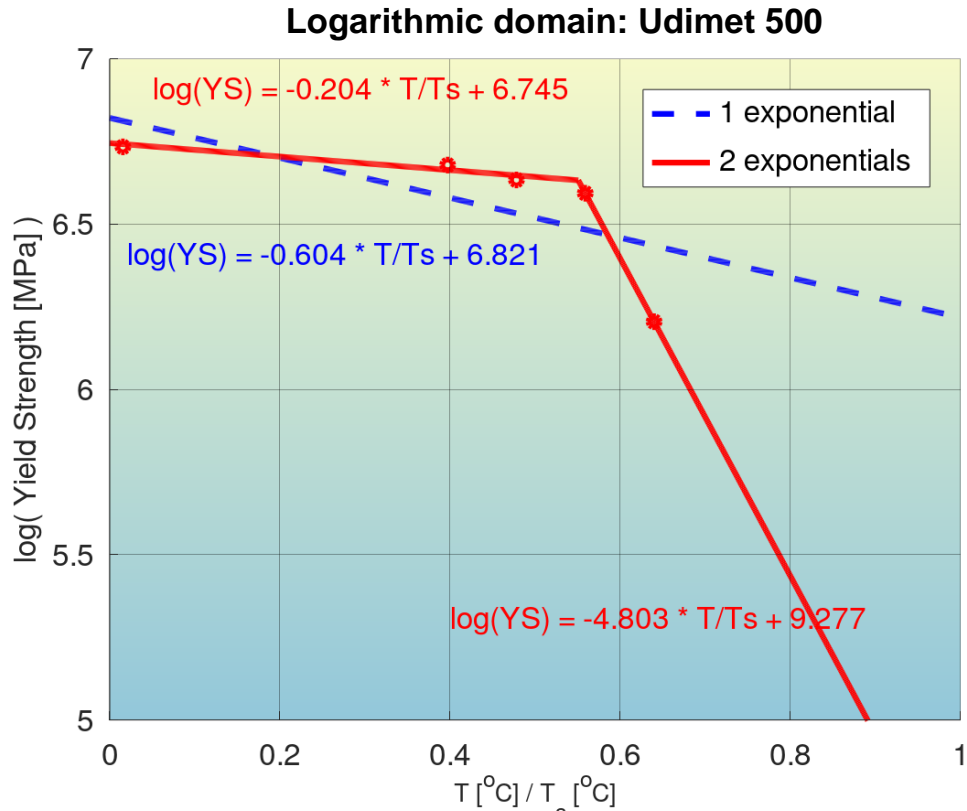
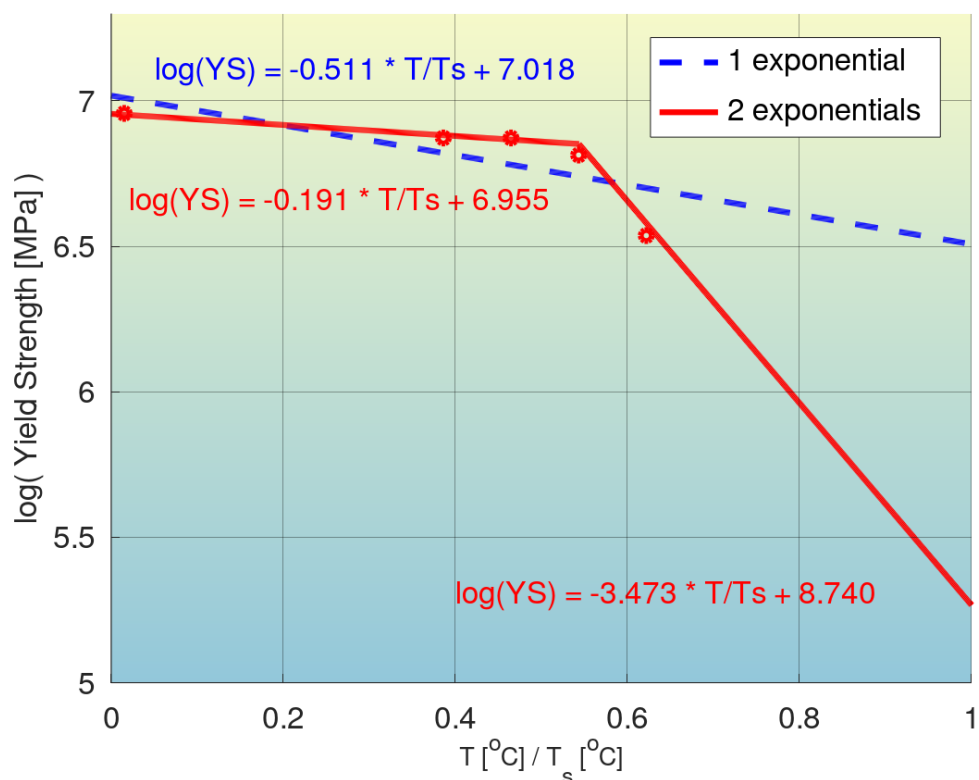


Figure S10: Quantification of modeling accuracy of the bilinear log model, for the composition No. 5 from Table S1 (Udimet 500), and comparison to that of a model with a single exponential.

Logarithmic domain: Astroloy



Linear domain: Astroloy

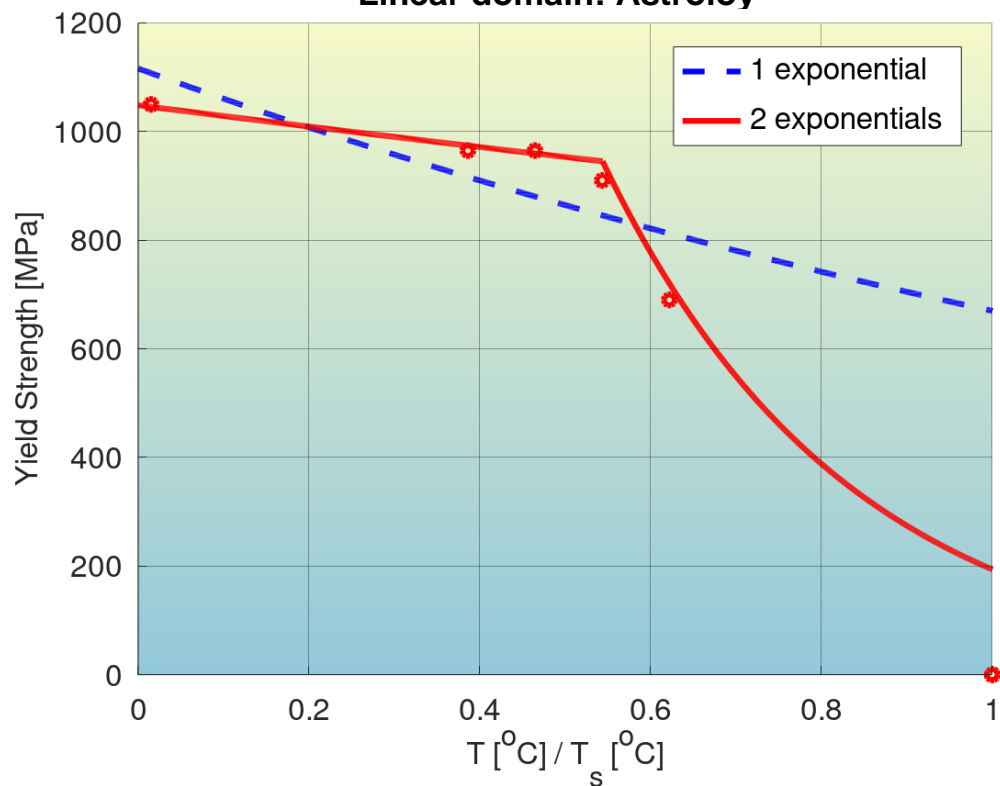


Figure S11: Quantification of modeling accuracy of the bilinear log model, for the composition No. 6 from Table S1 (Astroloy), and comparison to that of a model with a single exponential.

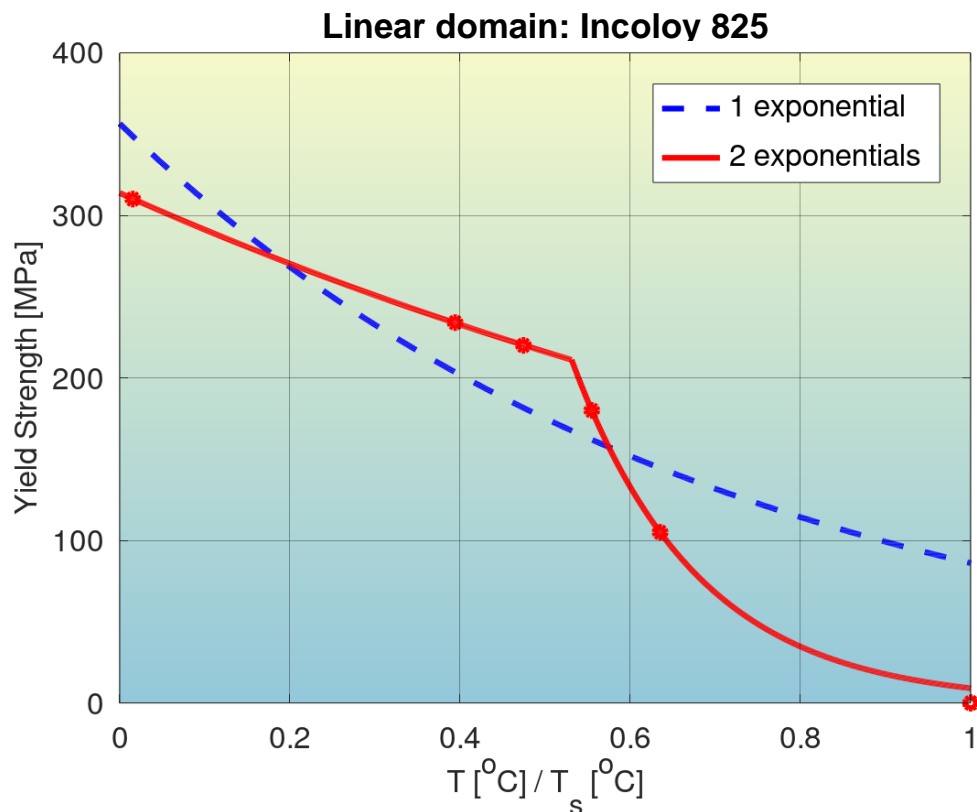
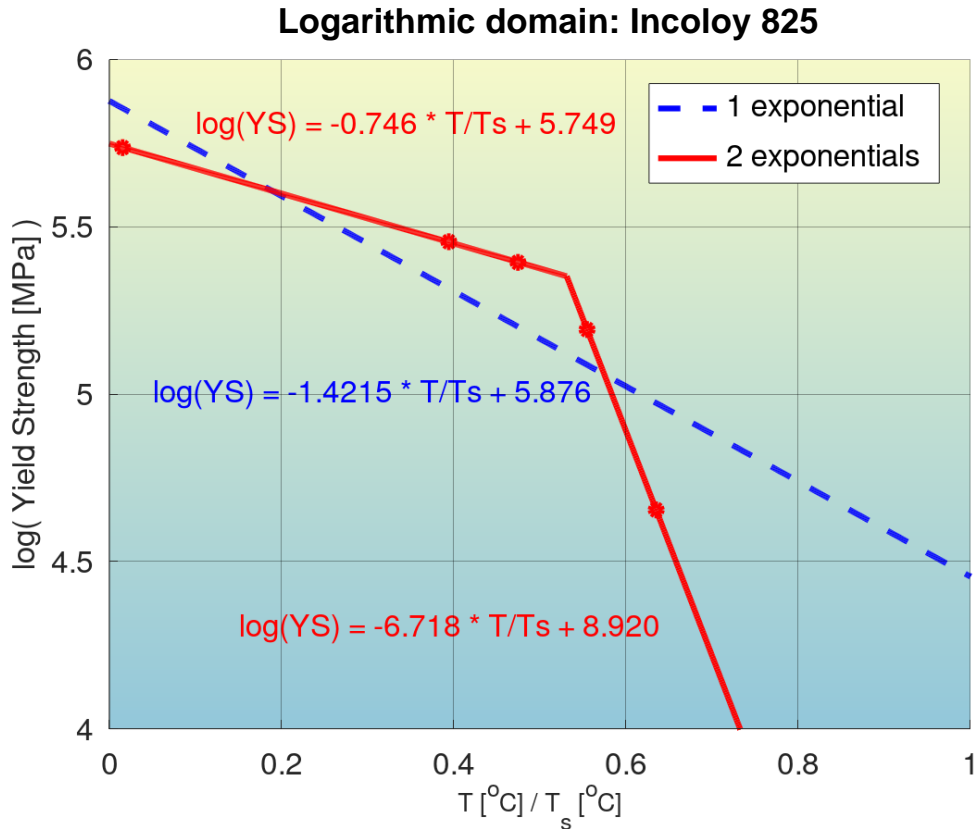


Figure S12: Quantification of modeling accuracy of the bilinear log model, for the composition No. 7 from Table S1 (Incoloy 825), and comparison to that of a model with a single exponential.

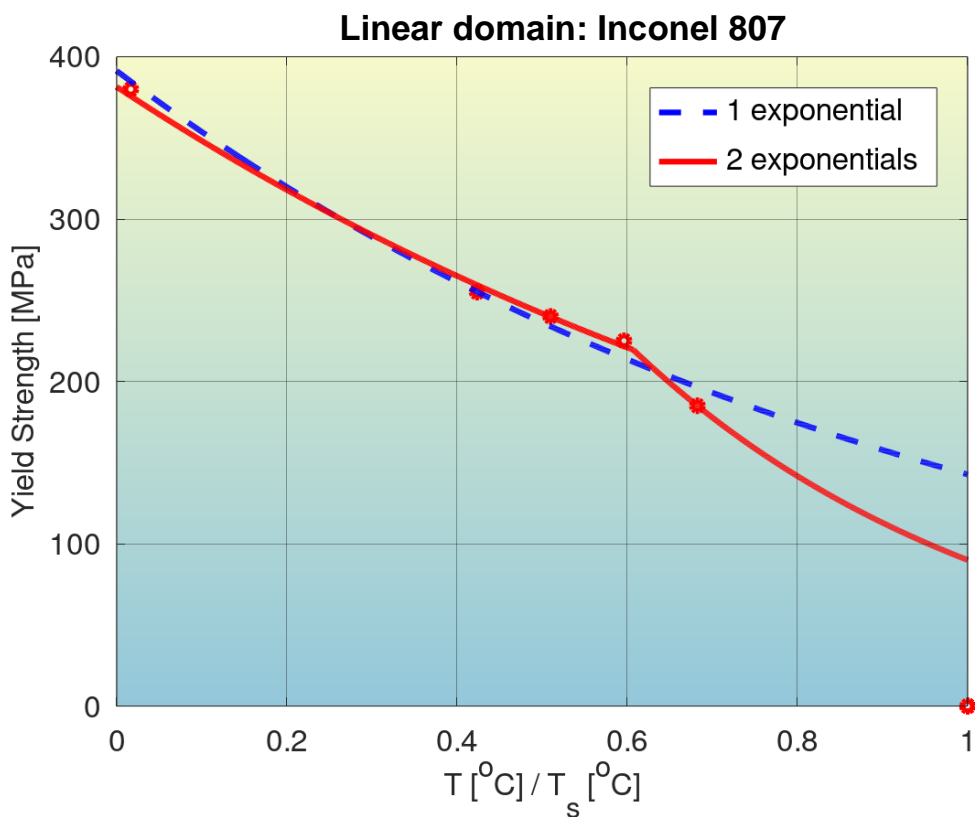
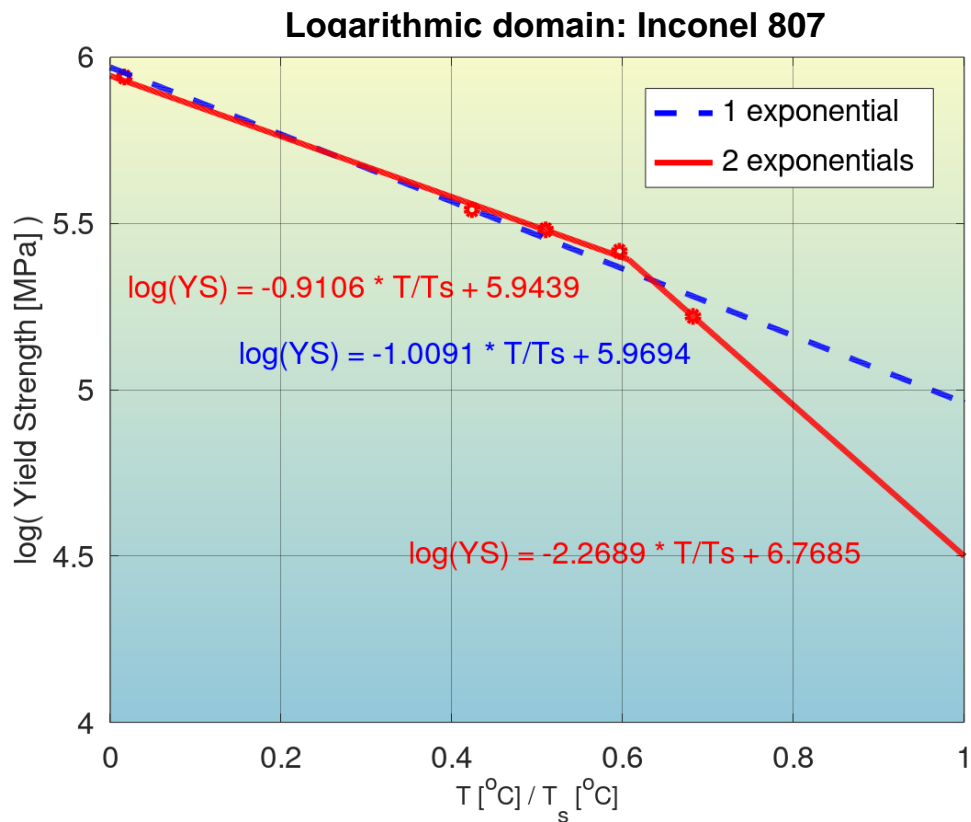


Figure S13: Quantification of modeling accuracy of the bilinear log model, for the composition No. 8 from Table S1 (Inconel 807), and comparison to that of a model with a single exponential.

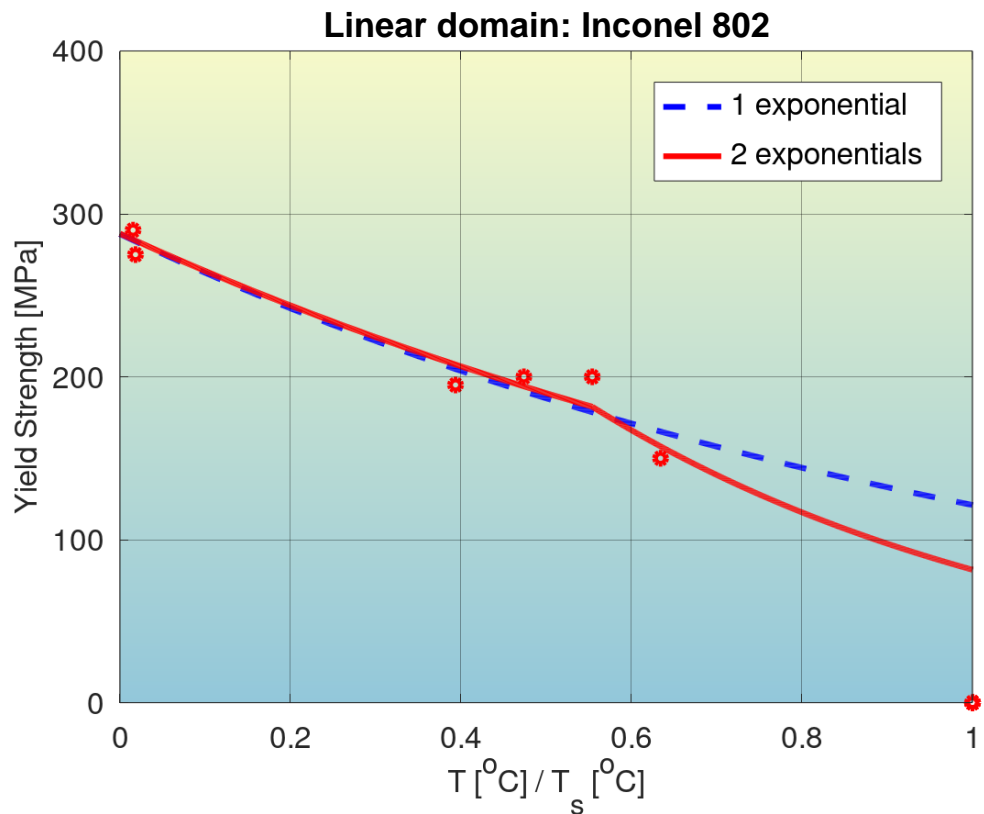
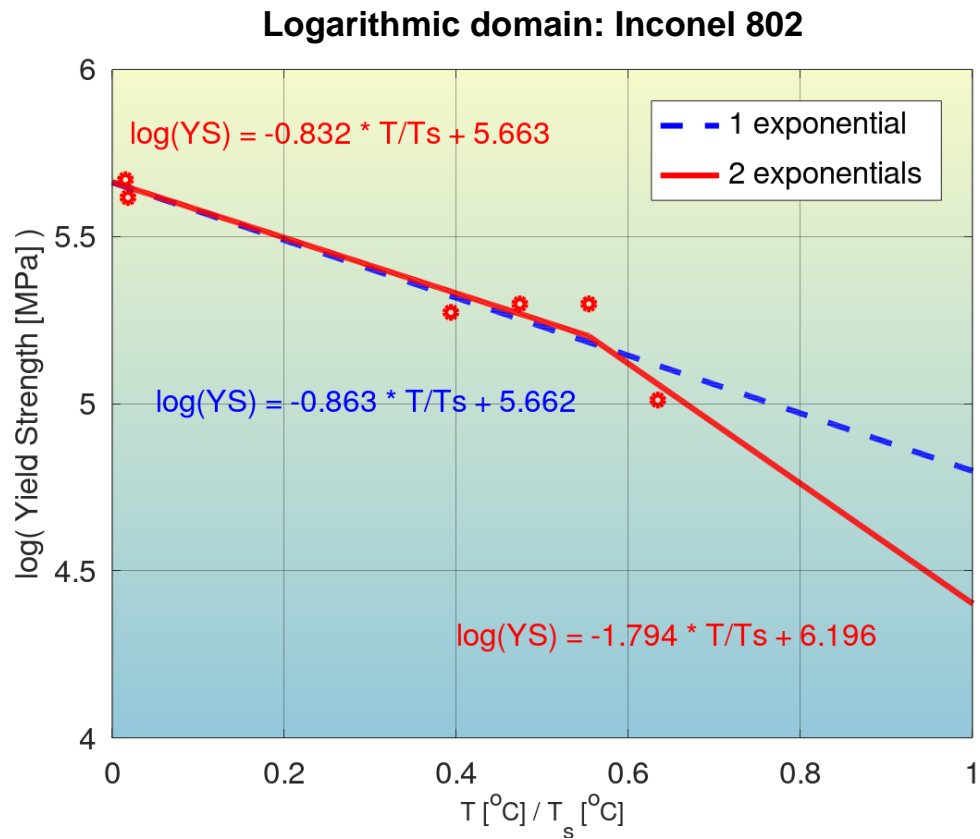


Figure S14: Quantification of modeling accuracy of the bilinear log model, for the composition No. 9 from Table S1 (Inconel 802), and comparison to that of a model with a single exponential.

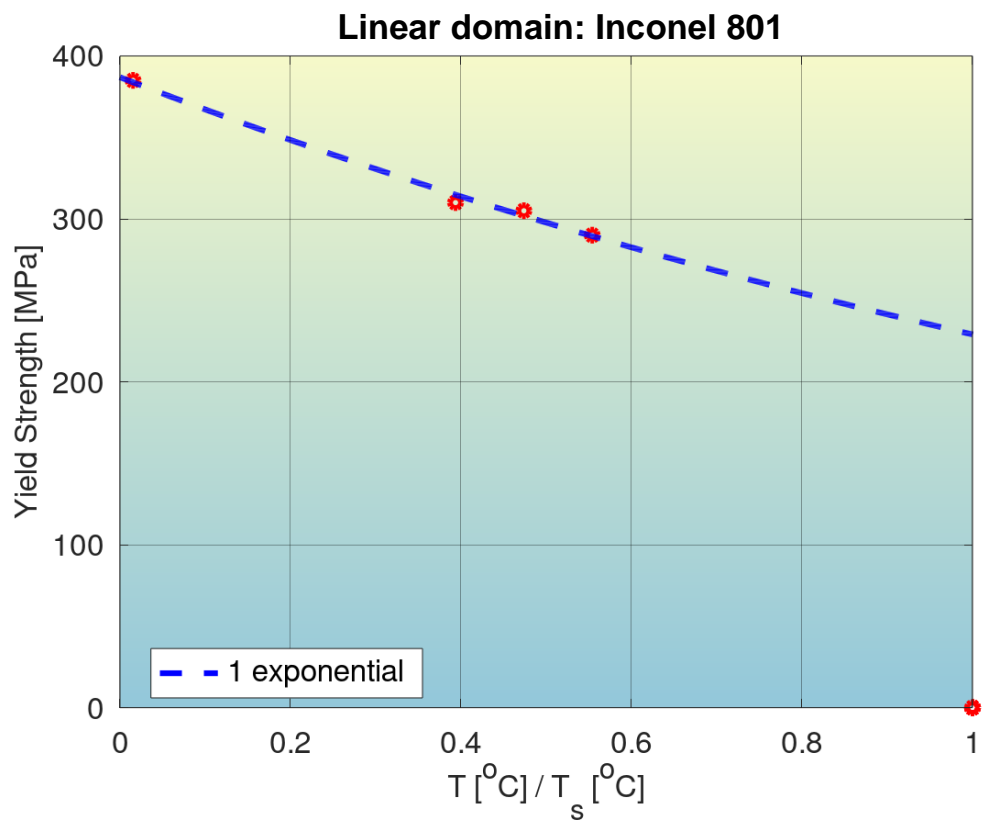
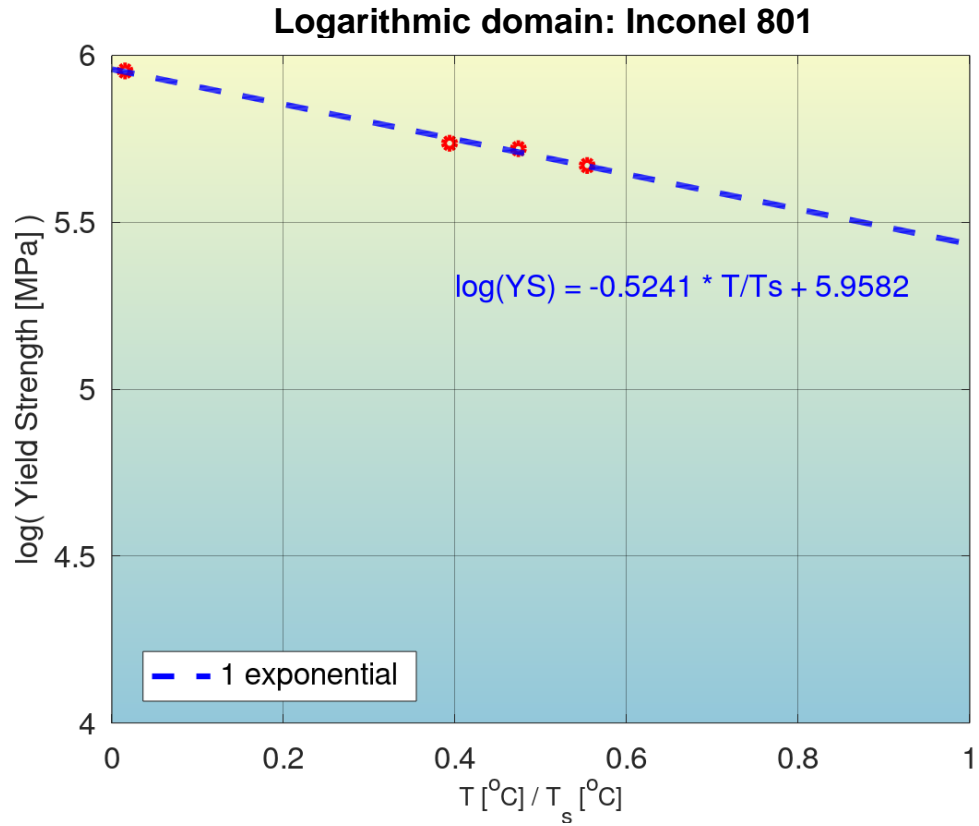


Figure S15: Quantification of modeling accuracy of the bilinear log model, for the composition No. 10 from Table S1 (Inconel 801), and comparison to that of a model with a single exponential.

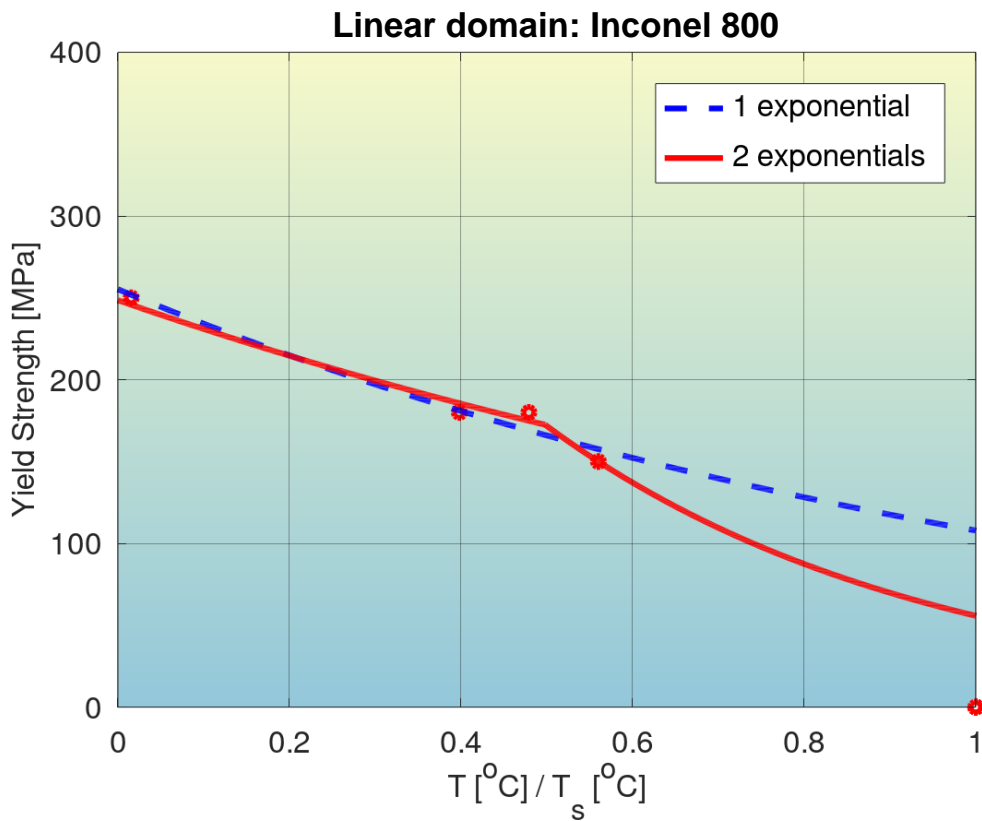
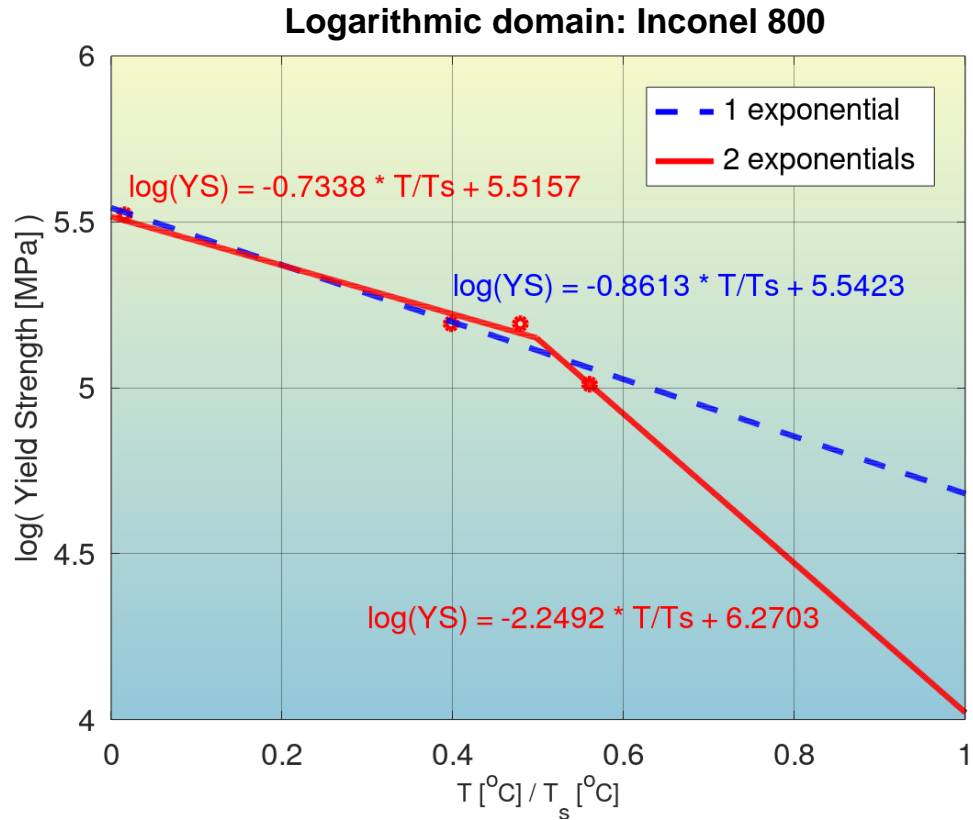
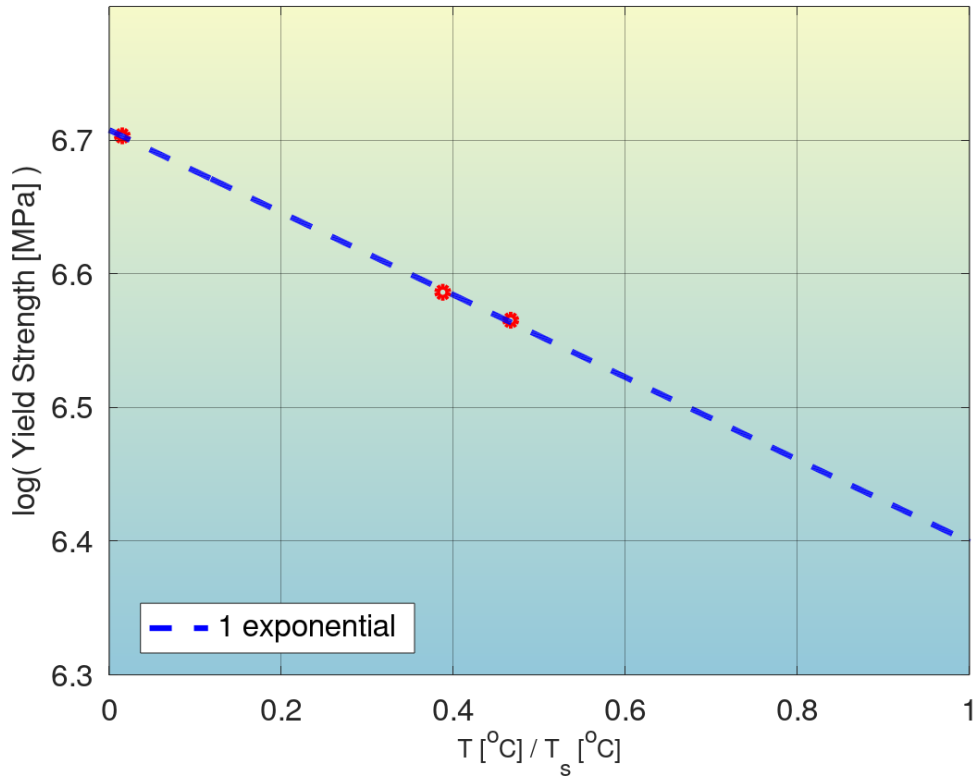


Figure S16: Quantification of modeling accuracy of the bilinear log model, for the composition No. 11 from Table S1 (Inconel 800), and comparison to that of a model with a single exponential.

Logarithmic domain: Inconel X750



Linear domain: Inconel X750

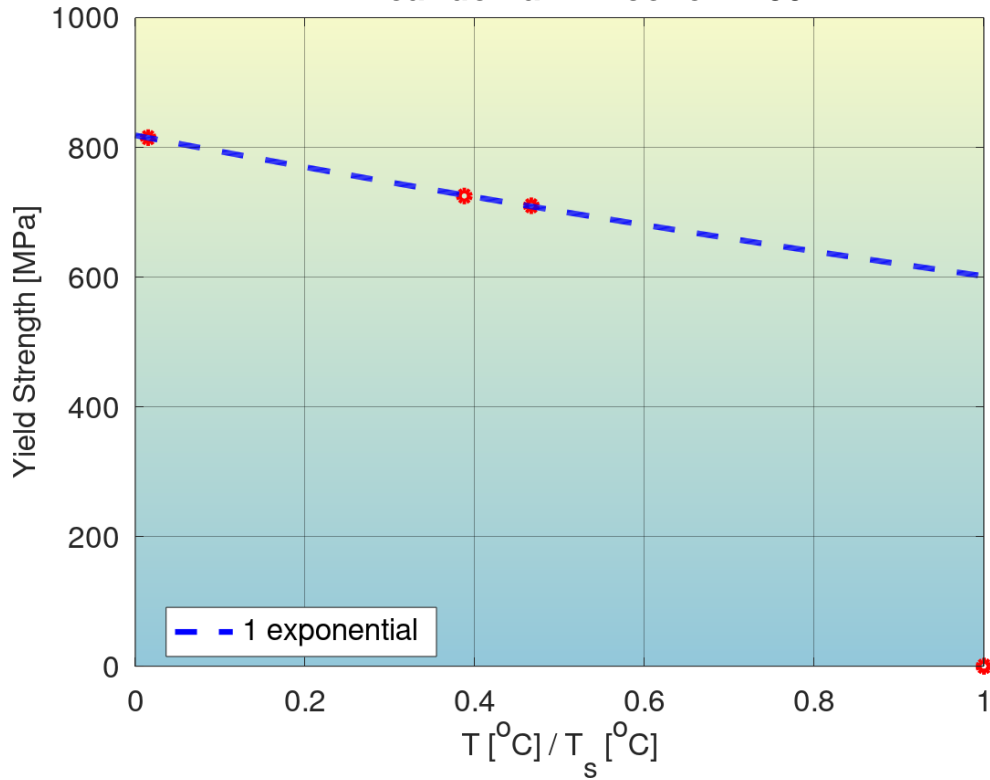


Figure S17: Quantification of modeling accuracy of the bilinear log model, for the composition No. 13 from Table S1 (Inconel X750), and comparison to that of a model with a single exponential.

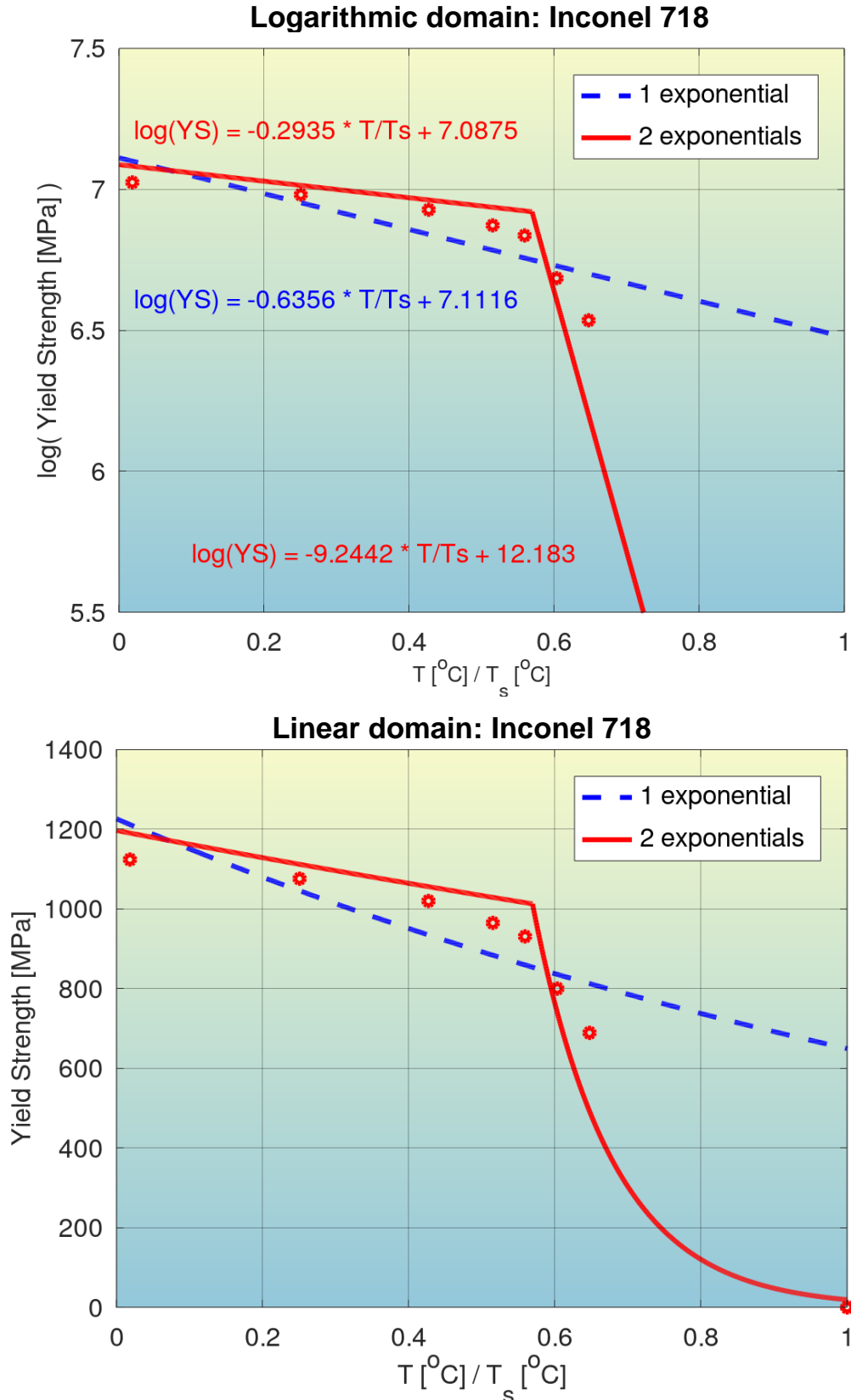


Figure S18: Quantification of modeling accuracy of the bilinear log model, for the composition No. 14 from Table S1 (Inconel 718), and comparison to that of a model with a single exponential.

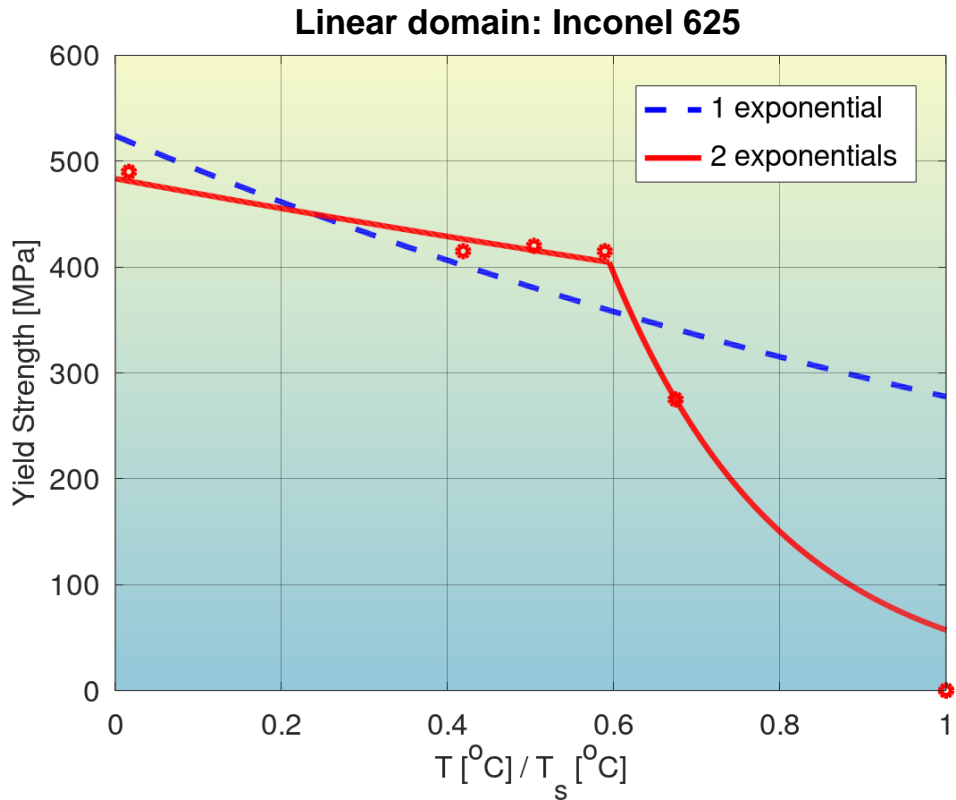
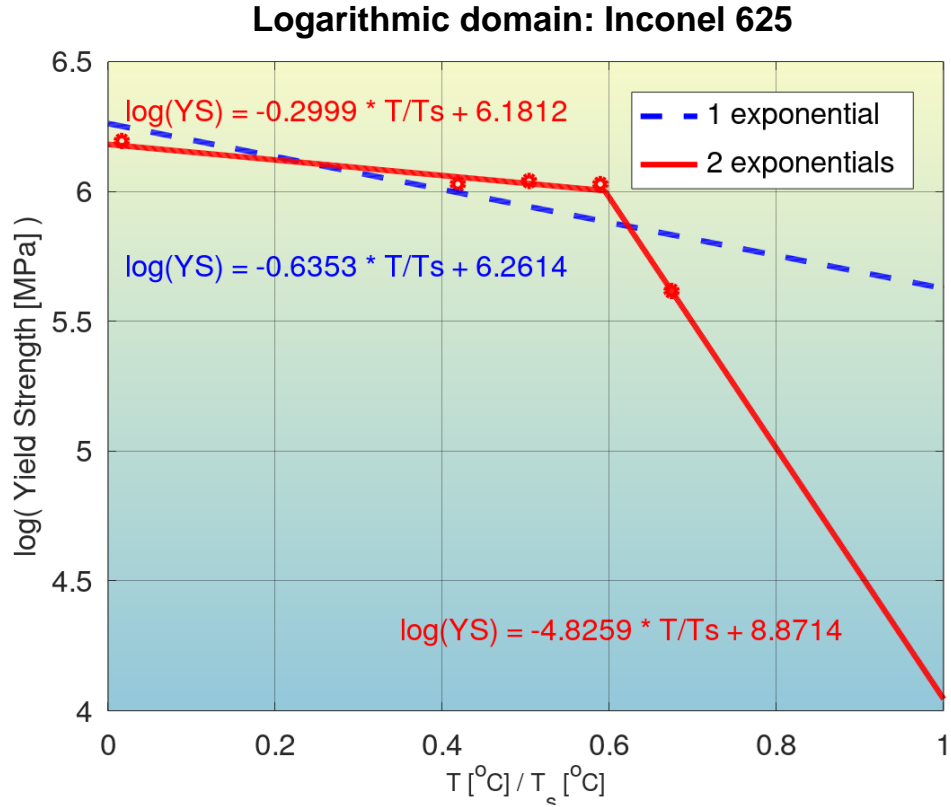


Figure S19: Quantification of modeling accuracy of the bilinear log model, for the composition No. 15 from Table S1 (Inconel 625), and comparison to that of a model with a single exponential. The outlier at room temperature has been excluded from modeling.

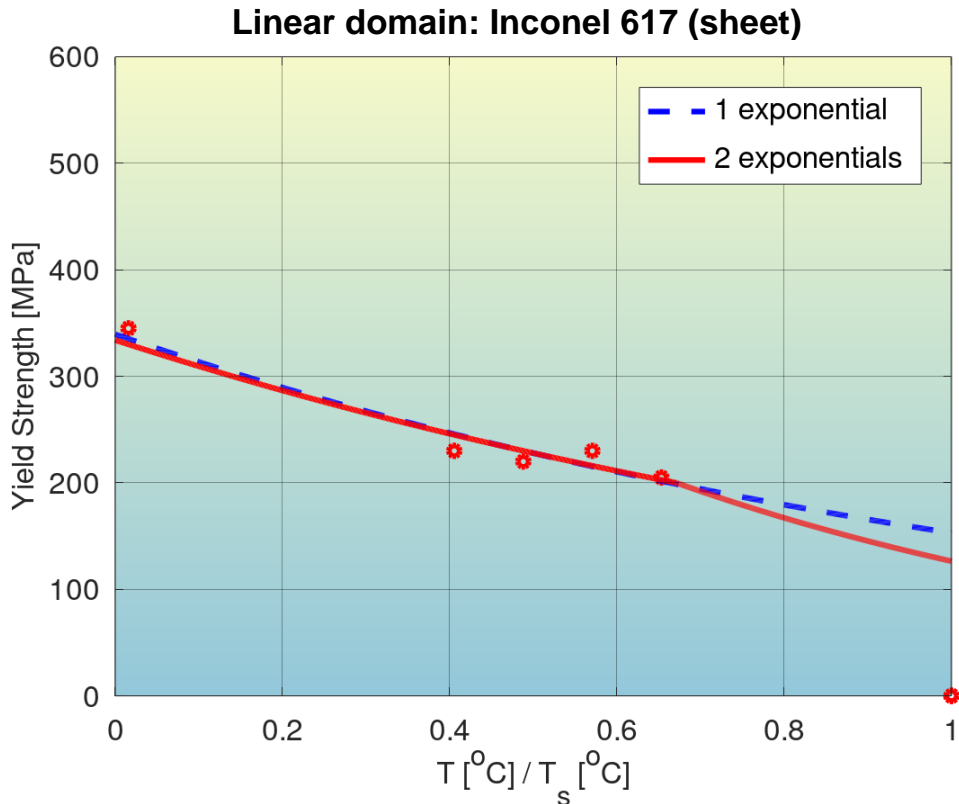
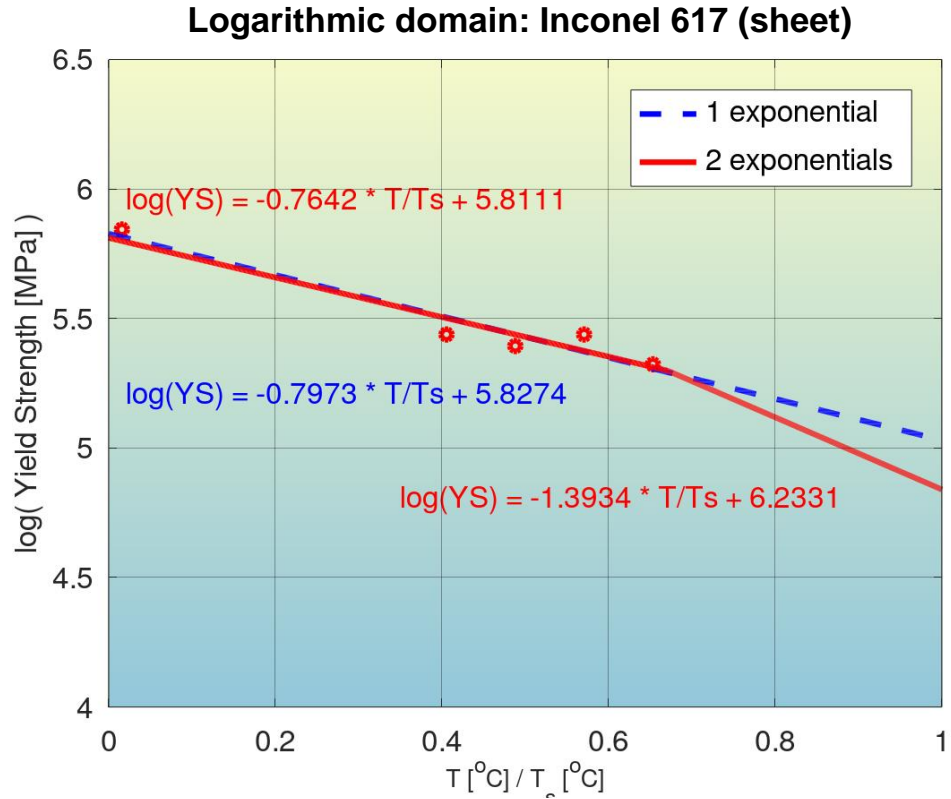


Figure S20: Quantification of modeling accuracy of the bilinear log model, for the composition No. 16 from Table S1 (Inconel 617 sheet), and comparison to that of a model with a single exponential. One outlier has been excluded from the modeling.

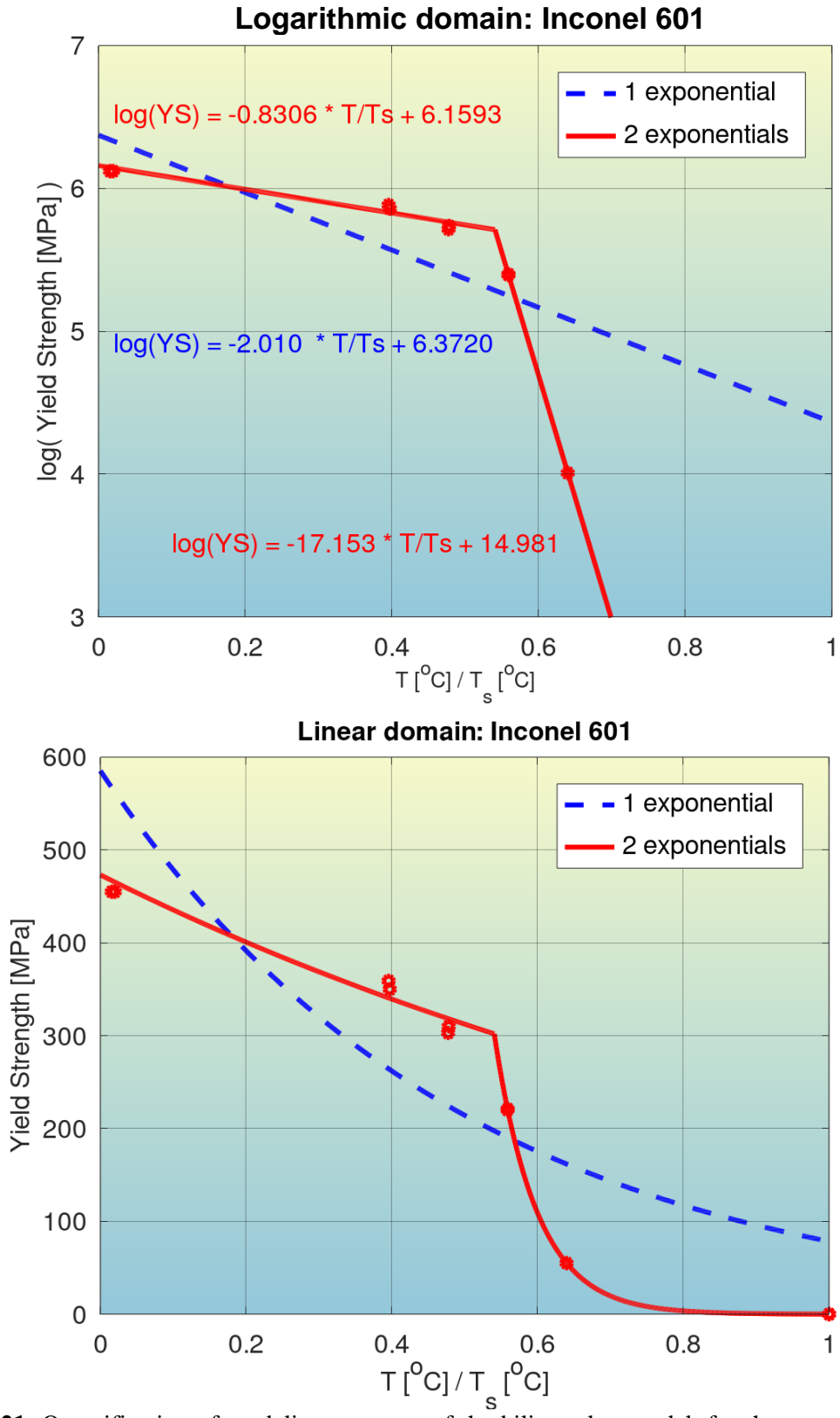


Figure S21: Quantification of modeling accuracy of the bilinear log model, for the composition No. 17 from Table S1 (Inconel 601), and comparison to that of a model with a single exponential. One outlier has been excluded from the modeling.

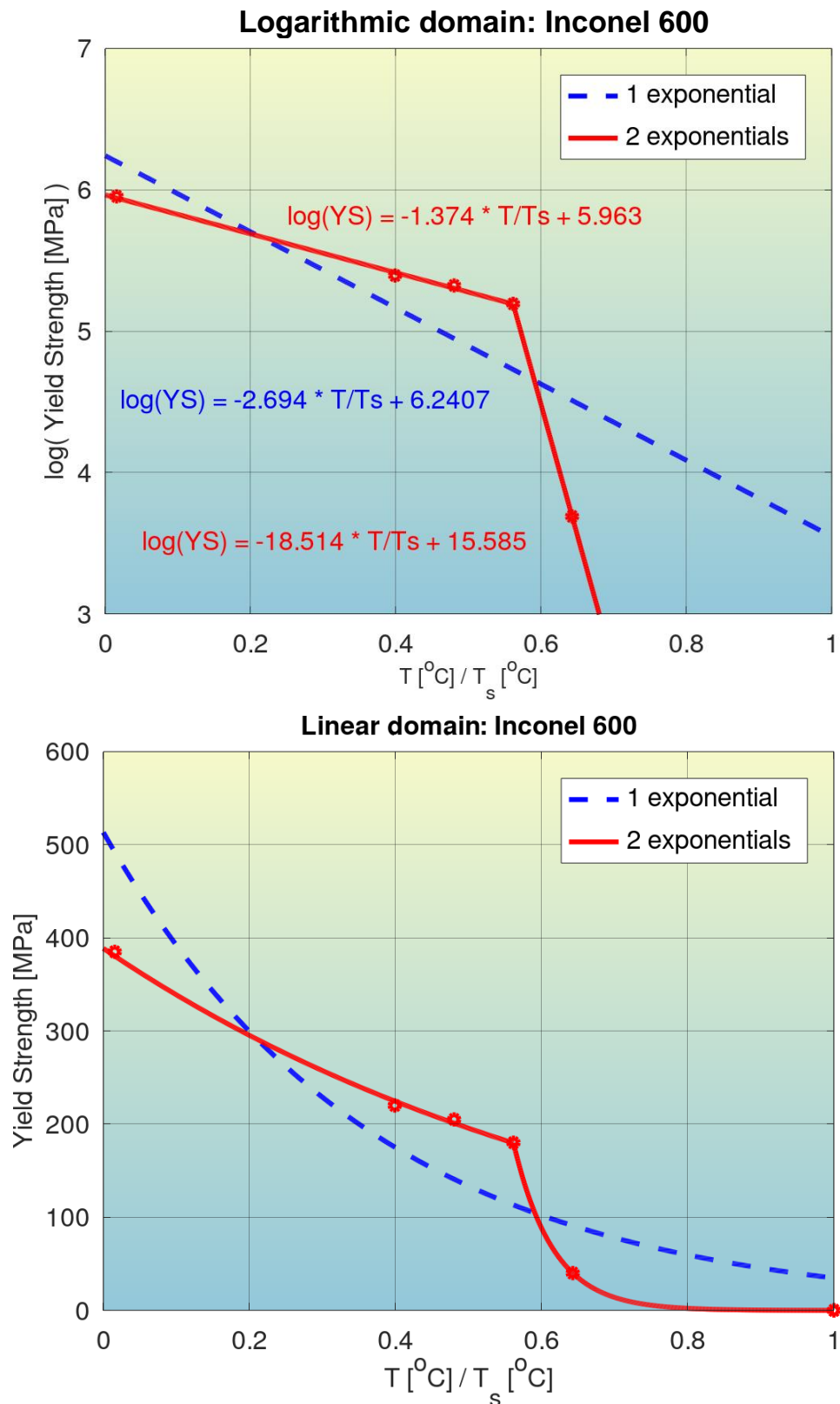


Figure S22: Quantification of modeling accuracy of the bilinear log model, for the composition No. 18 from Table S1 (Inconel 600), and comparison to that of a model with a single exponential. One outlier has been excluded from the modeling.

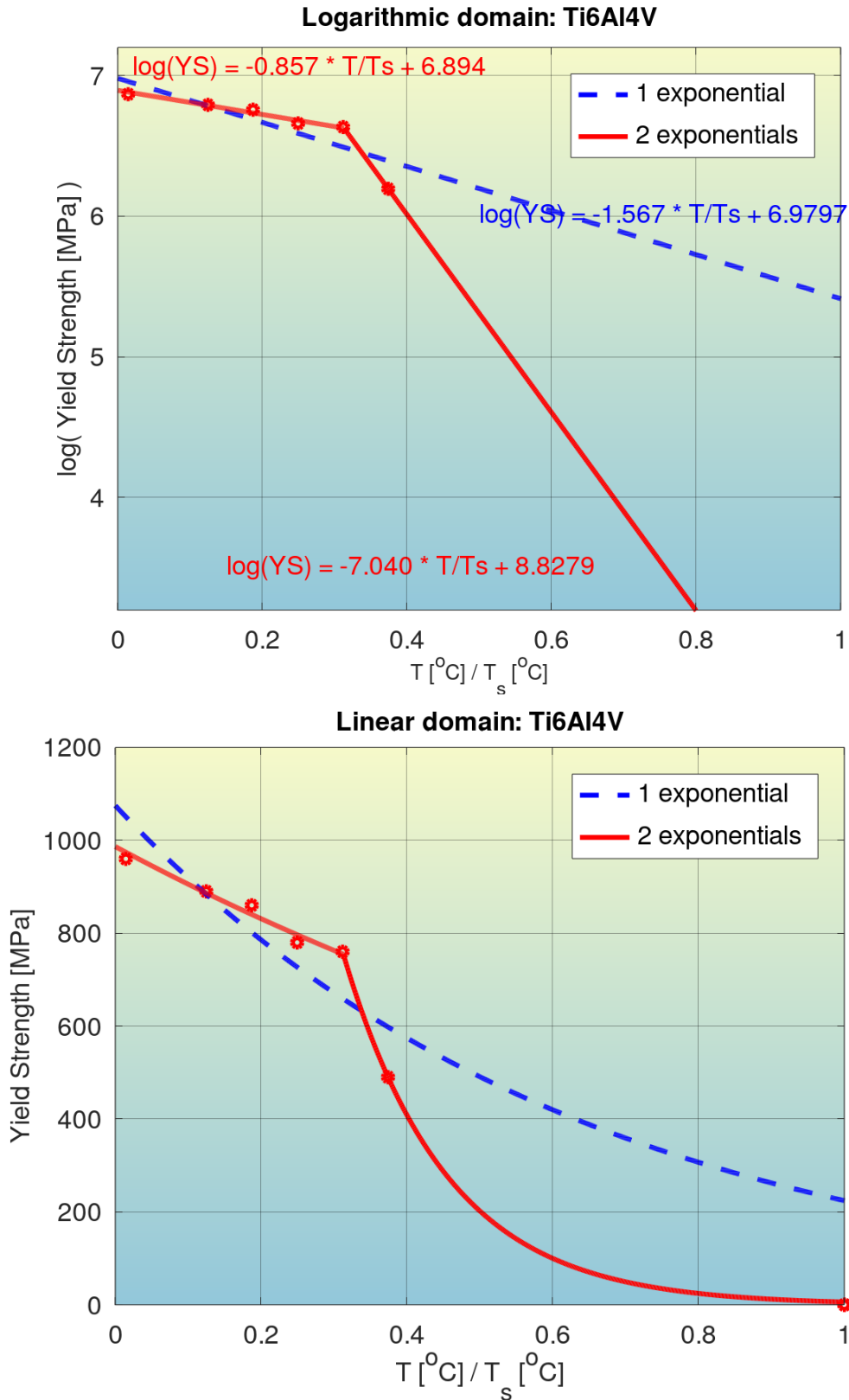


Figure S23: Quantification of modeling accuracy of the bilinear log model, for the composition No. 19 from Table S1 ($\text{Ti}_6\text{Al}_4\text{V}$), and comparison to that of a model with a single exponential. One outlier has been excluded from the modeling.

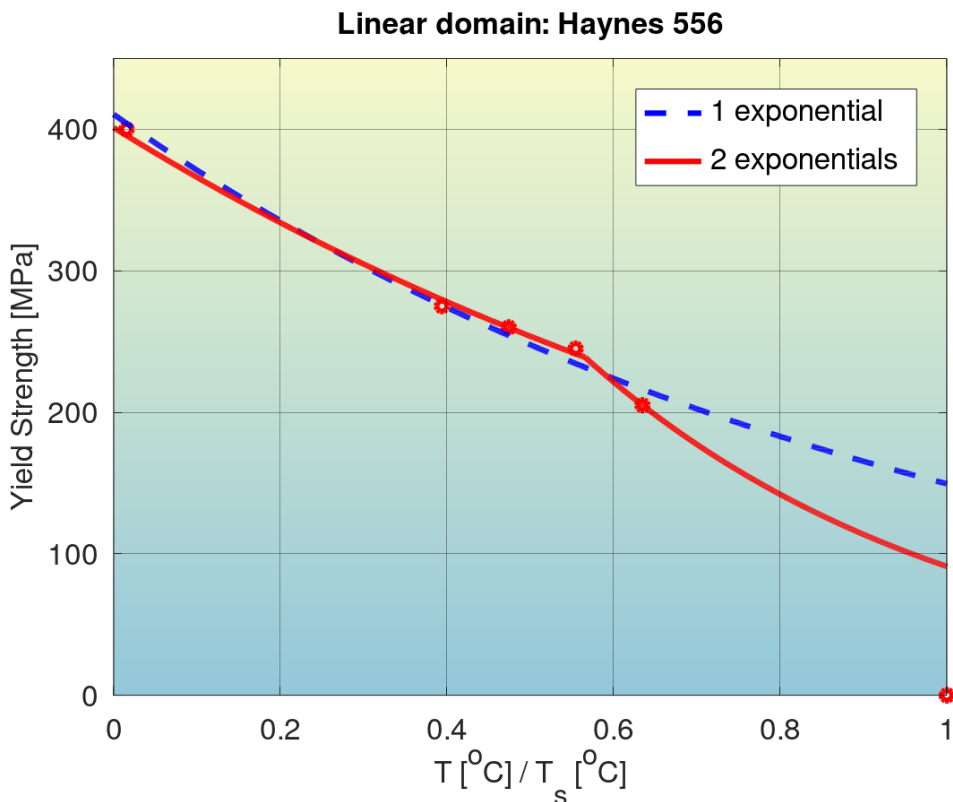
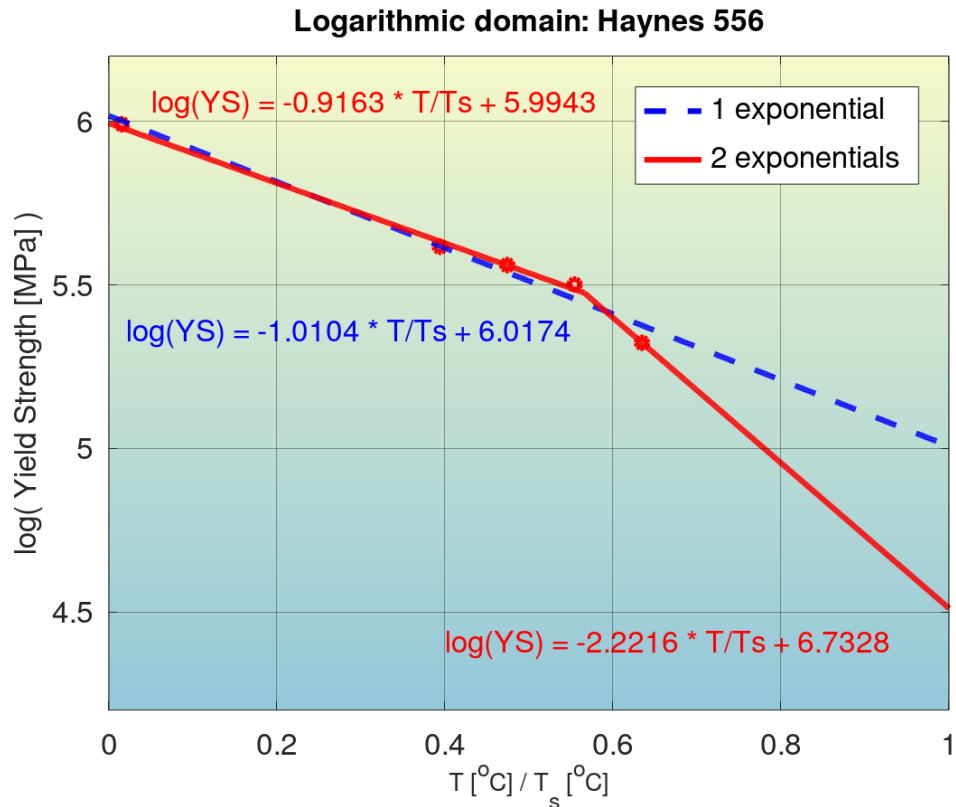


Figure S24: Quantification of modeling accuracy of the bilinear log model, for the composition No. 20 from Table S1 (Haynes 556), and comparison to that of a model with a single exponential. One outlier has been excluded from the modeling.

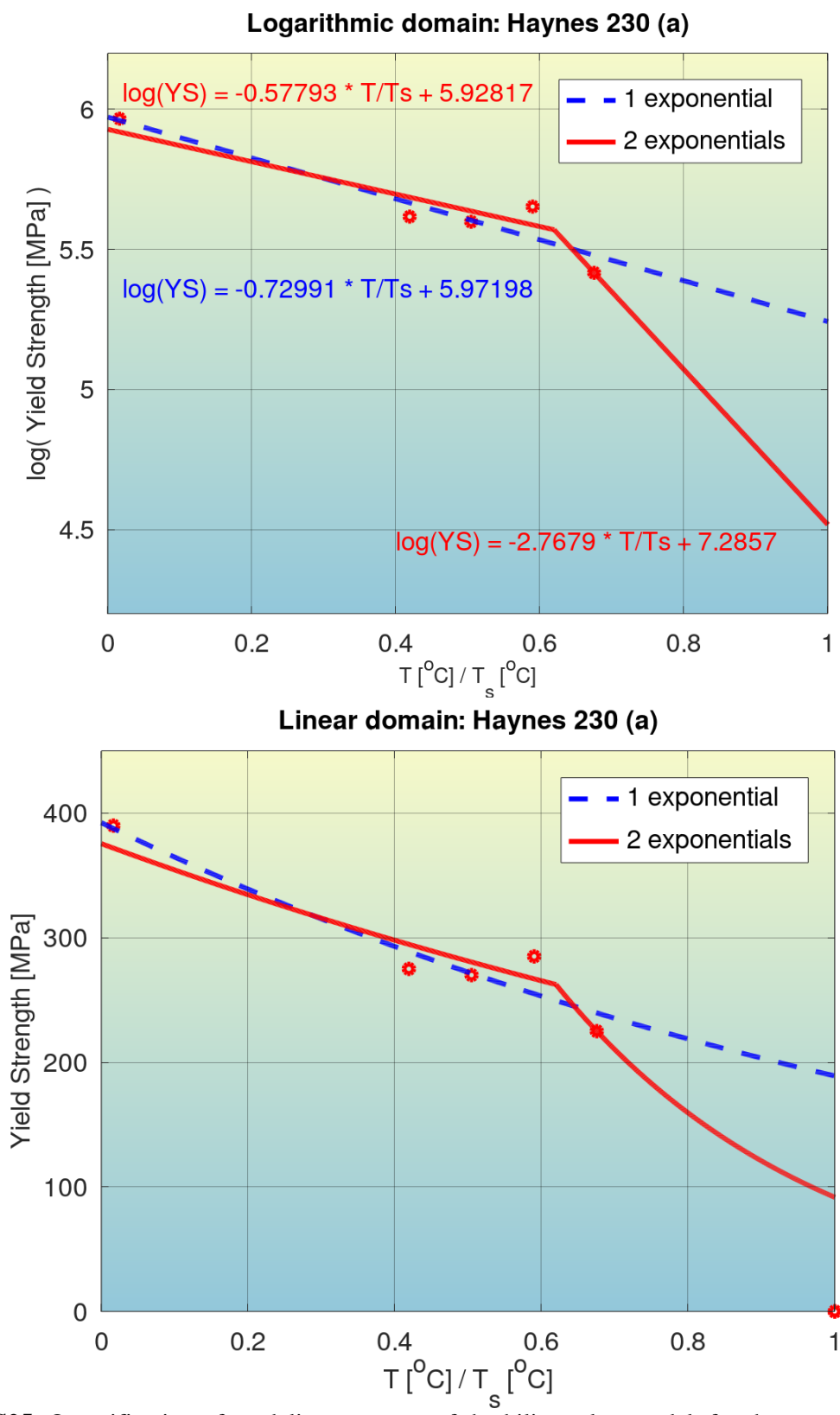


Figure S25: Quantification of modeling accuracy of the bilinear log model, for the composition No. 21 from Table S1 (Haynes 230 a), and comparison to that of a model with a single exponential. One outlier has been excluded from the modeling.

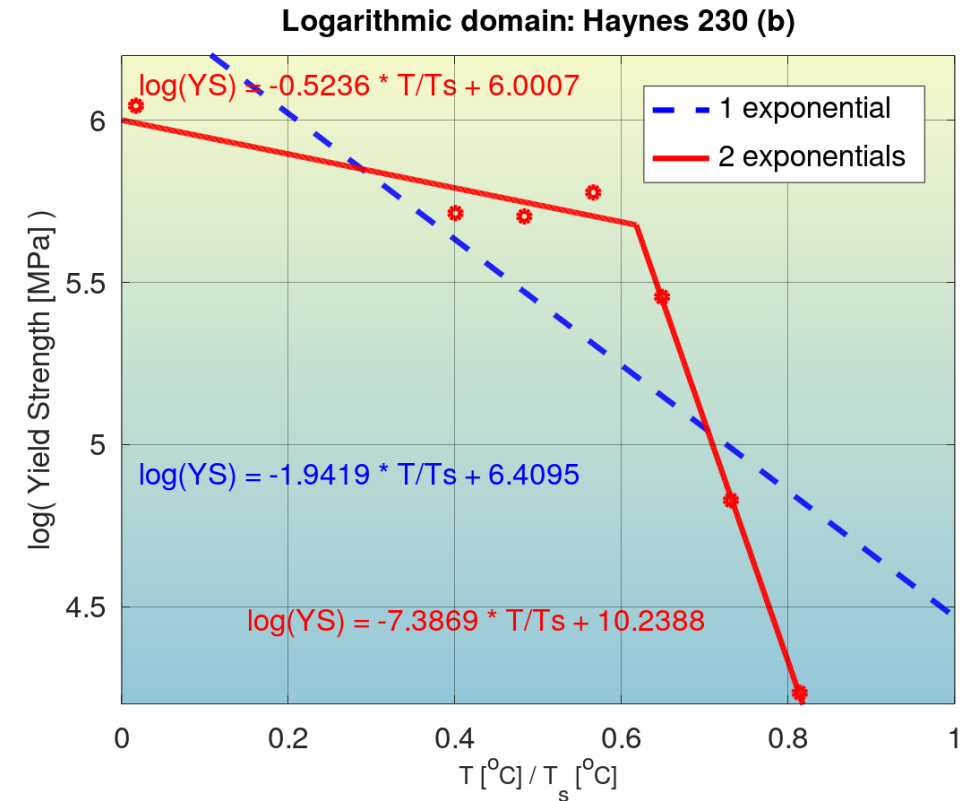


Figure S26: Quantification of modeling accuracy of the bilinear log model, for the composition No. 22 from Table S1 (Haynes 230 b), and comparison to that of a model with a single exponential. One outlier has been excluded from the modeling.

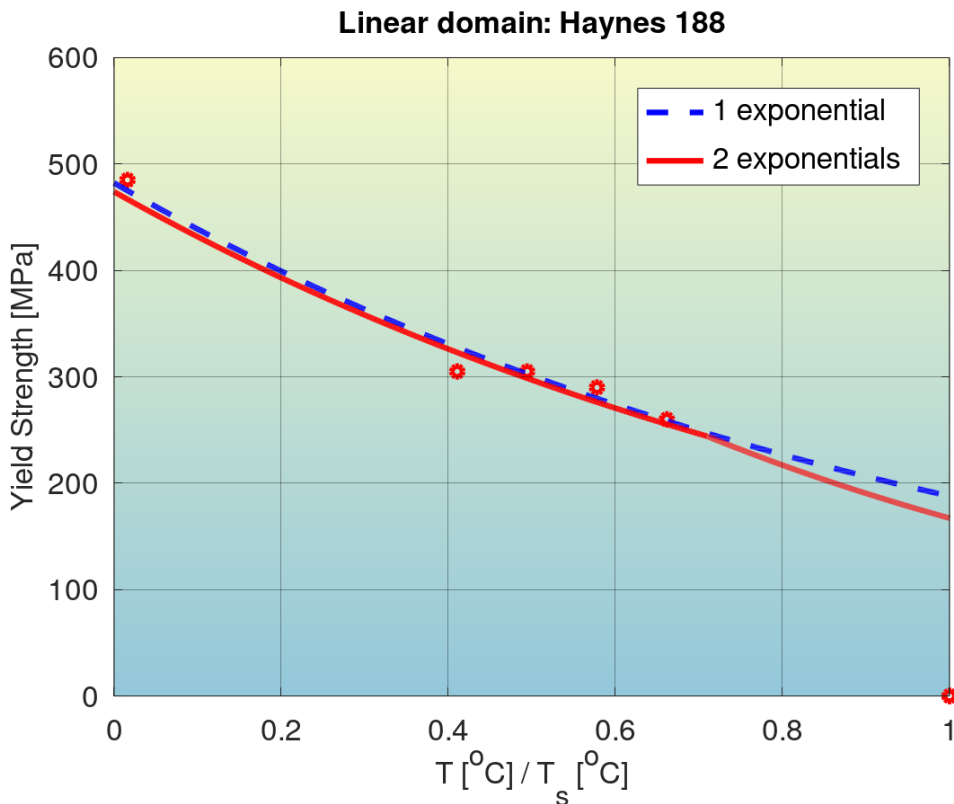
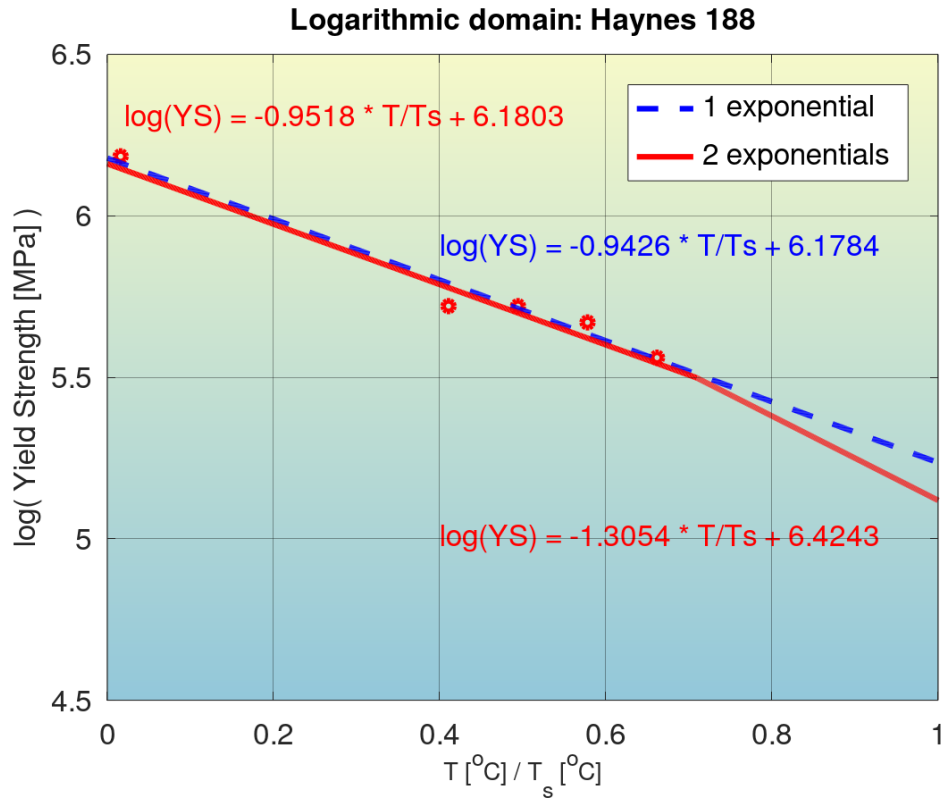


Figure S27: Quantification of modeling accuracy of the bilinear log model, for the composition No. 23 from Table S1 (Haynes 188), and comparison to that of a model with a single exponential. One outlier has been excluded from the modeling.

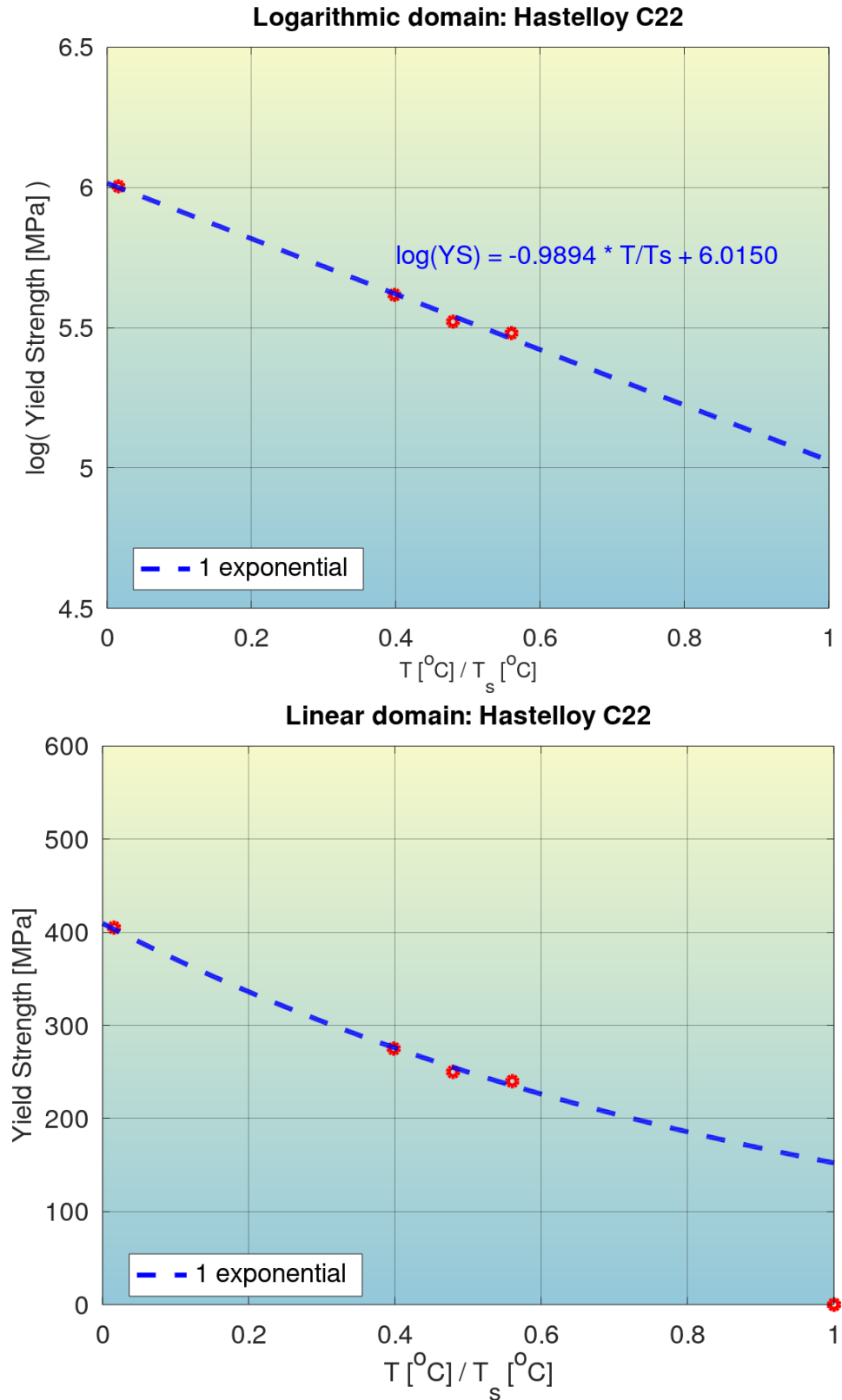


Figure S28: Quantification of modeling accuracy of the bilinear log model, for the composition No. 24 from Table S1 (Hastelloy C22), and comparison to that of a model with a single exponential. One outlier has been excluded from the modeling.

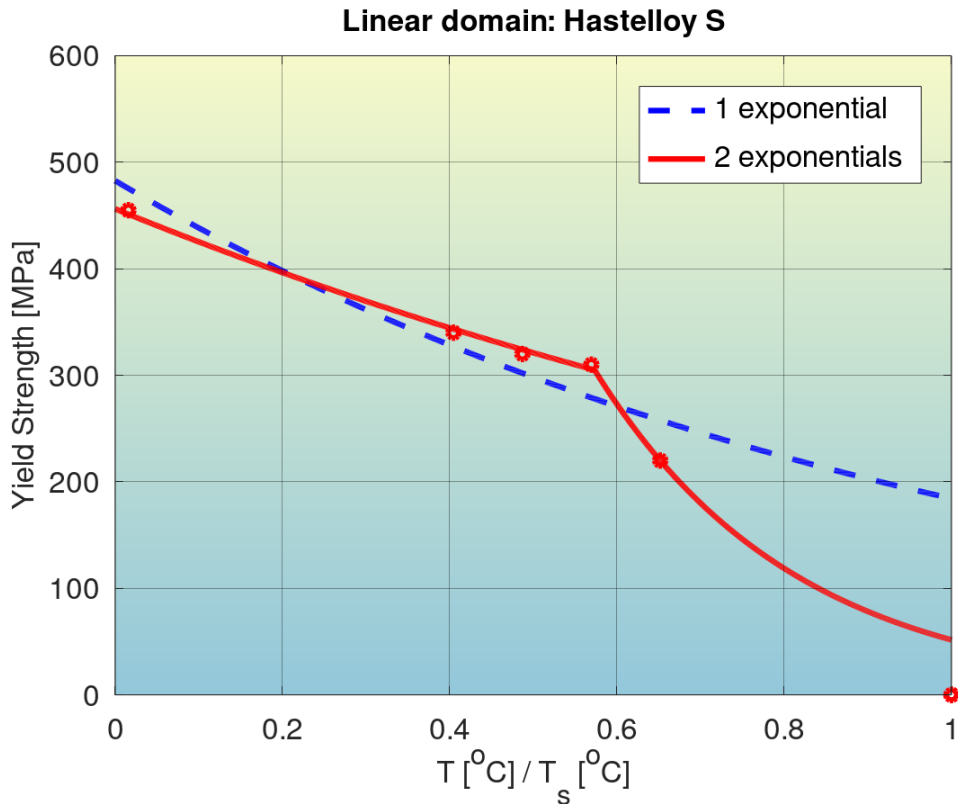
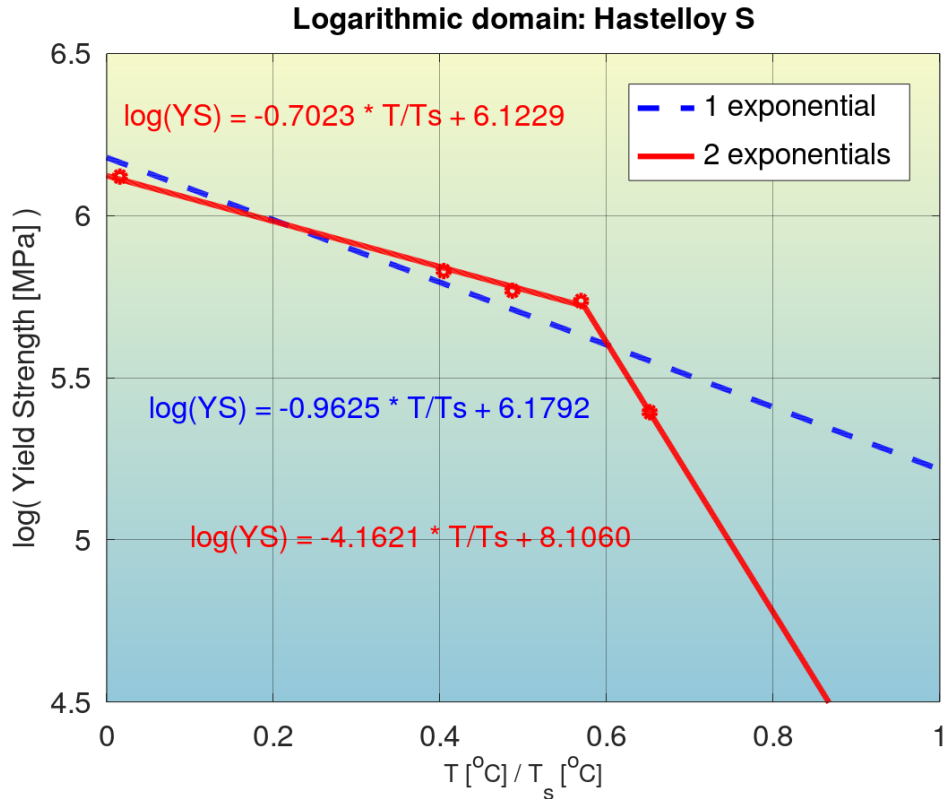


Figure S29: Quantification of modeling accuracy of the bilinear log model, for the composition No. 25 from Table S1 (Hastelloy S), and comparison to that of a model with a single exponential. One outlier has been excluded from the modeling.

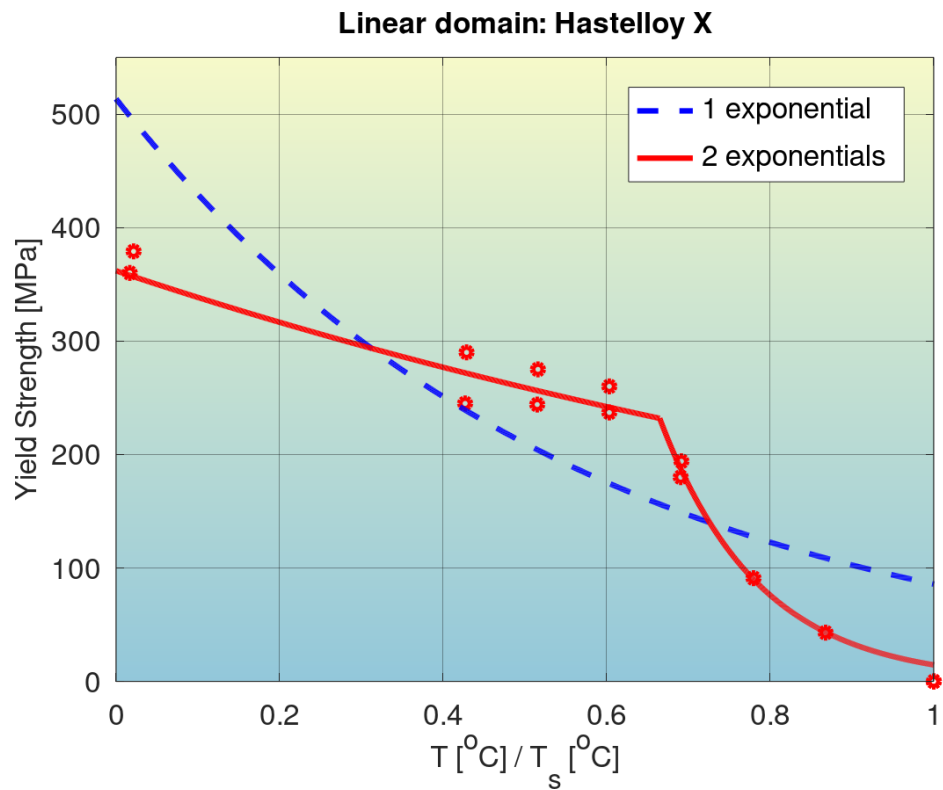
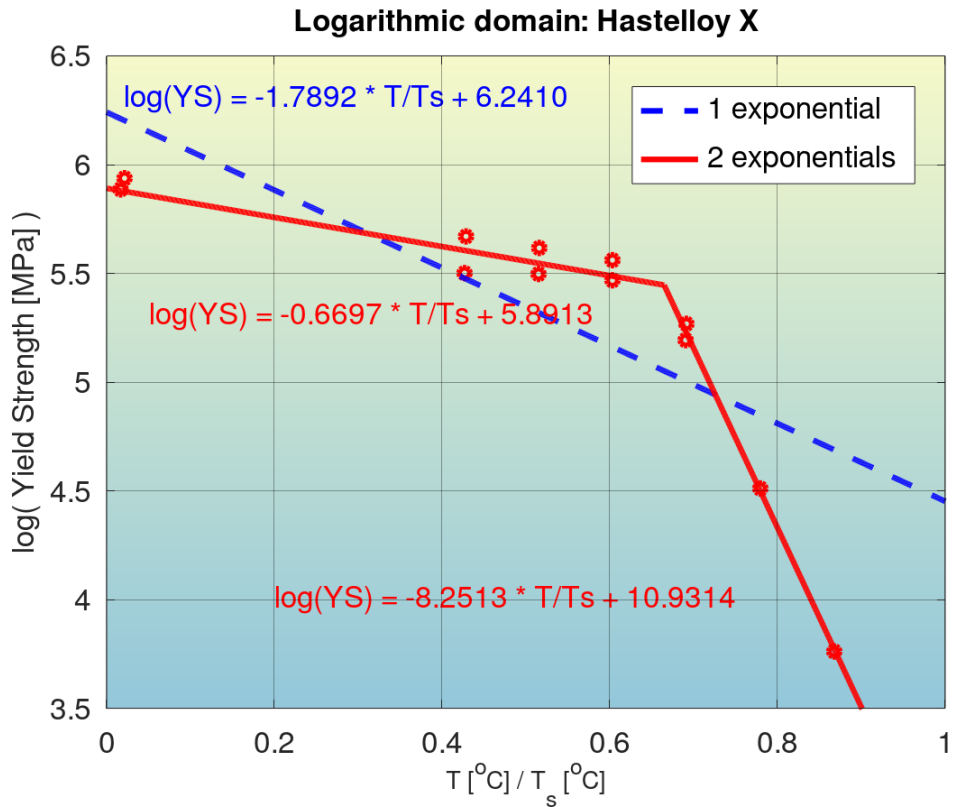


Figure S30: Quantification of modeling accuracy of the bilinear log model, for the composition No. 26 from Table S1 (Hastelloy X), and comparison to that of a model with a single exponential. One outlier has been excluded from the modeling.

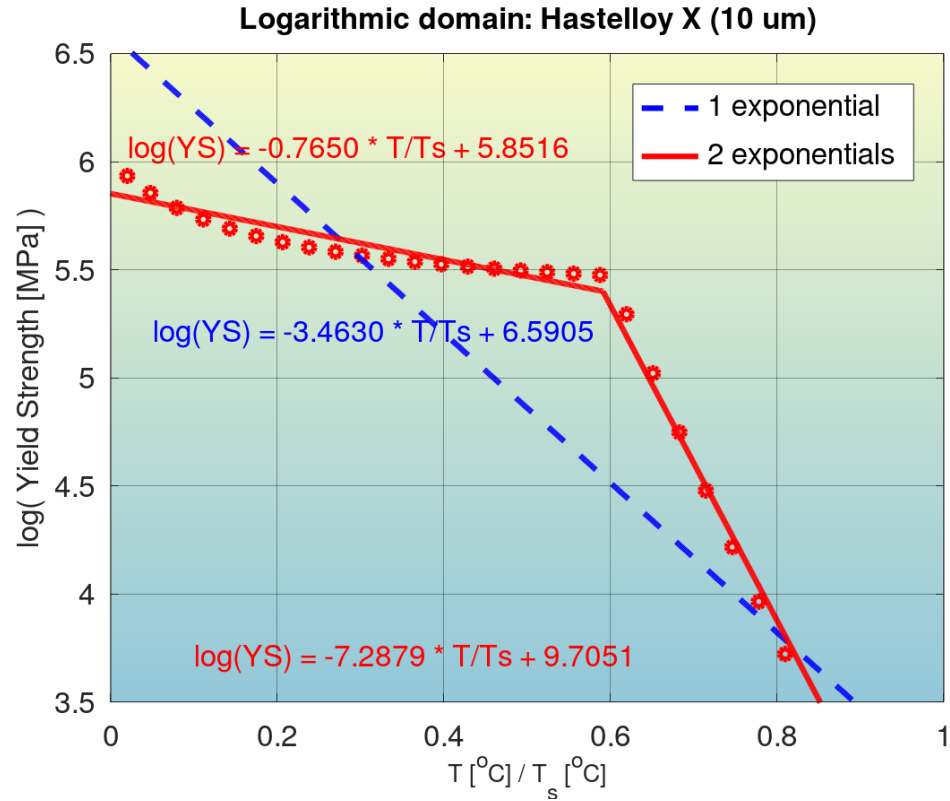


Figure S31: Quantification of modeling accuracy of the bilinear log model, for the composition No. 27 from Table S1 (Hastelloy X 10 μm), and comparison to that of a model with a single exponential. One outlier has been excluded from the modeling.

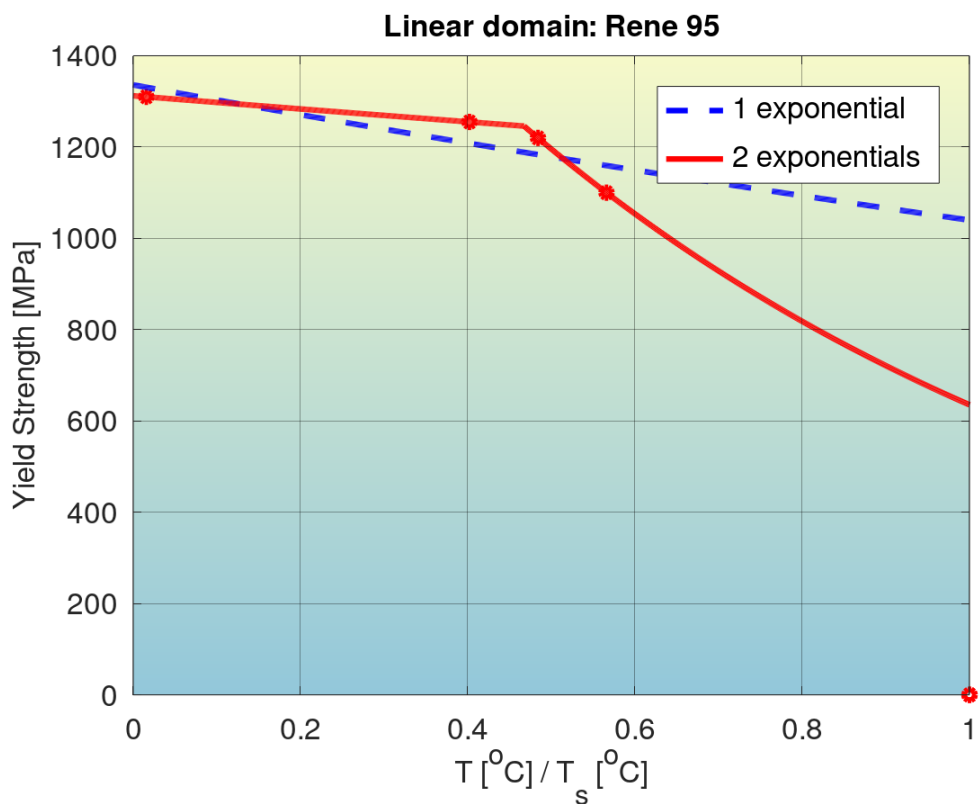
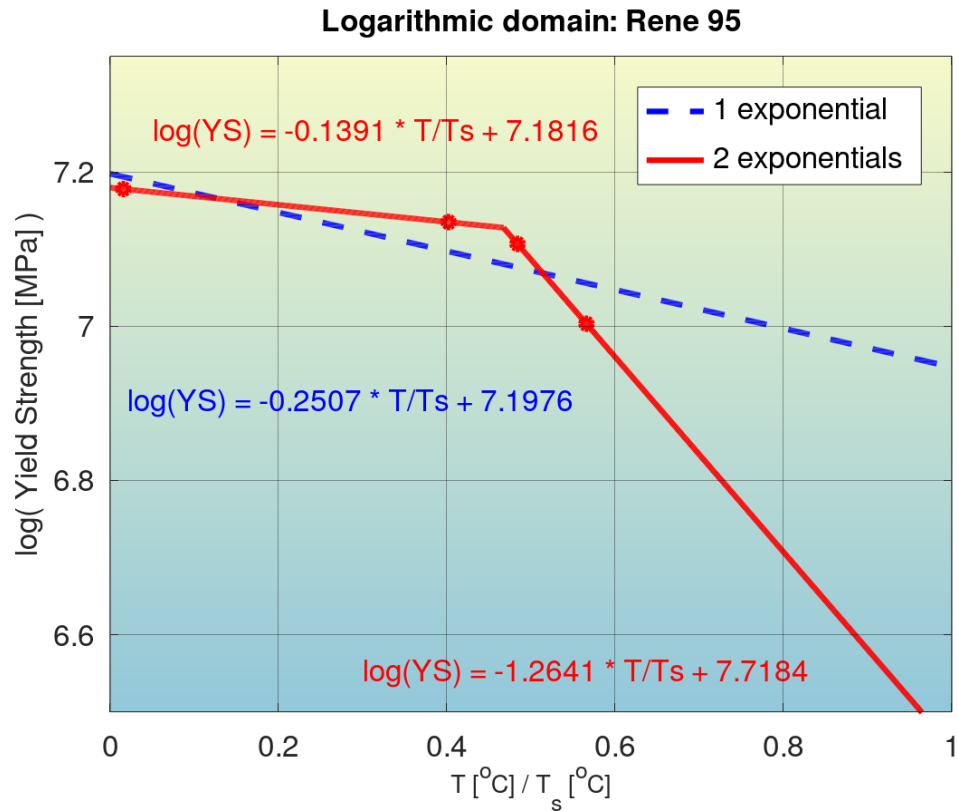


Figure S32: Quantification of modeling accuracy of the bilinear log model, for the composition No. 28 from Table S1 (Rene 95), and comparison to that of a model with a single exponential. One outlier has been excluded from the modeling.

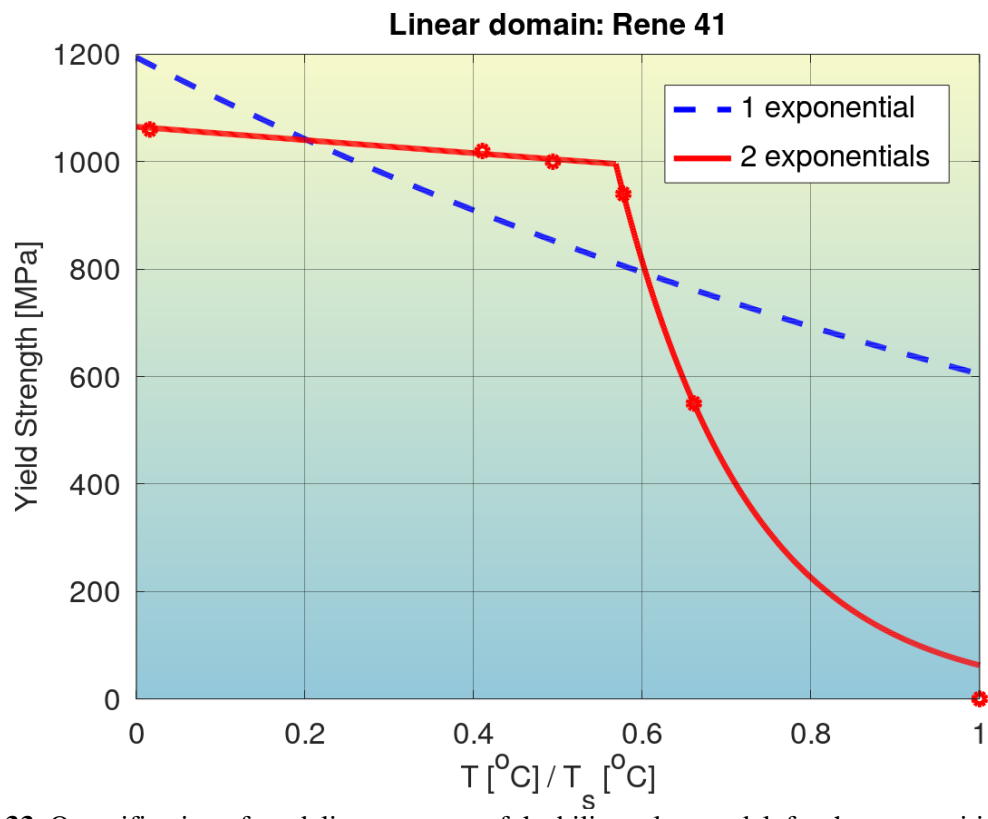
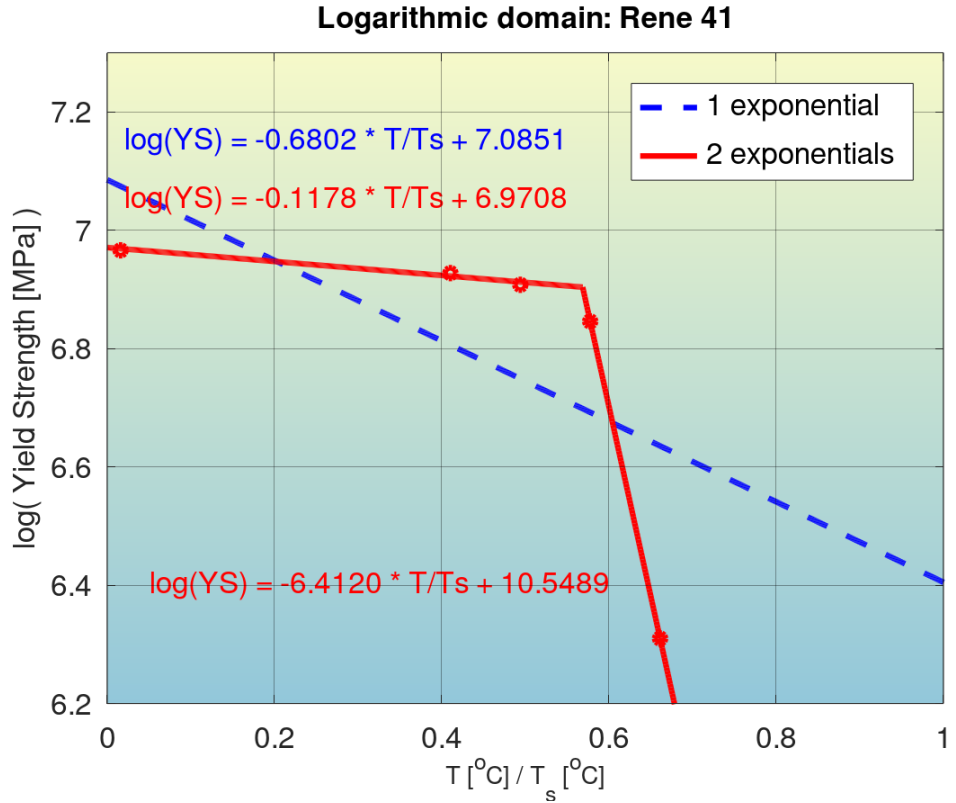


Figure 33: Quantification of modeling accuracy of the bilinear log model, for the composition No. 29 from Table S1 (Rene 41), and comparison to that of a model with a single exponential. One outlier has been excluded from the modeling.

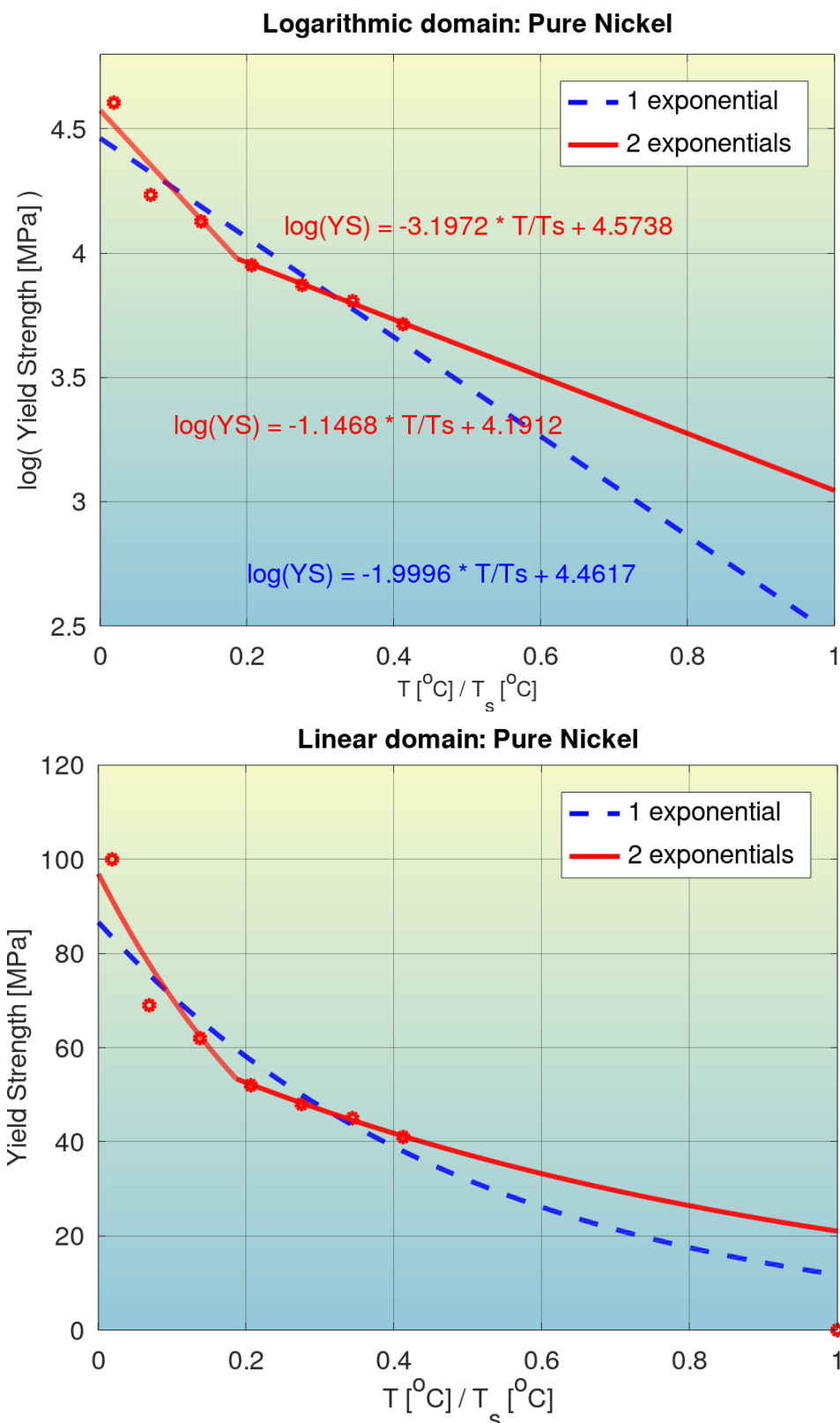


Figure 34: Quantification of modeling accuracy of the bilinear log model, for the composition No. 30 from Table S1 (Pure Nickel), and comparison to that of a model with a single exponential. One outlier has been excluded from the modeling.

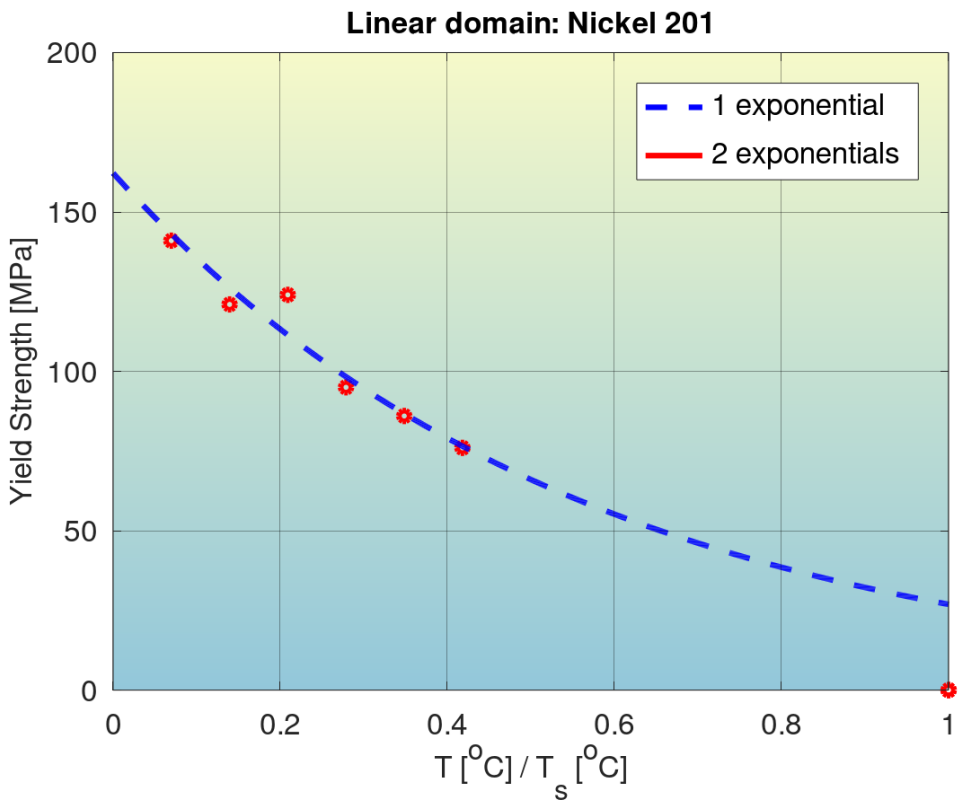
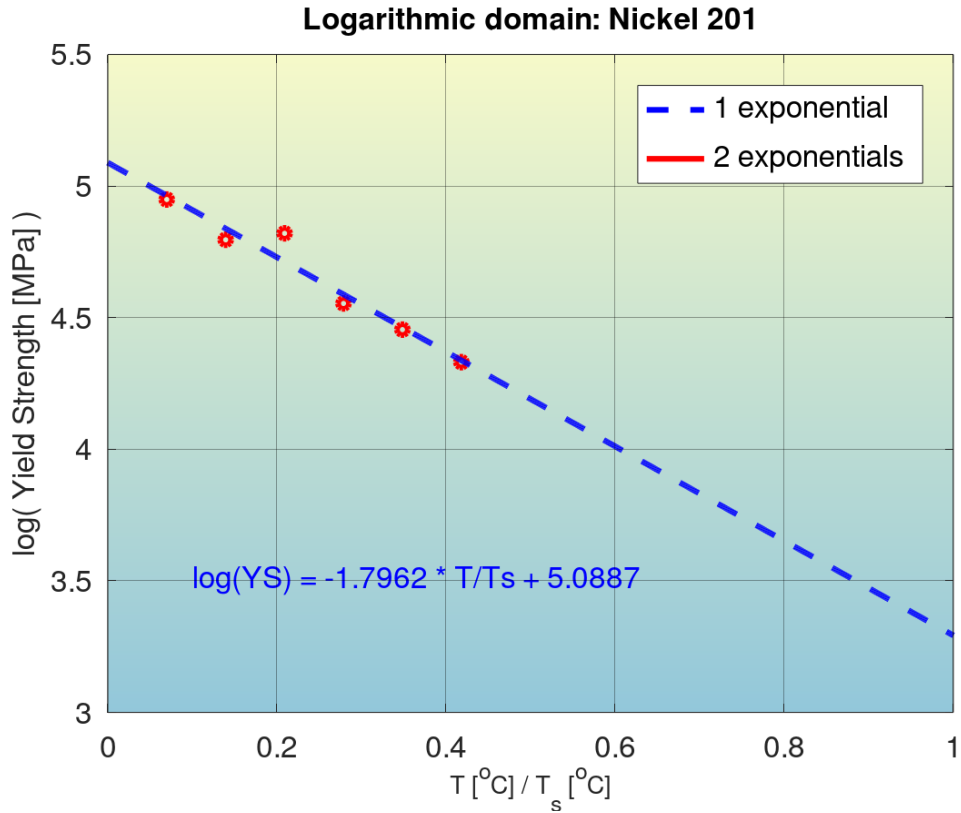


Figure 35: Quantification of modeling accuracy of the bilinear log model, for the composition No. 31 from Table S1 (Nickel 201), and comparison to that of a model with a single exponential. One outlier has been excluded from the modeling.

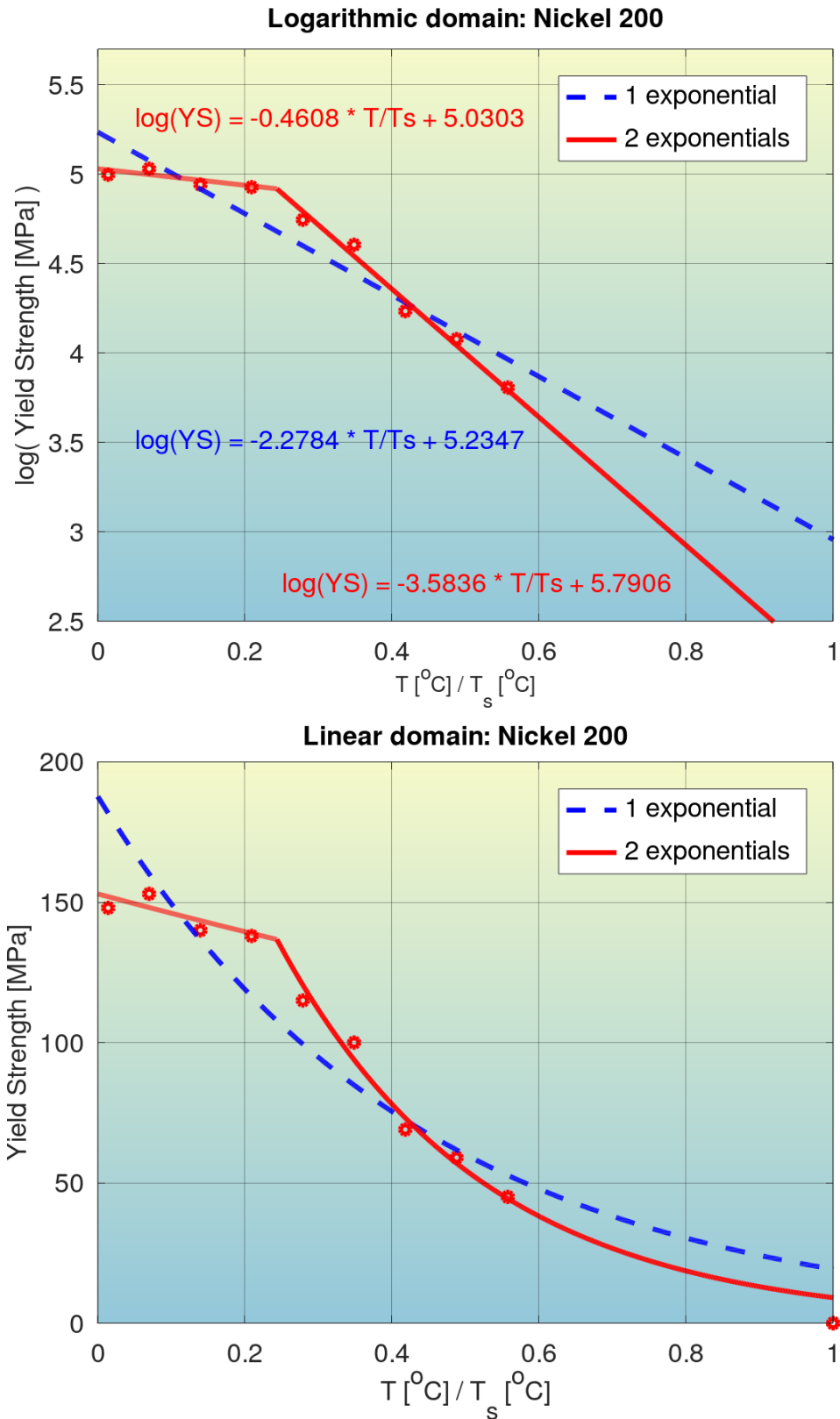


Figure 36: Quantification of modeling accuracy of the bilinear log model, for the composition No. 32 from Table S1 (Nickel 200), and comparison to that of a model with a single exponential. One outlier has been excluded from the modeling.

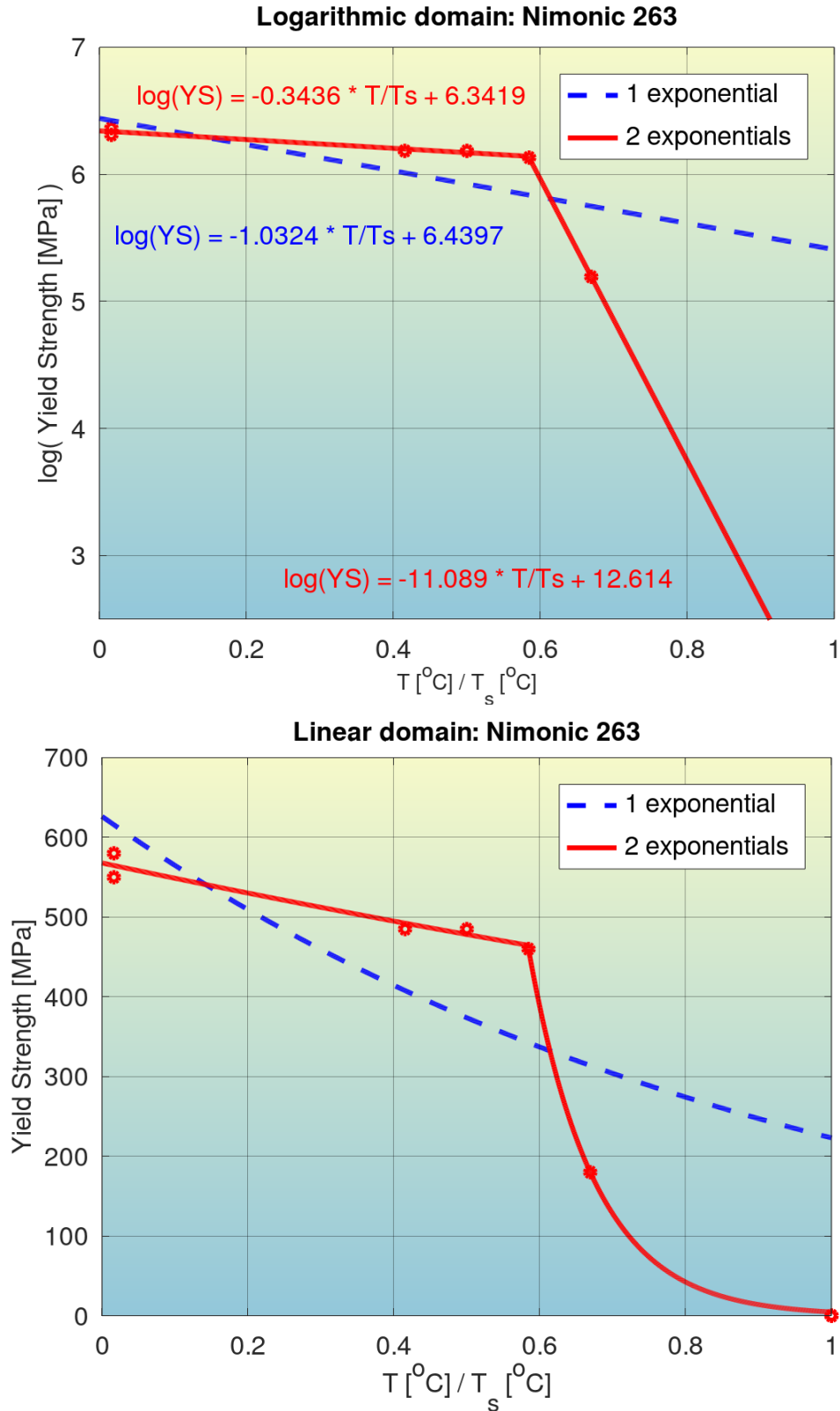


Figure 37: Quantification of modeling accuracy of the bilinear log model, for the composition No. 33 from Table S1 (Nimonic 263), and comparison to that of a model with a single exponential. One outlier has been excluded from the modeling.

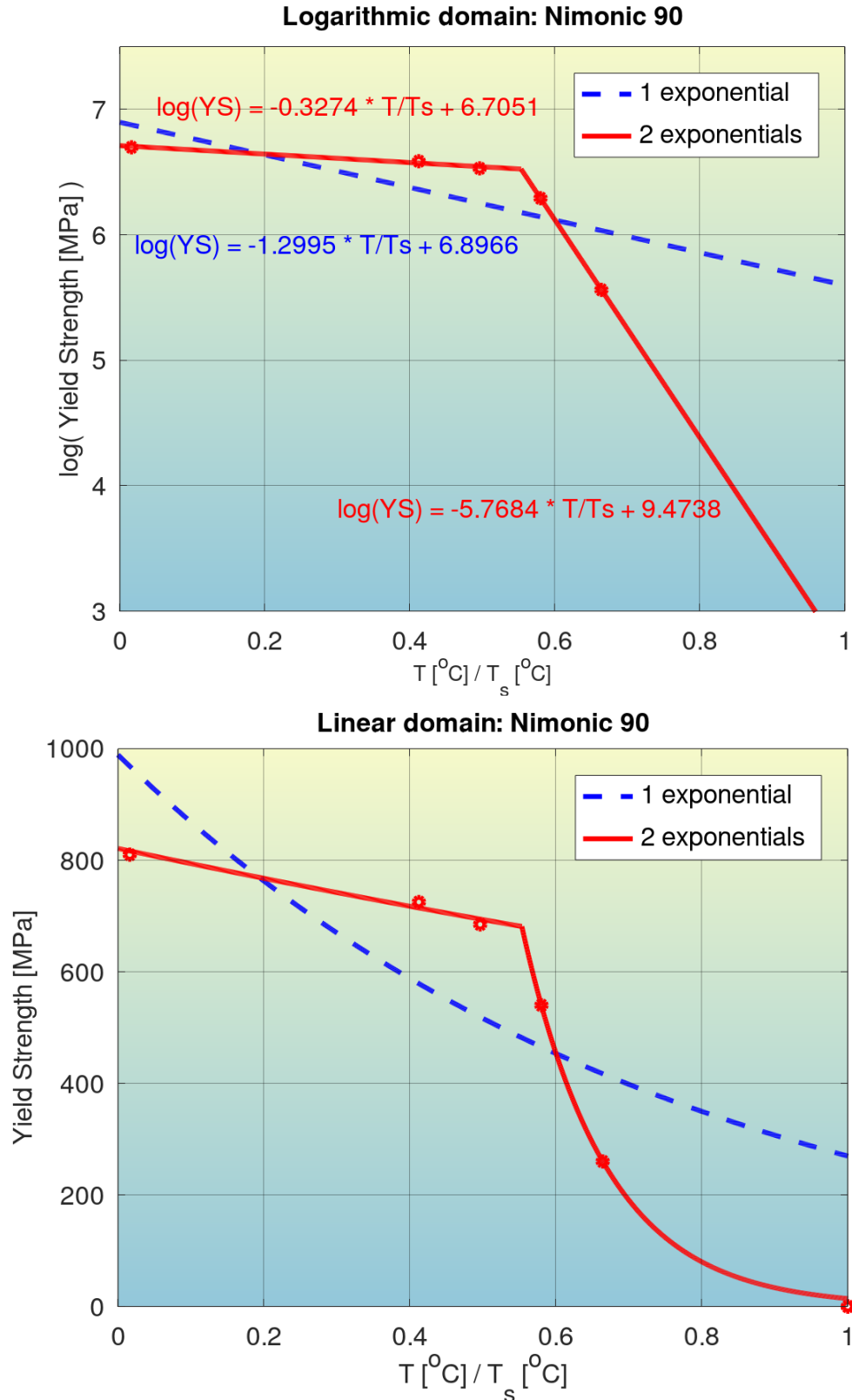


Figure 38: Quantification of modeling accuracy of the bilinear log model, for the composition No. 34 from Table S1 (Nimonic 90), and comparison to that of a model with a single exponential. One outlier has been excluded from the modeling.

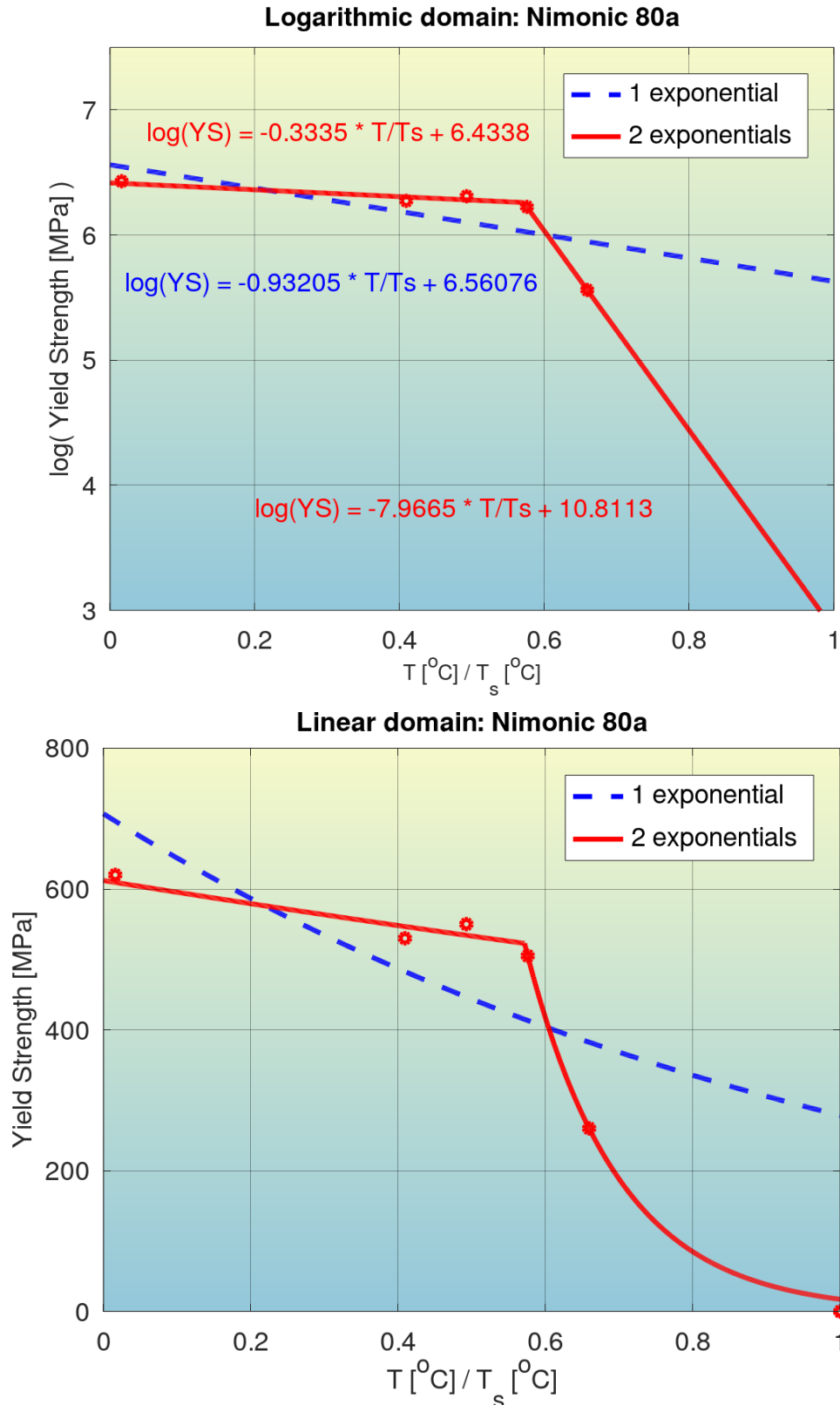


Figure 39: Quantification of modeling accuracy of the bilinear log model, for the composition No. 35 from Table S1 (Nimonic 80a), and comparison to that of a model with a single exponential. One outlier has been excluded from the modeling.

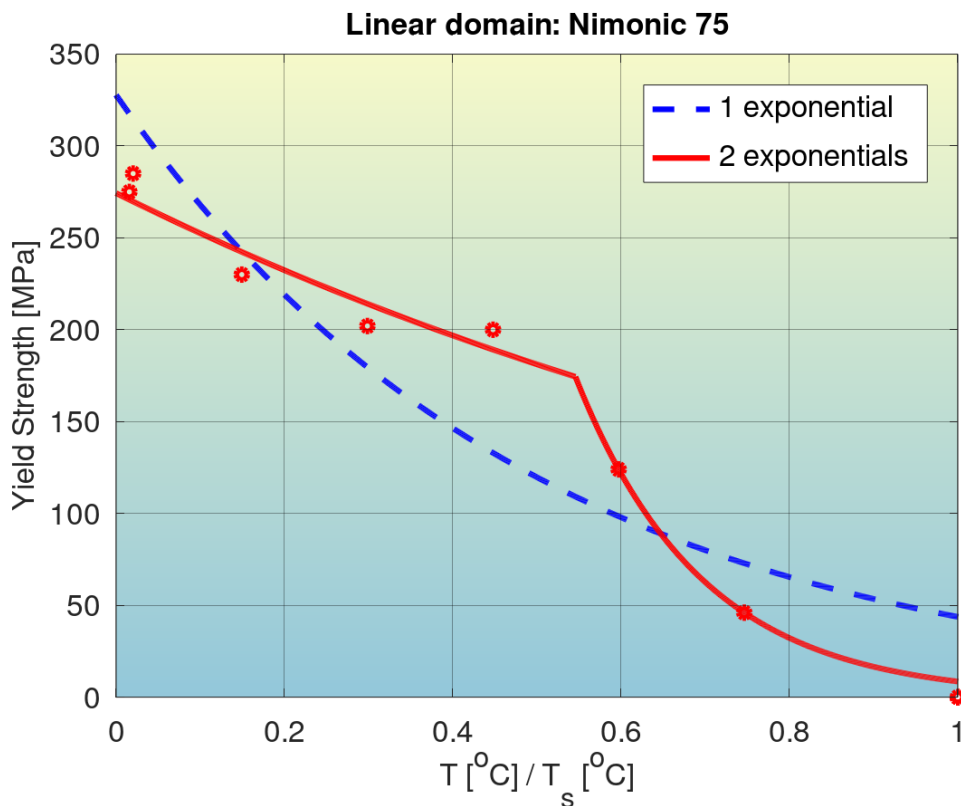
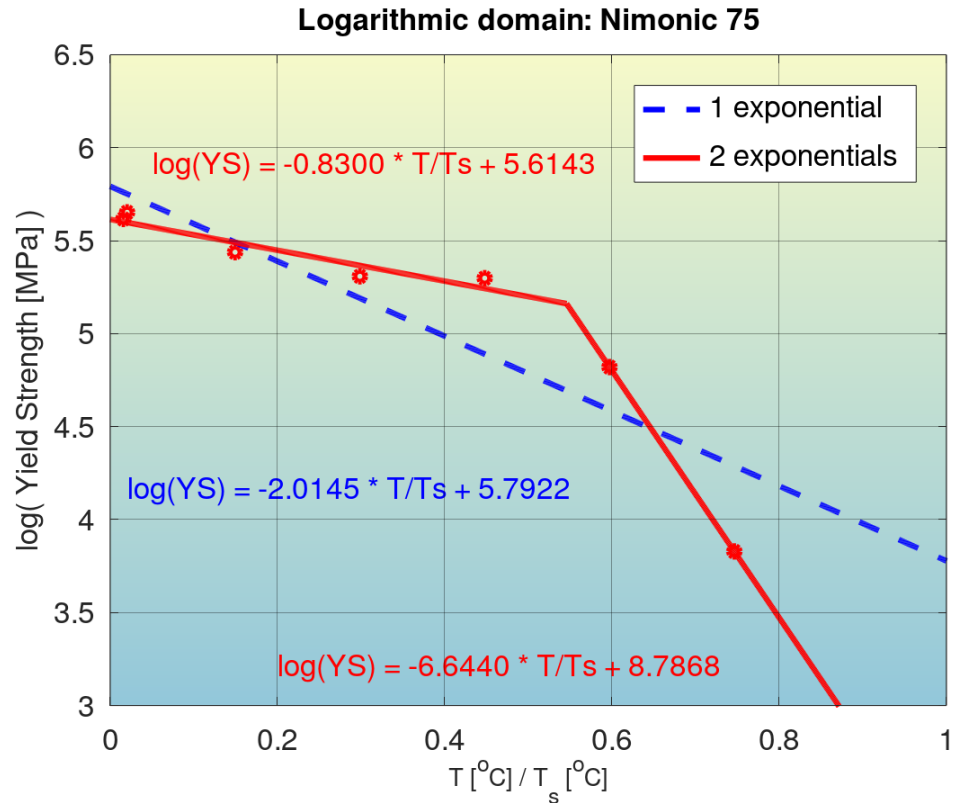


Figure 40: Quantification of modeling accuracy of the bilinear log model, for the composition No. 36 from Table S1 (Nimonic 75), and comparison to that of a model with a single exponential. One outlier has been excluded from the modeling.

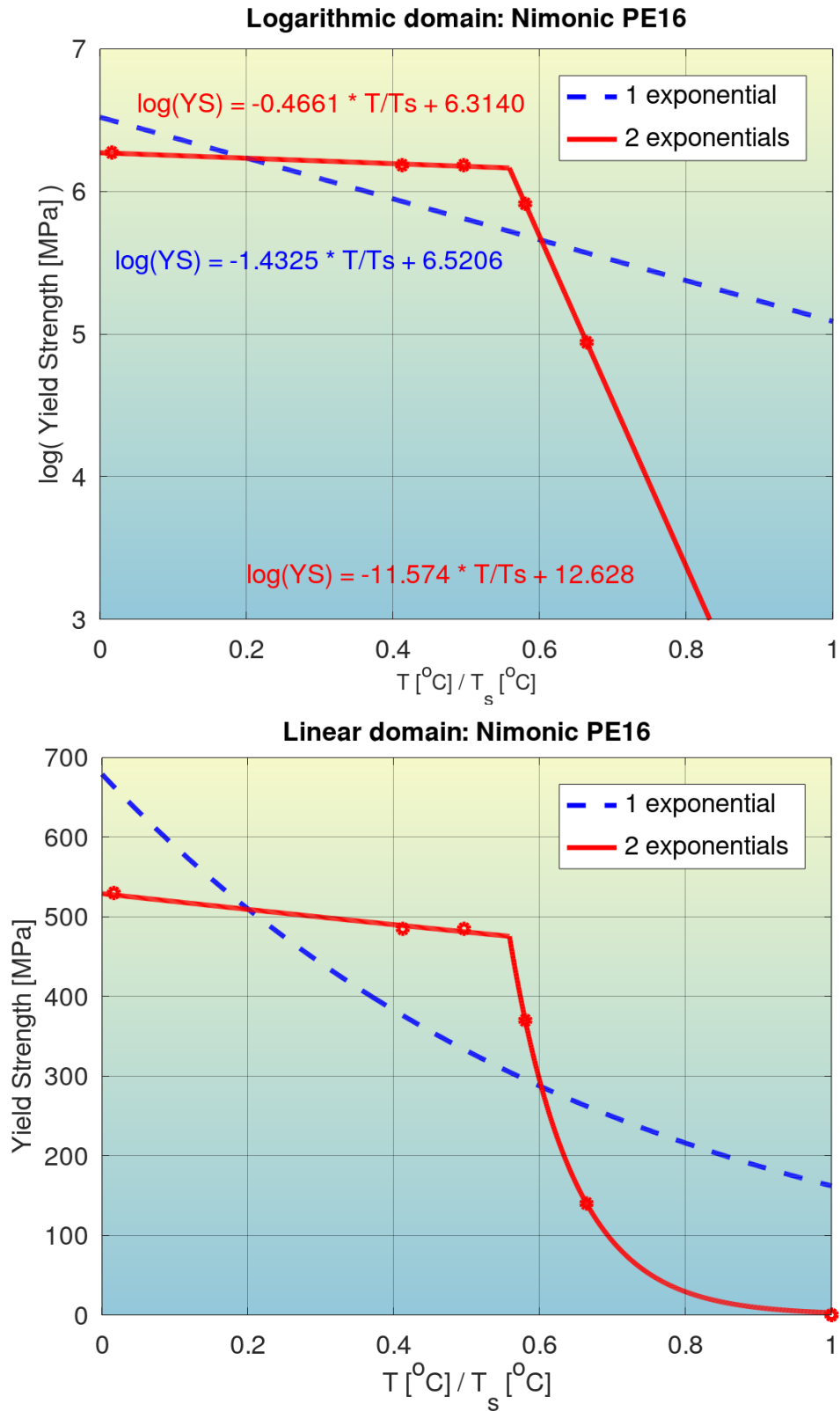


Figure 41: Quantification of modeling accuracy of the bilinear log model, for the composition No. 37 from Table S1 (Nimonic PE16), and comparison to that of a model with a single exponential. One outlier has been excluded from the modeling.

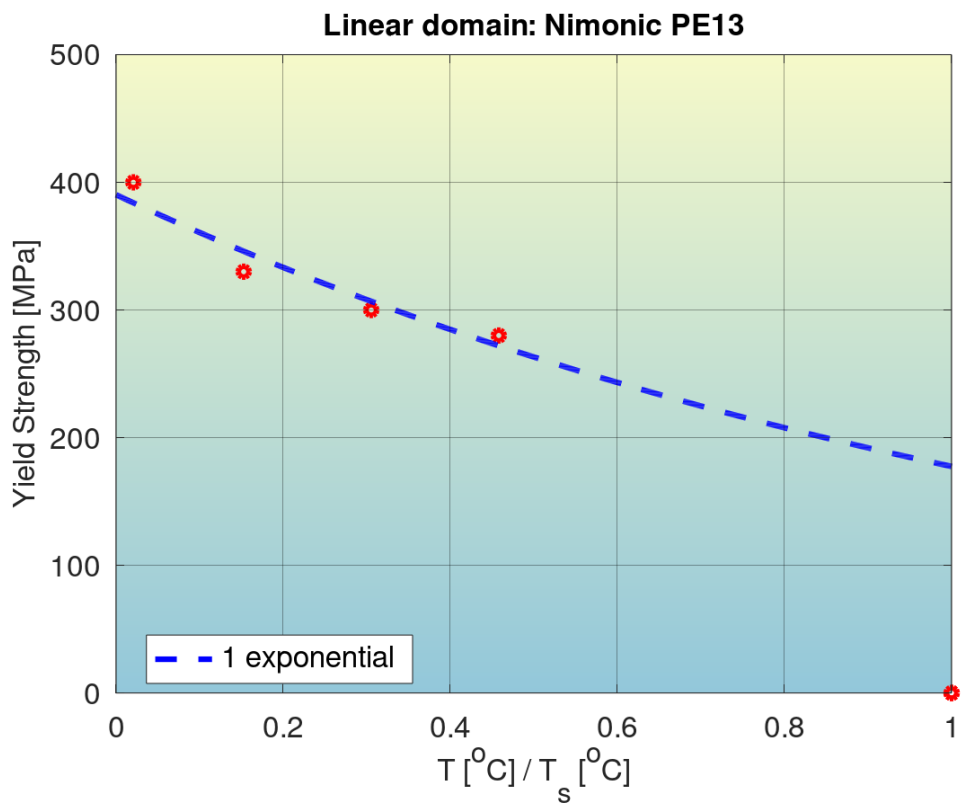
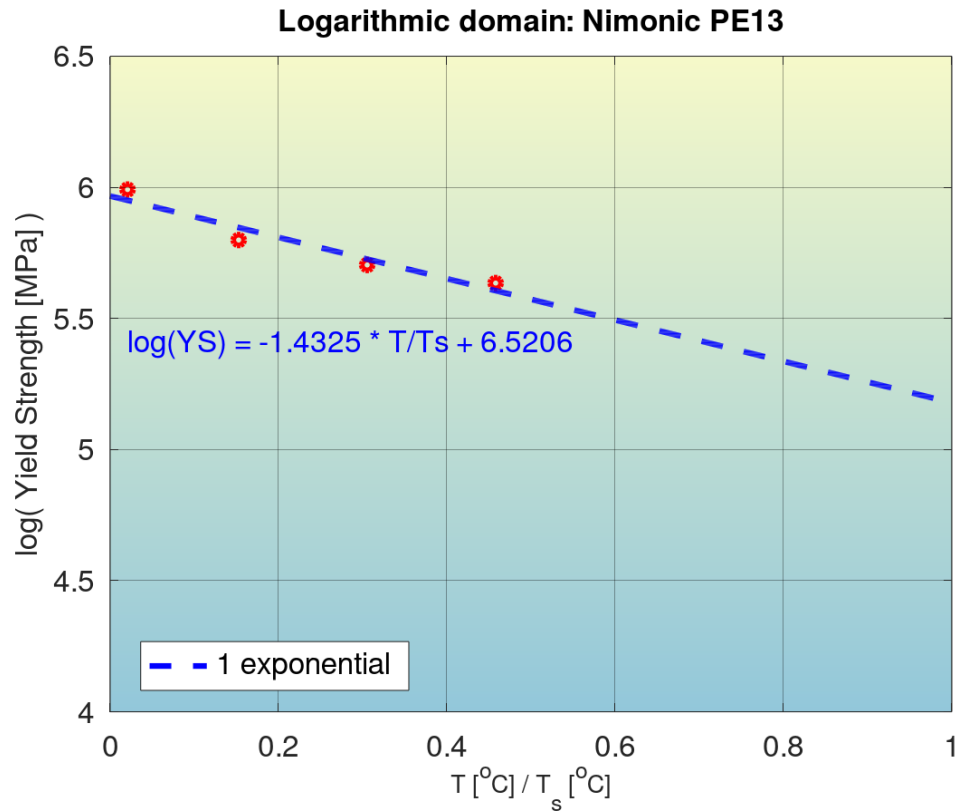


Figure 42: Quantification of modeling accuracy of the bilinear log model, for the composition No. 38 from Table S1 (Nimonic PE13), and comparison to that of a model with a single exponential. One outlier has been excluded from the modeling.

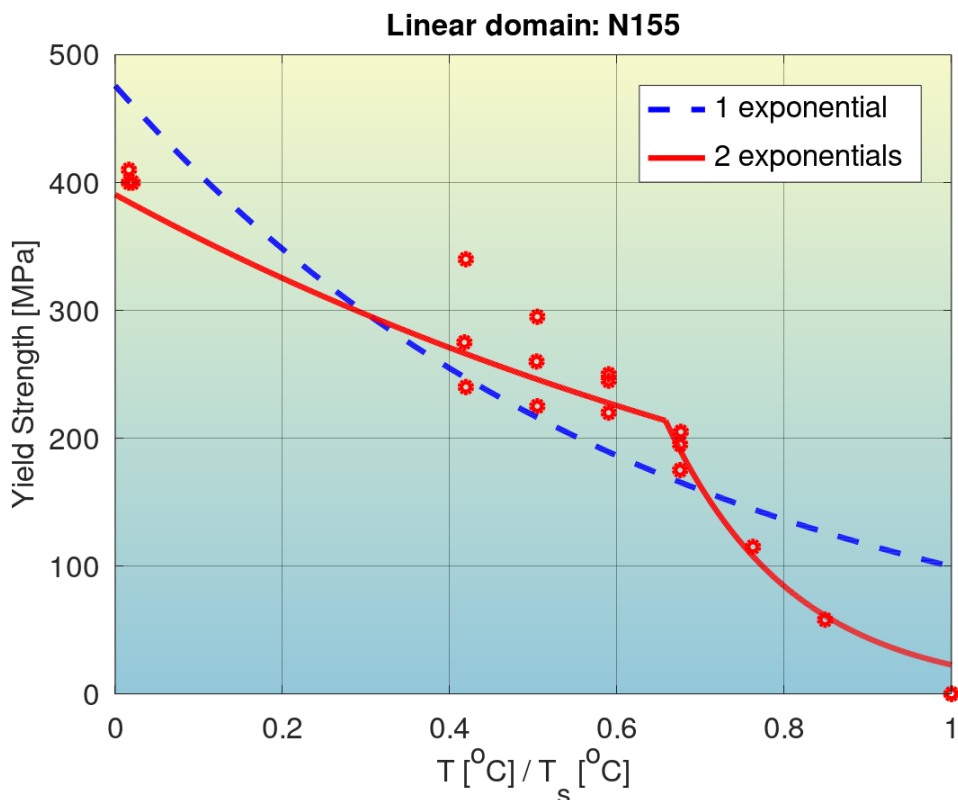
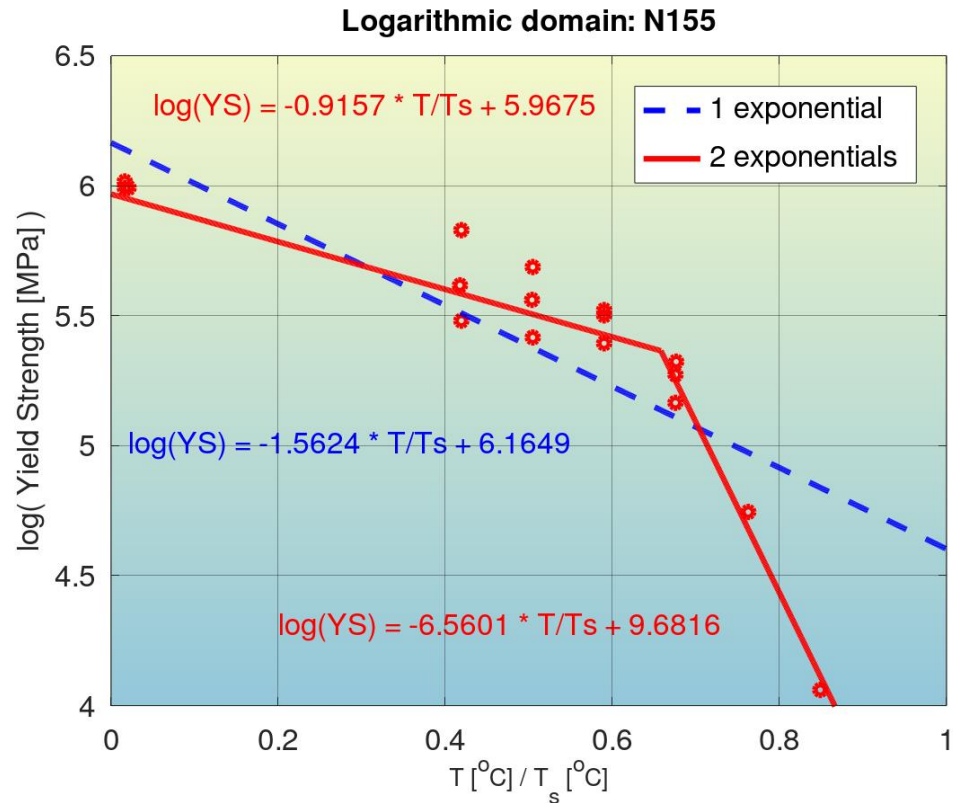


Figure 43: Quantification of modeling accuracy of the bilinear log model, for the composition No. 39 from Table S1 (N155), and comparison to that of a model with a single exponential. One outlier has been excluded from the modeling.

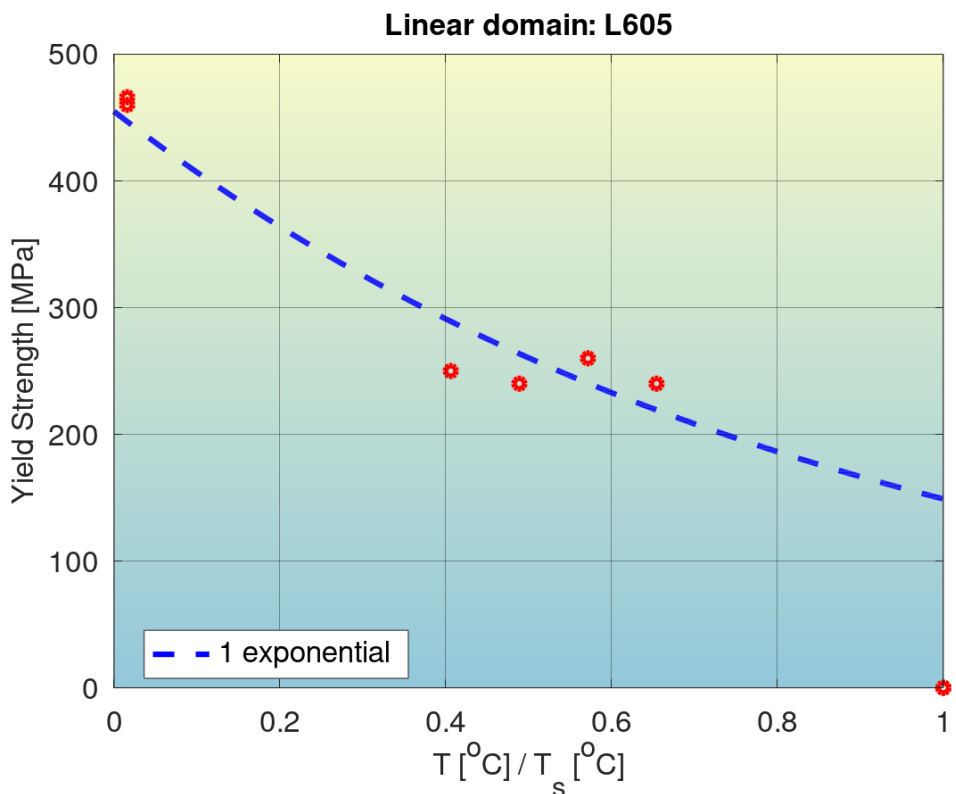
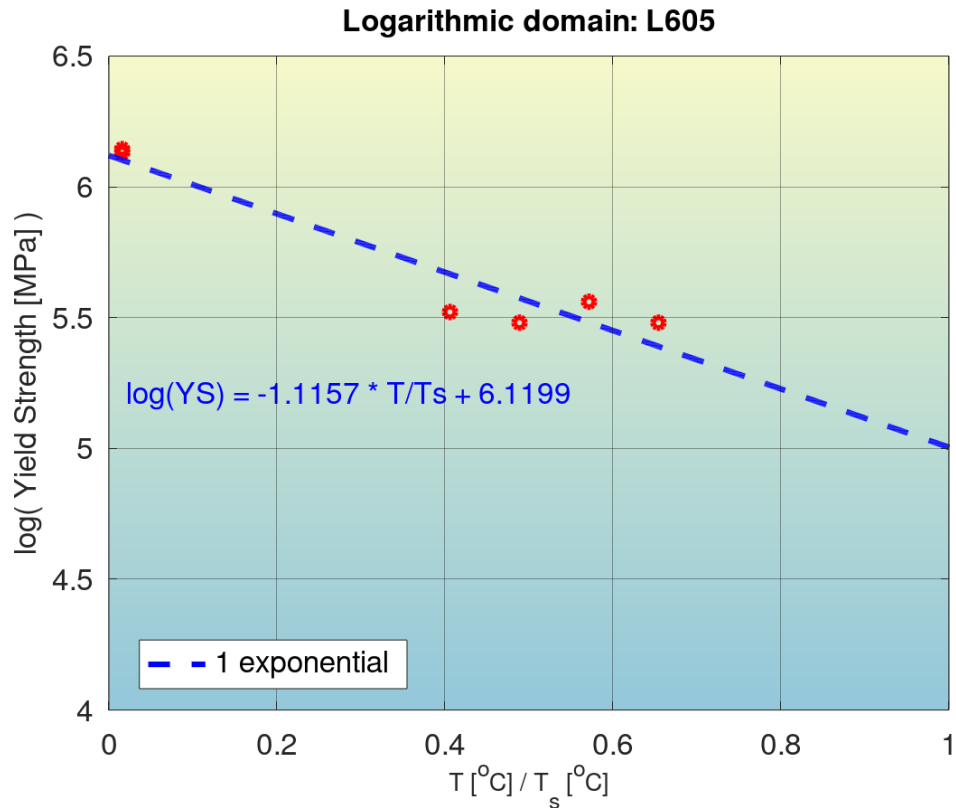


Figure 44: Quantification of modeling accuracy of the bilinear log model, for the composition No. 40 from Table S1 (L605), and comparison to that of a model with a single exponential. One outlier has been excluded from the modeling.

Supplementary Notes

1. *High-Level Classification of Alloy Materials for High-Temperature Applications*

Figure S1 offers a classification of alloy materials for fossil-energy power plants [40]. Ferrite, or α -Fe, refers to a specific body-centered-cubic (BCC) crystal structure of iron, which is observed below 912 °C (1,674 °F). Along with ferritic, martensitic, duplex and precipitation-hardened stainless steels, austenitic stainless steel is one of the five classes of stainless steels by a crystal structure. The primary crystalline structure of an austenitic stainless steel is the austenite phase [face-centered-cubic (FCC) γ -phase of iron (γ -Fe)], which prevents the steels from being hardenable by the heat treatment, and also makes them essentially non-magnetic. For a general overview of the Ni-base superalloys, refer to the Supplementary Note 2 below. As seen in Figure S1, the Ni-base superalloys Inconel 740, Haynes 230, and Inconel 617 offer superior mechanical properties at elevated temperatures, i.e., the maximum allowable stress, as compared to other engineering alloys [40].

2. *Brief Overview of Nickel-Based Superalloys*

For sample phase diagrams for Nickel-based superalloys, refer to [45].

1. The Gamma Phase (γ)

Most commercial Ni-based superalloys contain the following elements: C, Cr, Mo, W, Ni, Nb, Fe, Ti, Al, V, and Ta. The γ phase comprises the continuous matrix of the superalloy. The γ matrix is a solid-solution disordered FCC austenitic phase of the alloying elements, one that usually contains a high percentage of solid-solution elements (e.g., Co, Cr, Mo, and W). Ref. [46] provides a good overview of the metallurgy of superalloys, including the crystal structures and phases.

2. The Gamma Prime Phase (γ')

The γ' phase is an intermetallic precipitate and the principal strengthening phase in many Ni- and NiFe-based superalloys [46]. The intermetallic γ' phase consists of $\text{Ni}_3\text{AlNi}_3(\text{Al,Ti})$ with an ordered FCC $L1_2$ crystal structure [46].

3. The Gamma Double Prime Phase (γ'')

The γ'' is the principal strengthening phase in Inconel 718 [46]. The γ'' phase normally consists of the Ni_3Nb or Ni_3V and is typically used to strengthen Ni-based superalloys at lower temperatures (below 650 °C) relative to the γ' phase. The crystal structure of the γ'' phase is ordered $D0_{22}$ body-centered tetragonal (BCT). The γ'' phase precipitates as 60 nm by 10-nm-anisotropic discs whose (001) plane aligns parallel to the {001} family for the γ phase. Formation of these anisotropic phases is caused by the lattice mismatch between the BCT precipitates and the FCC austenitic γ matrix phase. Such a lattice mismatch gives rise to high coherency strains, which contribute to the primary strengthening mechanisms [47].

4. The Eta Phase (η)

Between the temperatures of 600 °C and 850 °C, the γ' phase can transform into the HCP ($D0_{24}$) η phase. The η phase consists of Ni_3Ti (no solubility for other elements) and is found after the extended exposure in some FeNi-, Co-, and Ni-based superalloys with high Ti/Al ratios [46].

5. The Carbide Phases

Formation of secondary carbide phases, such as the cubic MC phase, the FCC M_{23}C_6 phase, the FCC M_6C phase, or the hexagonal M_7C_3 phase, is common in Ni-based superalloys. Carbides present at grain boundaries have been used effectively to inhibit grain growth and grain-boundary sliding at elevated temperatures [48]. However, care must be taken to prevent continuous films along grain boundaries, which can cause the precipitate-free zone phenomenon near the boundaries, and increase notch sensitivity and intergranular cracking [46].

6. The Topologically-Closed-Packaged (TCP) Phases

The TCP phases refer to a family of phases, including the σ phase, the χ phase, the μ phase, and the Laves phase [46], which are not atomically close-packed. Instead, the TCP phases show closed-packed planes with an HCP stacking sequence. The TCP phases tend to be highly brittle and deplete

the γ matrix of solute atoms, needed for the formation of strengthening intermetallics. The TCP phases tend to form as a result of kinetics after long exposure (thousands of hours) at elevated temperatures ($> 750\text{ }^{\circ}\text{C}$) [47].

3. *Brief Overview of Cobalt-Based Superalloys*

As noted in [46], Co-based superalloys are usually strengthened by a combination of carbides and solid-solution hardeners.

1. The Gamma Phase (γ)

Analogous to the Ni-based superalloys, the γ phase comprises the continuous matrix of the superalloy. Developmental (i.e., non-commercial) superalloys contain the following elements: C, Cr, W, Ni, Ti, Al, Ir, and Ta [49], [50].

2. The Gamma Prime Phase (γ')

Similar to the Ni-based superalloys, the γ' phase constitutes the precipitate used to strengthen the Co-based superalloys [49], [51].

3. The Carbide Phases

As prevalent with the carbide formation, the appearance of carbide phases in Co-based superalloys does provide precipitation hardening, but decreases low-temperature ductility [50].

4. The Topologically Closed-Packaged Phases

The TCP phases may appear in some developmental Co-based superalloys. But the goal is to avoid such phases.

4. *Brief Overview of Iron-Based Superalloys*

Use of steels for applications necessitating superalloys may be of interest, because certain steels have exhibited creep and oxidation resistance analogous to that of Ni-based superalloys, while being much less expensive to manufacture.

1. The Gamma Phase (γ)

Similar to the Ni-based superalloys, the Fe-based superalloys feature a γ matrix phase of the austenite iron with an FCC microstructure [52].

2. The Gamma Prime Phase (γ')

As for the Ni- and Co-based superalloys, the γ' phase is introduced in the form of precipitates to strengthen the Fe-based superalloys.

5. *Qualitative Overview of Strengthening Mechanisms in Ni-Based Superalloys across Temperature*

Figure S2 and Figure S3 provide a qualitative overview of the strengthening mechanisms in Ni-based superalloys across temperature. At lower and medium temperature ranges, the superalloys benefit from precipitation strengthening (from γ' to γ''). With increasing the temperature, there is an earlier onset of precipitate coarsening and often times transformation into metastable phases, or formation of new ones. In turn, the effect of solid-solution strengthening can become more significant, as well as the presence of ideally homogeneously dispersed, fine carbides in the matrix and globular, larger ones along the grain boundaries.

6. *Towards Quantitative Overview of Strengthening Mechanisms in Superalloys across Temperature*

The total yield strength is the outcome of an interplay of the strengthening contributions from mainly the secondary phases and the solute atoms in the matrix. Generally, there is a linear relationship between the high-temperature strength and γ' volume fraction [53]. Commonly, the volume fraction varies between 25 – 60 %, with modern superalloys being on the upper end of this range. Besides the influence of the volume fraction, finer γ' precipitates may impart greater strength than coarser precipitates, at a constant volume fraction. However, as the temperature varies, different dislocation-interaction mechanisms may be activated, favoring larger precipitates, with higher lattice misfits.

The γ' -precipitation hardened superalloys exhibit unique positive temperature dependence with respect to the flow stress [54]. Between -200 °C and 800 °C, the flow stress tends to be reversible. This feature is related to the cross-slip of screw dislocations and the associated formation of Kear-Wiltsdorf locks on {100} planes [55], [56]. Similarly, lowering of the anti-phase boundary (APB) energy and thermally activated cross-slip on cube planes defines the location of the peak shown in Figure S4. The momentary flow stress and the peak location depend on the solute content (primarily the Al content, thus the volume fraction) [57].

7. *Further Specifics on the Superalloys Listed in the Supplementary Table S1*

2. Udimet D979: Here, there are no grain-boundary carbides of Type M₂₃C₆ or M₆C due to a low carbon content.
3. Udimet 720: We believe that the volume fraction, the average size of the primary precipitate, and the average size of the secondary/aged precipitate correspond to the standard treatment.
6. Astroloy: Most research here pertains to the powder-metallurgy material.
8. Inconel 807: No data available, from what we can tell.
9. Inconel 802: No data available, from what we can tell.
10. Inconel 801: No data available, from what we can tell.
11. Inconel 800: Most commonly presented as variation 800H/HT, which have higher design stresses allowable by the American Society of Mechanical Engineers (ASME), due to tighter C and Al + Ti contents.
14. Inconel 718: Here, we have chosen Inconel 718 with traditional two-step aging: 720°C for 8 hours and 620°C for 8 hours.
24. Hastelloy C22: We understand that Haynes has been emphasizing the point of age-hardenability with a long-range ordering (LRO) Ni₂Mo phase. LRO has been observed for some intermetallic phases, such as Laves or Pt₂Mo. It is believed that the increased volume fraction of the Ni₂Mo phase, upon long-term aging, contributes to the improved high-temperature strength of the Hastelloy C22 superalloy.
25. Hastelloy S: We have not identified any conclusive dataset thus far.
27. Hastelloy X: We have not identified any conclusive dataset thus far.
38. Nimonic PE13: Here we seem to be looking at a case of limited publications.

Supplementary References

1. J. Wosik, et al., *Stereological estimation of microstructural parameters of nickel-based superalloy Waspaloy using TEM methods*. Materials Characterization, 2001. **46**(2): pp. 119-123.
2. G.N. Maniar and J.E. Bridge, *Effect of gamma-gamma prime mismatch, volume fraction gamma prime, and gamma prime morphology on elevated temperature properties of Ni, 20 Cr, 5.5 Mo, Ti, Al alloys*. Metallurgical Transactions, 1971. **2**(1): pp. 95-102.
3. B.A. Ewing, R.P. Dalal, and P.B. Mee, *D 979 - An upgraded gas-turbine material*. J MATER, 1970. **5**(3): pp. 651-665.
4. J.R. Wood, *Long-time creep-rupture properties and elevated temperature stability of D-979*.
5. H. Monajati, et al., *The influence of heat treatment conditions on γ' characteristics in Udimet® 720*. Materials Science and Engineering: A, 2004. **373**(1-2): pp. 286-293.
6. I. Calliari, M. Magrini, and M. Dabala, *Microstructural evolution of Udimet 720 superalloy*. Journal of materials engineering and performance, 1999. **8**(1): pp. 111-115.
7. R.A. Ricks, A.J. Porter, and R.C. Ecob, *The growth of γ' precipitates in nickel-base superalloys*. Acta Metallurgica, 1983. **31**(1): pp. 43-53.
8. Y. Shimanuki, *Effect of heat treatment on microstructure and tensile deformation characteristics of Udimet 520*, in *Proceedings from the International Conference on Superalloys-Processing*. 1972.
9. N. Lambert, et al. *Structural stability of Udimet-500, a nickel-base superalloy*.
10. S.A. Sajjadi, H.R. Elahifar, and H. Farhangi, *Effects of cooling rate on the microstructure and mechanical properties of the Ni-base superalloy UDIMET 500*. Journal of Alloys and Compounds, 2008. **455**(1-2): pp. 215-220.
11. M. Al-Saadi, et al., *Modelling of strengthening mechanisms in wrought nickel-based 825 alloy subjected to solution annealing*. Metals, 2021. **11**(5): p. 771.
12. Y. Cao, H. Di, and R.D.K. Misra, *The impact of aging pre-treatment on the hot deformation behavior of alloy 800H at 750° C*. Journal of Nuclear Materials, 2014. **452**(1-3): pp. 77-86.
13. Y. Hisazawa, Y. Terada, and M. Takeyama, *Morphology evolution of γ' precipitates during isothermal exposure in wrought Ni-based superalloy Inconel X-750*. Materials Transactions, 2017: p. M2016376.
14. R. Cozar and A. Pineau, *Morphology of γ' and γ'' precipitates and thermal stability of inconel 718 type alloys*. Metallurgical Transactions, 1973. **4**(1): pp. 47-59.
15. S.T. Wlodek and R.D. Field, *The effects of long time exposure on alloy 718*. Superalloys, 1994. **718**(625): pp. 659-670.
16. S. Floreen, G.E. Fuchs, and W.J. Yang, *The metallurgy of alloy 625*. Superalloys, 1994. **718**(625): pp. 13-37.
17. I.J. Moore, et al., *Grain coarsening behaviour of solution annealed Alloy 625 between 600–800 C*. Materials Science and Engineering: A, 2017. **682**: pp. 402-409.
18. K. Mo, et al., *High temperature aging and corrosion study on alloy 617 and alloy 230*. Journal of engineering for gas turbines and power, 2011. **133**(5).
19. W. Ren and R. Swindeman, *A review paper on aging effects in Alloy 617 for Gen IV Nuclear Reactor applications*. Journal of Pressure Vessel Technology, 2009. **131**(2).
20. S.H. Hong, *Dynamic strain aging behavior of Inconel 600 alloy*. in *Superalloys 1996*. 1996.
21. P.K. Chaudhury and D. Zhao, *Atlas of Formability: Haynes 556*. 1993, National Center for Excellence in Metal Working Technology, Johnstown PA.
22. H.M. Tawancy, *Order-strengthening in a nickel-base superalloy (hastelloy alloy S)*. Metallurgical Transactions A, 1980. **11**(10): pp. 1764-1765.
23. W.S. Lee and H.-C. Kao, *High temperature deformation behaviour of Haynes 188 alloy subjected to high strain rate loading*. Materials Science and Engineering: A, 2014. **594**: pp. 292-301.
24. S.Y. Lee et al., *Hold-time effects on elevated-temperature low-cycle-fatigue and crack-propagation behaviors of HAYNES® 188 superalloy*. Journal of materials science, 2009. **44**(11): pp. 2945-2956.

25. X. Xie et al., *The precipitation and strengthening behavior of Ni₂(Mo,Cr) in Hastelloy® C-22HS® alloy, a new developed high Molybdenum Ni-base superalloy*. Superalloys 2008 (Eleventh International Symposium), 2008. **2**: pp. 799 - 805.
26. W.Z. Abuzaid et al., *Slip transfer and plastic strain accumulation across grain boundaries in Hastelloy X*. Journal of the Mechanics and Physics of Solids, 2012. **60**(6): pp. 1201-1220.
27. C.E. Campbell, J.C. Zhao, and M.F. Henry, *Examination of Ni-base superalloy diffusion couples containing multiphase regions*. Materials Science and Engineering: A, 2005. **407**(1): pp. 135-146.
28. C.E. Shamblen, R.E. Allen, and F.E. Walker, *Effect of processing and microstructure on René 95*. Metallurgical Transactions A, 1975. **6**(11): pp. 2073-2082.
29. Q.L. Pan et al., *Characterization of hot deformation behavior of Ni-base superalloy Rene'41 using processing map*. Materials Science and Engineering: A, 2013. **585**: pp. 371-378.
30. J.V. Gluck and J.W. Freeman, *Effect of creep-exposure on mechanical properties of Rene'41: part II: structural studies, surface effects, and re-heat treatment*. 1961.
31. C. Crozet, A. Devaux, and D. Béchet, *Microstructure stability: Optimisation of 263 Ni-based superalloy*. MATEC Web of Conferences, 2014. **14**.
32. J.C. Zhao, V. Ravikumar, and A.M. Beltran, *Phase precipitation and phase stability in nimonic 263*. Metallurgical and Materials Transactions A, 2001. **32**(6): pp. 1271-1282.
33. M.J. Wong et al., *Design of an eta-phase precipitation-hardenable nickel-based alloy with the potential for improved creep strength above 1023 K (750 °C)*. Metallurgical and Materials Transactions A, 2015. **46**(7): pp. 2947-2955.
34. E.I. Galindo-Nava, L.D. Connor, and C.M.F. Rae, *On the prediction of the yield stress of unimodal and multimodal γ' nickel-base superalloys*. Acta Materialia, 2015. **98**: pp. 377-390.
35. E.I. Galindo-Nava and C.M.F. Rae, *Microstructure evolution during dynamic recrystallisation in polycrystalline nickel superalloys*. Materials Science and Engineering: A, 2015. **636**: pp. 434-445.
36. R.W. Hayes et al., *Characterization of creep deformation of Ni-Cr solid solution alloy Nimonic 75*. Materials Science and Engineering: A, 2017. **690**: pp. 453-462.
37. K. Ali, S. Messoras, and R.J. Stewart, *Precipitation in a Nimonic PE16 alloy*. Journal of Physics F: Metal Physics, 1985. **15**(2): p. 487.
38. W.R. Witzke and J.R. Stephens, *Creep-rupture behavior of seven iron-base alloys after long term aging at 760 deg in low pressure hydrogen*. 1980.
39. J.P. Shingledecker et al., *Tensile and creep-rupture evaluation of a new heat of haynes alloy 25*. 2007, Oak Ridge National Lab.(ORNL), Oak Ridge, TN (United States).
40. R. Viswanathan et al., *U.S. program on materials technology for ultra-supercritical coal power plants*. Journal of Materials Engineering and Performance, 2005. **14**(3): pp. 281-292.
41. S. Azadian, L.-Y. Wei, and R. Warren, *Delta phase precipitation in Inconel 718*. Materials Characterization, 2004. **53**(1): pp. 7-16.
42. T. Grosdidier, A. Hazotte, and A. Simon, *Precipitation and dissolution processes in γ/γ' single crystal nickel-based superalloys*. Materials Science and Engineering: A, 1998. **256**(1): pp. 183-196.
43. P.H. Thornton, R.G. Davies, and T.L. Johnston, *The temperature dependence of the flow stress of the γ' phase based upon Ni3Al*. Metallurgical Transactions, 1970. **1**(1): pp. 207-218.
44. P. Beardmore, *On the temperature dependence of the flow stress of nickel-base alloys*. Trans. Aime, 1969. **245**: p. 1537.
45. N. Saunders, *Phase Diagram Calculations for Ni-Based Superalloys*. in In "Superalloys 1996" eds. R.D. Kissinger et al (TMS, Warrendale). 1996. 101.
46. M.J. Donachie and S.J. Donachie, *Superalloys, a Technical Guide*. 2002, Second Edition: ASM International.
47. D.C. Dunand, *Materials Science & Engineering 435: High Temperature Materials*. February 25, 2016, Lecture: Northwestern University, Evanston IL.
48. G.P. Sabol and R. Stickler, *Microstructure of nickel-based superalloys*. Physica Status Solidi B, 1969. **35**(1): pp. 11-52.

49. J. Sato, *Cobalt-base high-temperature alloys*. Science, 2006. **312**(5770): pp. 90-91.
50. C. Cui, *A New Co-Base Superalloy Strengthened by γ' Phase*. Materials Transactions, 2006. **47**(8): pp. 2099–2102.
51. A. Suzuki and T.M. Pollock, *High-temperature strength and deformation of γ/γ' two-phase Co - Al - W-base alloys*. Acta Materialia, 2008. **56**(6): p. 1288 - 97.
52. M.P. Brady, Y.Y., M.L. Santella, P.J. Maziasz, B.A. Pint, C.T. Liu, Z.P. Lu and H. Bei, *The development of alumina-forming austenitic stainless steels for high-temperature structural use*. JOM, 2008. **60**(7): pp. 12-18.
53. E.W. Ross, *Nickel-base alloys*. Superalloy II: High-Temperature Materials for Aerospace and Industrial Power, 1987.
54. C.T. Sims, N.S. Stoloff and W.C. Hagel, *Chapter 4*. Superalloys II, 1987: pp. 80-83.
55. B. Kear, *Role of 2-dislocation boundaries in plastic deformation of FCC crystals*. Transactions of the Metallurgical Society of AIME, 1962. **224**(4): p. 674.
56. B. Kear, *Clustering of slip bands in Cu_3Au crystals*. AIME TRANS, 1962. **224**(4): pp. 669-673.
57. O. Noguchi, Y. Oya, and T. Suzuki, *The effect of nonstoichiometry on the positive temperature dependence of strength of Ni_3Al and Ni_3Ga* . Metallurgical Transactions A, 1981. **12**(9): pp. 1647-1653.